UNIVERSITY OF CALIFORNIA

Los Angeles

Nonlinear Mechanics of the Bacterial Cell Wall

A dissertation submitted in partial satisfaction
of the requirements for the degree
Doctor of Philosophy in Mechanical Engineering

by

Jordan Kazuo Price

2019

ABSTRACT OF THE DISSERTATION

Nonlinear Mechanics of the
Bacterial Cell Wall

by

Jordan Kazuo Price
Doctor of Philosophy in Mechanical Engineering
University of California, Los Angeles, 2019
Professor Jeffrey D. Eldredge, Chair

Despite the relentless study of the Gram-negative bacterium *Escherichia coli* that began many decades ago and has continued to the present, the understanding of its mechanics remains weak. Technological advances in microfluidic devices and the use of atomic force microscopy (AFM) as a tool to measure mechanical properties of nanometer scale objects have pushed the field forward. However, in the latter case it remains difficult to translate force-deflection curves acquired through AFM into meaningful properties when the material is anisotropic, which is the case for the peptidoglycan (PG) cell wall in *E. coli*. The situation is further complicated by the cell's turgor pressure, which has not been reliable measured and may frequently undergo changes on the order of several atmospheres. Nevertheless, these difficulties provide opportunities for theoretical and computational mechanics researchers to help close the gaps in understanding. In this thesis we start by developing analytical and computational composite thin shell models that recognize the inner membrane as an additional stress-bearing structure within the cell envelope. These models are also utilized to investigate the anisotropic material properties of the cell wall. Next, an osmotic transport model is constructed to search for reasons why cell lysis occurs on short time scales during a rapid change in external osmolarity known as osmotic shock. Finally, we investigate the active mechanics of a growing cell wall by developing a finite growth kinematics model. New PG material is inserted into the cell wall in thin strips, which leads to a highly disordered stress field littered with stress concentrations. We study the interactions of these defects in

the cell wall and demonstrate how geometric and material nonlinearity affect them.

The dissertation of Jordan Kazuo Price is approved.

Hossein Pirouz Kavehpour

Nasr M Ghoniem

Alexander Jacob Levine

Jeffrey D. Eldredge, Committee Chair

University of California, Los Angeles

2019

To Professor Klug

TABLE OF CONTENTS

LIST OF FIGURES

LIST OF TABLES

ACKNOWLEDGMENTS

I would like to start by thanking Professor William Klug for giving me the opportunity to attend UCLA and work in his lab. I am very grateful to have learned about the field of computational mechanics from him, and for his patience and willingness to help me learn.

A big thank you to Professor Eldredge for being my committee chair and advising me for the past three years. His patience and feedback on my work helped me tremendously. Thank you Professor Levine for serving on my committee and for all of your analogies that taught me to look at problems from different points of view. Thank you to Professor Ghoniem and Professor Kavehpour for your useful comments and for taking the time to be on my committee. I would also like to thank Pierre and especially Rob for their contributions and feedback for the work presented in Chapter 3.

Thank you to my labmates and friends Aditya and Amit for making our office an enjoyable place to be over the years. So many great memories but I think the photo shoot might be at the top. Thank you Luigi for convincing me to run up and down stairs as well as the ridiculous animal stories, and thank you Sanjay for having us over to enjoy your delicious meals and for all of the great conversations. I would also like to thank Ethan for all of the M20 fun, and for always being excited to talk about anything.

Thank you Ryan for letting me follow you here and for being a great friend. And thank you to Tyler for visiting so frequently. Zion was a fantastic trip.

To my parents, thank you so much for all of your support over the years, and to Kailee for always making time for me when I come home.

Thank you Lori and Wes for your generosity and helping me survive. Finally thank you Kelsey for sticking with me through this. Youre the best.

VITA

2012	B.Eng. (Mechanical Engineering), McGill University, Montreal, Canada
2015	M.S. (Mechanical Engineering), UCLA, Los Angeles, California.
2014–2019	Teaching Assistant, Mechanical and Aerospace Engineering Department, UCLA.

CHAPTER 1

Introduction

Bacteria exhibit the extraordinary ability to withstand internal pressure changes of several atmospheres when exposed large to external concentration gradients, all while growing to double their size and dividing several times per hour. The techniques utilized to combat osmotic shocks are predominantly mechanical and are associated with two structural layers that lie within the cell envelope: the lipid bilayer inner membrane and the solid peptidoglycan cell wall. The porous PG wall is the primary stress bearing structure, a key component in cell growth, and the determining factor in maintaining cell shape. On the other hand, the fluid membrane houses mechanosensitive ion channels, which respond to local forces by opening pathways for solute and water flux, allowing the cell to regulate turgor pressure and return to an equilibrium state with the surrounding medium. Cells inevitably fail at large osmotic pressure gradients, but the manner in which they do so is surprising. Bacteria do not only burst or explode as has been previously hypothesized, rather they display several death phenotypes and commonly fail over time scales associated with cell growth. This indicates that while an osmotic shock may put a cell on the path towards lysis, the story becomes more complicated as bacterial death is frequently a slow transient process involving the active mechanics of a growing cell wall.

Motivated by experiments on single-cells subjected to osmotic downshock (a sudden decrease in external osmolarity), we investigate the causes of short and long timescale lysis in shocked cells. Acquiring a further understanding of the mechanisms behind bacterial cell death can potentially impact the development of novel antibiotics. Many antibiotics function by attacking the cell wall, inhibiting synthesis of peptidoglycan material, and creating defects in the peptidoglycan network that weakens the structure. Although we study the mechanics

of growth towards the end of this work, we focus on the stress field evolution of the cell wall in the presence of defects, which somewhat surprisingly appears to overlap with antibiotic induced cell lysis.

In order to break down the topics covered in this thesis into manageable pieces, we provide the following outline that includes specific goals at each step:

1. **Cell envelope mechanical properties:** Determine the elastic properties of the cell wall and the significance of material anisotropy in the peptidoglycan layer.
   (a) Construct a composite shell model that considers the mechanics of the inner membrane and cell wall.
   (b) Determine mechanical properties of the cell wall based on experimental results and stability requirements.
   (c) Derive key relationships between membrane tension, cell wall stresses, turgor pressure, and volume change.
   (d) Validate analytical calculations using a geometrically nonlinear finite element analysis.
2. **Transport:** Develop a transport model to determine the mechanical response of the cell to osmotic shock.
   (a) Apply the Kedem-Katchalsky transport equations to an *E. coli* cell.
   (b) Insert previously derived constitutive equations into the model.
   (c) Analyze the cell response to osmotic downshock as different parameters including shock magnitude, rate, and channel populations are varied.
   (d) Investigate how cell lysis occurs on short timescales consistent with osmotic transport.
3. **Growth:** Determine how evolution in the stress field during cell wall growth can affect cell lysis.

(a) Construct a mechanical growth model with finite kinematics and develop an evolution equation for the MreB-directed insertion of material into the cell wall.

(b) Incorporate a system of differential equations into the model that govern activation and inactivation of the discrete growth machinery.

(c) Connect the motion of the growth machinery and spatial-dependence of the activation processes to a stress-dependent probability.

(d) Determine the effects that arise when geometric and material nonlinearity are included in the model.

(e) Discuss methods to quantify cell lysis in terms of the growth model variables.

Following the outline above, Chapter 2 is devoted to the development and analysis of the composite shell model. Different geometric idealizations are compared and the effects of excess membrane area on estimates for cell wall material properties are studied. In Chapter 3 construction of the osmotic transport model is discussed, along with its coupling to the analytical model from Chapter 2. Key relationships between membrane failure and the model parameters are identified to measure cell survivability. Chapters 4 and 5 are dedicated to the large deformation growth model of the cell wall. In Chapter 4, the important concepts within the field of growing soft biological tissue mechanics are explained and illustrated through a few simple numerical examples. This framework is then applied to the bacterial cell wall in Chapter 5. Finally, Chapter 6 provides a summary of this work and includes a discussion of future research directions on the mechanics of bacteria.

CHAPTER 2

Composite Thin Shell Model of the Cell Envelope

The complex interaction between the inner membrane and cell wall is thought to strongly influence key aspects of the bacterial life cycle, such as growth, division, and death. Internal osmolyte concentrations establish turgor pressure, which presses the lipid bilayer up against the peptidoglycan cell wall, resulting in a thin laminate framework that is responsible for maintaining structural integrity by providing resistance to internal forces. Under ionic concentration gradients known as osmotic shock, the cell adapts by equilibrating the turgor pressure with the external environment. Under large pressures imposed by osmotic shock, failure of cells can occur via mechanisms such as blebbing (membrane bulging through a hole in the porous cell wall), membrane rupture, and cell wall fracture. These phenomena suggest that the mechanical properties of both layers are significant players in cell survivability. To investigate this matter, a composite shell model is constructed that aims to emulate experimentally observed deformation under pressure variations, determine the stress-bearing contributions of both lamina, and gain a quantitative understanding of the anisotropic material properties of the peptidoglycan cell wall.

Bacterial structure is predominantly influenced by the cell envelope, composed of the cell wall, an inner membrane, and in the case of gram-negative bacteria an outer membrane. This category of bacteria, which includes *Escherichia coli*, has a notably thin cell wall ($\sim 5\,\mathrm{nm}$) relative to its gram-positive counterpart that resides between the two membranes in what is known as the periplasmic space. *E. coli* cells assume a rod-like shape that can be thought of as a central cylindrical section bonded to hemispherical caps at either end. The cell wall is composed of peptidoglycan chains, with stiff glycan strands oriented circumferentially and elastic peptide links aligned axially. This leads to a directionally dependent porous

scaffold that exhibits anisotropic material properties. In fact, the cell wall displays a special type of anisotropy due to its three planes of symmetry, known as orthotropy. It has been observed that cell expansion occurs primarily in the axial direction, and it is hypothesized that the relatively weak peptide chains are the reason behind this behavior. On the other hand, the inner membrane acts as an isotropic fluid barrier to ions and other molecules that can pass through the permeable wall, controlling their entry into the cell interior. Although the lipid bilayer is largely impenetrable to most solutes, it displays the unique ability to open ion channels allowing the cell to equilibrate pressure with its surroundings by controlling osmolyte flow across the cell envelope. The analytic continuum mechanics model contained within this work is the first to consider the inner membrane as a key contributor in providing resistance to turgor pressure. The outer membrane does not appear to play a significant structural role during downshock or under normal growth conditions [8], thus it is disregarded in this work. In the sequel, "membrane" is used to refer to the inner membrane.

The life cycle of a bacterial cell is fundamentally dynamic, comprised of time-dependent processes such as ionic flow across the cell envelope, peptidoglycan construction during growth, DNA replication, and pressure variations. During growth, the cell wall exhibits viscoelastic material behavior, or in other words, the state of stress is dependent on the rate of deformation. Furthermore, when subject to hypoosmotic shock (causing increased turgor pressure) the probability of cell failure depends on the shock rate [9]. MS channel gating can return the cell to a state of pressure equilibrium with its surrounding environment, but extreme shocks on short time scales do not provide adequate time for the cell to respond, leading to low probabilities of survival. These dynamic processes become extremely complex when combined, thus we analyze the simpler picture of mechanical deformation under "small" turgor pressures that have negligible dependence on channel gating. While the exact values of turgor pressure and critical gating tensions are not precisely known, they are thought to lie in the ranges $p = 0.1 - 5$ atm and $0.1 - 2.0 k_{\mathrm{B}}T/\mathrm{nm}^2$, respectively.

Several recent works have examined the mechanical properties of the peptidoglycan sacculus in *E. coli* – in particular the stiffness known as the Young's modulus, E – through experimental measurements and theoretical analysis. The small cellular length scales in-

herent to bacteria have made it difficult to accurately determine their material properties. Advances in atomic force microscopy (AFM) help combat this issue, and several studies have utilized this technique coupled with theoretical calculations to infer the elastic moduli from measurements [2, 10, 1]. Similar empirical approaches and molecular dynamics simulations have been used to investigate the mechanical characteristics of peptidoglycan networks in bacterial cells [11, 12]. From these works, the reported values for the Young's modulus vary through a wide range, $E \sim 5-200\,\mathrm{MPa}$. Additionally, many of these results rely on the assumption that the cell wall is isotropic. However, the observed axially dominated nature of deformation makes this highly improbable. Moreover, the stress-bearing contribution of the membrane has previously been ignored, which necessarily requires that the turgor pressure is resisted entirely by the cell wall. We postulate that both the material anisotropy of the peptidogylcan cell wall and the ability of the membrane to sustain a state of isotropic tension play key roles in how bacteria resist turgor pressure and respond to osmotic challenge. Therefore, the composite model derived herein incorporates both layers in order to provide new insights into the mechanics of the cell envelope.

2.1 The Model

As our model scenario we consider a spherocylindrical bacterial cell subjected to an outward-directed pressure representing the mechanical load due to a hypoosmotic shock — i.e., a rapid reduction in osmolarity of the surrounding medium that drives water through the semipermeable cell envelope, leading to an expansion of volume. We idealize the structure of the cell envelope as a composite shell of two layers: The inner layer is a fluid membrane of finite stiffness in bending and area stretch, representing a lipid bilayer membrane. The outer layer is a thin solid shell, representing the peptidoglycan (PG) cell wall. For *E. coli* and other Gram negative cells, the PG layer is thin (likely in the range of one to a few molecules thick), and sandwiched between the inner lipid membrane and a second, outer lipid membrane. However, this outer membrane is understood to have a more disordered gel-like structure offering insignificant mechanical support. We neglect the outer membrane

in our model.

2.1.1 Kinematics & Constitutive Response

We assume that the membrane and cell wall layers remain in contact throughout the deformation. Furthermore, because both layers are thin ($h \approx 5\,\text{nm}$) relative to the dimensions of the cell ($R \approx 1\,\mu\text{m}$) we neglect the distance between layers and describe the kinematics in terms of a single surface ω, which we may think of as the mid surface between the layers.

2.1.1.1 Membrane

The inner lipid membrane is modeled as a fluid surface, insensitive to surface shears, but resistant to bending and isotropic stretching. The surface bending elasticity is modeled by the classic Helfrich-Canham-Evans energy [13, 14, 15],

$$\Pi_{\text{b}}^{\text{m}} = \int_{\omega} \frac{\mathcal{K}_b}{2}(2H - C_0)^2 + \mathcal{K}_G K \, da, \tag{2.1}$$

where $\mathcal{K}_b$ and $\mathcal{K}_G$ are defined as the bending and Gaussian moduli, and C_0 is the spontaneous curvature arising from asymmetries in the bilayer. Additionally, the mean curvature $H = a^{\alpha\beta}b_{\alpha\beta}$ is the average of the two principal curvatures, and the Gaussian curvature $K = \det(b_{\alpha\beta})/\det(a_{\alpha\beta})$ is their product.

The in-plane stretching elasticity is modeled by defining a relation between surface tension τ_m and areal strain

$$\epsilon_A = \frac{da}{dA}. \tag{2.2}$$

Because membrane fluidity guarantees that the surface tension will be homogeneous, we can also compute the areal strain as

$$\epsilon_A = \frac{\Delta A}{A_0} = \frac{A[\boldsymbol{x}] - A_0}{A_0}, \tag{2.3}$$

where A and A_0 are the total areas of the deformed and reference configurations, respectively. For small tensions, the corresponding change in area involves the "smoothing" or "flattening out" of thermal undulations in the membrane, and results in an exponential area-tension

constitutive relation. For larger tensions, such as those that trigger gating of mechanosensitive channels, changes in area of the membrane actually involve changes in lipid density. In this case, the tension is directly proportional to areal strain,

$$\tau_m = K_A \epsilon_A. \tag{2.4}$$

The stretching modulus, K_A, for typical lipid bilayers takes values on the order of $K_A = 30\text{–}60 k_\mathrm{B}T/\mathrm{nm}^2$ [16, 17, 18]. The energy of elastic stretch can then be obtained by integration of (2.4),

$$\Pi_\mathrm{s}^\mathrm{m} = \int_\Omega \frac{K_A}{2} \epsilon_A^2 dA = \frac{K_A}{2} \frac{(A - A_0)^2}{A_0}, \tag{2.5}$$

and the total membrane energy is the sum of bending and stretching contributions

$$\Pi^\mathrm{m} = \Pi_\mathrm{b}^\mathrm{m} + \Pi_\mathrm{s}^\mathrm{m}. \tag{2.6}$$

2.1.1.2 Cell Wall

The bacterial cell wall is constructed of a disordered network of peptidoglycan, that is thought to be one to several layers thick. As with the membrane, we write the elastic strain energy of the peptidoglycan layer as a combination of stretching and bending terms, in this case according to standard thin shell elasticity [19],

$$\Pi^\mathrm{w} = \Pi_\mathrm{b}^\mathrm{w} + \Pi_\mathrm{s}^\mathrm{w}, \tag{2.7}$$

$$\Pi_\mathrm{b}^\mathrm{w} = \int_\Omega \frac{1}{2} D^{\alpha\beta\gamma\delta} \rho_{\alpha\beta} \rho_{\gamma\delta} dA, \tag{2.8}$$

$$\Pi_\mathrm{s}^\mathrm{w} = \int_\Omega \frac{1}{2} A^{\alpha\beta\gamma\delta} E_{\alpha\beta} E_{\gamma\delta} dA. \tag{2.9}$$

Fourth order tensors $A^{\alpha\beta\gamma\delta}$ and $D^{\alpha\beta\gamma\delta}$ contain the elastic and bending material constants, respectively. The curvature change and elastic strain tensors are denoted by $\rho_{\alpha\beta}$ and $E_{\alpha\beta}$, respectively.

For spherocylindrical bacteria like *E. coli*, the cell wall is a two-dimensional orthotropic material, with stiffness along the axis of the cell that is softer than in the azimuthal (i.e., "hoop") direction. We define a linear orthotropic stress-strain response in terms of a cylindrical polar coordinate system with axial coordinate z and azimuthal angle θ, with flexibility

relation

$$\boldsymbol{\epsilon} = \begin{bmatrix} \epsilon_z \\ \epsilon_\theta \\ 2\epsilon_{z\theta} \end{bmatrix} = \frac{1}{h} \begin{bmatrix} 1/E_z & -\nu_{\theta z}/E_\theta & 0 \\ -\nu_{z\theta}/E_z & 1/E_\theta & 0 \\ 0 & 0 & 1/G_{z\theta} \end{bmatrix} \begin{bmatrix} \tau_z \\ \tau_\theta \\ \tau_{z\theta} \end{bmatrix}$$
$$= \mathbf{S}\boldsymbol{\sigma} \tag{2.10}$$

where E_z and E_θ are the Young's moduli in the z and θ directions, $\nu_{\theta z}$ and $\nu_{z\theta}$ are the Poisson's ratios, and $G_{z\theta}$ is the shear modulus. Here $\boldsymbol{\tau}$ are two-dimensional stress resultants, having units of force per length. The wall is sufficiently thin that we can assume the (three-dimensional) stresses to be uniform through the thickness, such that the integrated stress resultants (force per unit length along an edge of the surface) are obtained by multiplying by the thickness h ($\boldsymbol{\tau} = h\boldsymbol{\sigma}$). Thermodynamic reversibility demands that $dg = \boldsymbol{\tau}^T d\boldsymbol{\epsilon} = \boldsymbol{\tau}^T \mathbf{S} d\boldsymbol{\tau}$ be a perfect differential. This requires that $\mathbf{S}$ be symmetric, that is

$$\frac{\nu_{\theta z}}{\nu_{z\theta}} = \frac{E_\theta}{E_z} \equiv \alpha. \tag{2.11}$$

We will take this ratio α, along with E_z and $\nu \equiv \nu_{z\theta}$ as the independent material parameters in our model.

2.1.2 Loading and Equilibrium

The only load considered is the internal turgor pressure. A potential for the pressure load p can be written as follows

$$V^{\text{ext}} = \int p \, \mathrm{d}v = \frac{1}{3} \int p \, \nabla \cdot \boldsymbol{x} \, \mathrm{d}v = \frac{1}{3} \int p \, \boldsymbol{x} \cdot \boldsymbol{n} \, \mathrm{d}a, \tag{2.12}$$

allowing us to write the total potential energy as a sum of three terms:

$$\Pi = \Pi^{\text{m}} + \Pi^{\text{w}} + V^{\text{ext}}. \tag{2.13}$$

Mechanical equilibrium is attained by minimizing the total potential energy. For a general spherocylindrical geometric model of the cell the resulting Euler-Lagrange equations are not amenable to analytical solution. For this case we discretize the general problem with

cubic axisymmetric finite elements. However, for simpler idealizations of cell shape the equilibrium equations may be solved by hand. In the following section we work out solutions for idealized spherical and cylindrical shapes and compare them to the numerically computed spherocylindrical model. Specifically, expressions for membrane tension (τ_m) and volume strain (ϵ_V) are derived to facilitate comparison with experimental results.

2.2 Comparison of Different Geometric Idealizations

Sphere

We begin with the simplest idealization — a spherical shell of radius R with isotropic cell wall properties ($\alpha \equiv E_\theta/E_z = 1$). This produces a uniform isotropic state of strain with no bending effects to lowest order. The membrane and cell wall layers deform together with equal strains ($\epsilon_z = \epsilon_\theta = \epsilon_A/2$). Summing the stress resultants (force per unit length) of the membrane and wall gives

$$\tau = \tau^{\mathrm{m}} + \tau^{\mathrm{w}} = \left(K_A^{\mathrm{m}} + K_A^{\mathrm{w}}\right)\epsilon_A, \tag{2.14}$$

where K_A^{w} is the wall stretch modulus, defined as $K_A^{\mathrm{w}} = Eh/2(1-\nu)$. The equilibrium equations here reduce to the well-known Laplace-Young equation, which balances the pressure difference $p = p_{in} - p_{out}$ across both lamina with stress resultants $\tau = pR/2$. Combining the stress resultants of both layers allows us to write the pressure in terms of the areal stretch,

$$p = \frac{2}{R}\left(K_A^{\mathrm{m}} + K_A^{\mathrm{w}}\right)\epsilon_A. \tag{2.15}$$

Taking $E \to 0$ in Eqn. (2.15) eliminates the load bearing contribution of the wall and we are left with the area-stretch relationship for the membrane, shown in Eqn. (2.4). The linearized volumetric strain can be written in terms of a bulk modulus K_V and pressure,

$$\epsilon_V = \frac{1}{K_V}p = \frac{3}{2\left(K_A^{\mathrm{m}} + K_A^{\mathrm{w}}\right)}\frac{pR}{2}. \tag{2.16}$$

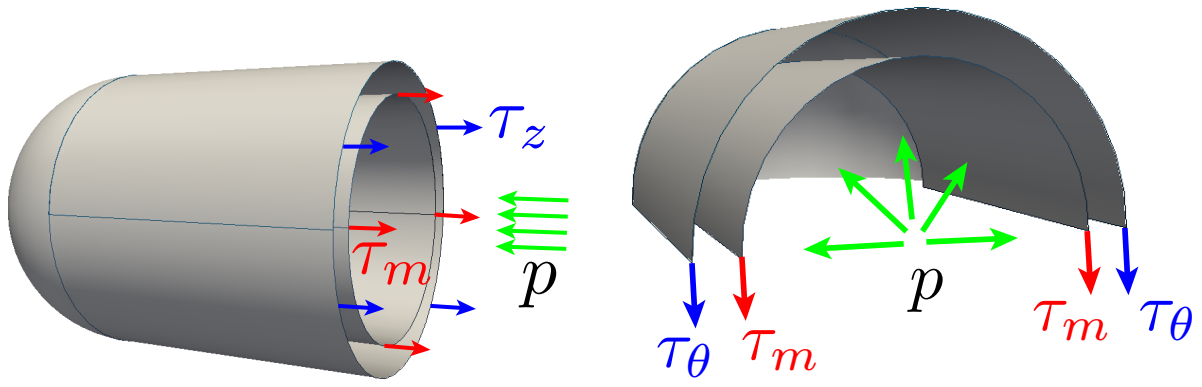

Figure 2.1: Free body diagrams of a cylindrical composite shell composed of membrane and peptidoglycan layers. Stress resultants τ_m, τ_θ and τ_z balance the internal pressure p. The geometry of the pressurized cylinder leads to circumferential stresses (right) that are twice as large as those aligned with the cylindrical axis (left).

Orthotropic Cylinder

In the simplified cylindrical model, we consider both the structural and mechanical orthotropy of the cell wall. For the pressurized cylinder, shear is zero, $\sigma_{z\theta} = 0 \Rightarrow \epsilon_{z\theta} = 0$, so that Hooke's law for the stress resultants simplifies to

$$\underbrace{\begin{bmatrix} \epsilon_z \\ \epsilon_\theta \end{bmatrix}}_{\boldsymbol{\epsilon}} = \underbrace{\frac{1}{E_z h} \begin{bmatrix} 1 & -\nu \\ -\nu & 1/\alpha \end{bmatrix}}_{\mathbf{S}} \underbrace{\begin{bmatrix} \tau_z \\ \tau_\theta \end{bmatrix}}_{\boldsymbol{\tau}}. \tag{2.17}$$

To couple the membrane and peptidoglycan layers, and determine the stresses in a cylindrical shell, we can use free body diagrams of sections defined by axial and longitudinal cuts. A cut perpendicular to the axis (Fig. 2.1) allows us to compute the axial tension τ_z,

$$\pi R^2 p = 2\pi R(\tau_z + \tau_m). \tag{2.18}$$

Notably, this is the same as the Laplace-Young relation ($\tau = pR/2$) for a spherical shell with a combined surface tension $\tau_z + \tau_m$. A cut parallel to and through the axis of the cylinder gives the circumferential tension τ_θ,

$$2RLp = 2L(\tau_\theta + \tau_m). \tag{2.19}$$

We can solve for the stress resultants in the PG layer as

$$\boldsymbol{\tau} = \begin{bmatrix} \tau_z \\ \tau_\theta \end{bmatrix} = \begin{bmatrix} pR/2 - \tau_m \\ pR - \tau_m \end{bmatrix}. \tag{2.20}$$

Hooke's law from Eqn. (2.17) can then be written as

$$\boldsymbol{\epsilon} = \begin{bmatrix} \epsilon_z \\ \epsilon_\theta \end{bmatrix} = \mathbf{S} \begin{bmatrix} pR/2 - \tau_m \\ pR - \tau_m \end{bmatrix}. \tag{2.21}$$

The membrane area-stretch relationship $\tau_m = K_A \epsilon_A = K_A(\epsilon_z + \epsilon_\theta)$ can be substituted into Eqn. (2.20), leading to

$$\boldsymbol{\epsilon} = \underbrace{\left(\mathbf{I} + K_A \mathbf{S} \begin{bmatrix} 1 & 1 \\ 1 & 1 \end{bmatrix} \right)^{-1} \mathbf{S}}_{\mathbf{S}_c} \begin{bmatrix} 1 \\ 2 \end{bmatrix} \frac{pR}{2}. \tag{2.22}$$

The membrane tension can then be written in terms of an *effective* area-stretch modulus K_A^*,

$$\begin{aligned} \tau_m &= K_A \epsilon_A \\ &= \frac{K_A}{K_A^*} \frac{pR}{2} \\ &= \frac{2 + \alpha(1 - 3\nu)}{1 + \alpha\left(1 - 2\nu + \frac{hE_z}{K_A}\right)} \frac{pR}{2}. \end{aligned} \tag{2.23}$$

Note that in the limit as $E_z \to 0$, we also have $\nu \to 0$ for stability, which gives $K_A^* \to K_A$ and $\tau_m \to pR/2$ as expected. The fractional volume change is

$$\begin{aligned} \epsilon_V &= \epsilon_z + 2\epsilon_\theta, \\ &= \begin{bmatrix} 1 & 2 \end{bmatrix} \left(\mathbf{I} + K_A \mathbf{S} \begin{bmatrix} 1 & 1 \\ 1 & 1 \end{bmatrix} \right)^{-1} \mathbf{S} \begin{bmatrix} 1 \\ 2 \end{bmatrix} \frac{pR}{2}, \\ &= \frac{1}{K_V} p, \end{aligned} \tag{2.24}$$

where

$$K_V = \frac{2K_A}{R} \frac{1 + \alpha(1 - 2\nu + \frac{hE_z}{K_A})}{4 + \alpha(1 - 4\nu) + \frac{K_A}{hE_z}(1 - \alpha\nu^2)}. \tag{2.25}$$

2.3 Analysis

2.3.1 Model Comparison

To gain a sense of how the models mechanically respond to hypoosmotic shock, we investigate the effects of increased pressure on membrane tension and strains (Fig. 2.2). Values for the material parameters used to calculate $\tau_m(p)$ and $\epsilon_V(p)$ are summarized in Table 2.1. Notably, based on AFM measurements [1], we select $E_z = 25$ MPa and $E_\theta = 50$ MPa for the cell wall moduli, which gives $\alpha = 2$. As material anisotropy is neglected in the spherical model, the sole elastic modulus is set as the average of the two cylindrical moduli, i.e., $E_{\text{iso}} = E_z(1+\alpha)/2$.

In Fig. 2.2, all three models exceed the critical lytic tension of $\tau_m^{\text{rupture}} = 3.5\ k_{\text{B}}T/\text{nm}^2$—corresponding to critical rupture stretch $\epsilon_A^{\text{rupture}} = \tau_m^{\text{rupture}}/K_A = 5.83\%$—at less than one atmosphere of pressure, suggesting that the membrane is bearing too much load. It may be that MS channels, which gate at sub-lytic values, are able to prevent tension from reaching the rupture limit by rapidly moving cytoplasmic contents out of the cell. Alternatively, it is plausible that in living cells the membrane simply does not stretch this much. We also observe that though the orthotropic cylindrical model neglects bending energy and geometric nonlinearities induced by the hemispherical endcaps, membrane loads largely agree with those in the spherocylindrical finite element analysis, implying that these contributions do not significantly alter membrane tension.

Table 2.1: Cell wall and membrane material parameters used in Fig. 2.2 calculations [1, 2].

Parameter	Symbol	Value
Cell radius	R	500 nm
Cell wall thickness	h	5 nm
Membrane stretch modulus	K_A	60 $k_{\text{B}}T/\text{nm}^2$
Cell wall anisotropy	α	2
Axial elastic modulus	E_z	25 MPa
Isotropic elastic modulus	E_{iso}	37.5 MPa
Poisson ratio	ν	0.3

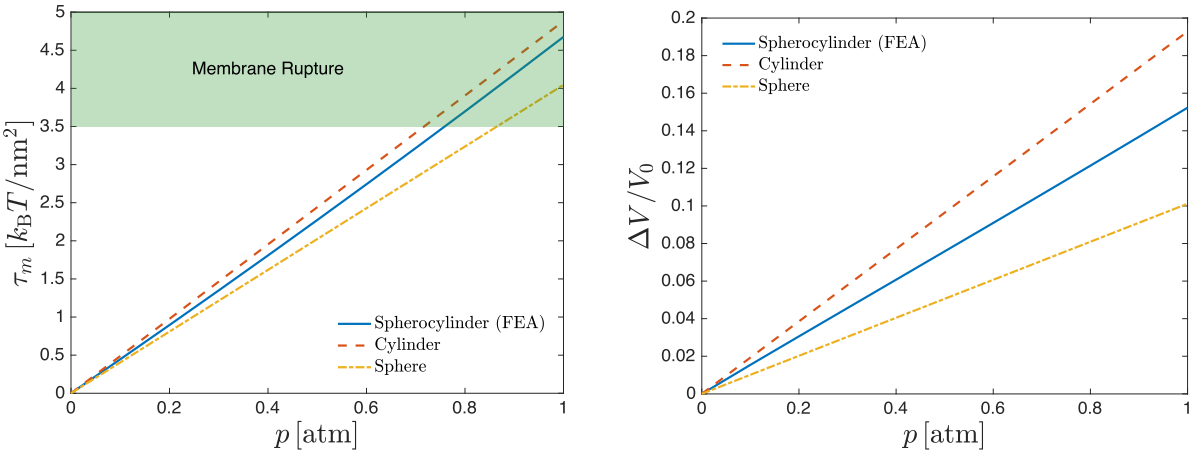

Figure 2.2: Dependence of membrane tension (left) and volumetric strain (right) on pressure for each model. Left: tensions within the green region exceed the critical rupture tension for a lipid bilayer ($\tau_m^{\text{rupture}} \gtrsim 3.5\, k_B T/\text{nm}^2$). The cylindrical and finite element model exhibit similar behavior. Right: volumetric strain versus pressure. At 1 atm of pressure the differences in normalized volume change are significant, with the spherocylindrical model attaining a value twice that of the sphere.

Fractional changes in volume range between 10% and 20% at 1 atm, slightly exceeding estimates of 8 to 12% based on AFM measurements [2]. Other reported values volumetric strains fall between a few percent up to roughly 30%, though . While hyperosmotic shocks leading to plasmolysis induce reductions in volume up to ≈ 50 %, hypoosmotic shocks lead to smaller increases in volume, possibly hinting at cell stiffening. For the cylindrical model we calculate strains $\epsilon_z \approx -3\%$ and $\epsilon_\theta \approx 11\%$ at $p = 1$ atm. This result clearly conflicts with the observed longitudinally dominated expansion of rod-shaped bacterial cells under pressure, which warrants further investigation of the mechanical properties of the cell wall.

2.3.2 Calculating Bounds on α and ν

We first investigate thermodynamic stability, which requires that the determinant of the cell wall compliance matrix in Eq. (2.17) is positive ($\det \mathbf{S} > 0$). From this we obtain

$$E_z > 0, \qquad \alpha > 0, \qquad \frac{1}{\alpha} - \nu^2 > 0. \tag{2.26}$$

Although the Poisson ratio has not been reliably measured, we can bound it for stability

$$|\nu| < \frac{1}{\sqrt{\alpha}}. \tag{2.27}$$

We enforce the same requirement on the determinant of the composite compliance matrix $\mathbf{S}_\mathrm{c}$ in Eq. (2.22). For all values of ν, we recover the same condition determined for the isolated cell wall in Eq. (2.27). Additionally, if both $\nu > 1/2$ and $K_A > E_z h/(2\nu - 1)$, the Poisson ratio is also valid in a region defined by

$$\nu > \frac{1}{2}\left(1 + \frac{1}{\alpha} + \frac{E_z h}{K_A}\right). \tag{2.28}$$

Next, we turn our attention to conditions on strain garnered from experimental research. During an osmotic shock bacteria such as *E. coli* exhibit swelling, but largely maintain their rod-like geometry. For this to occur, cells extend almost exclusively along their longitudinal axis, while circumferential strains are near zero. Starting with the hoop strain, we set $\epsilon_\theta \approx 0$ and solve for α in terms of ν,

$$\alpha \approx \frac{1 + 2\frac{E_z h}{K_A}}{\nu\left(\nu + \frac{E_z h}{K_A}\right)}. \tag{2.29}$$

We can also impose axially dominated deformation by assuming $\epsilon_z > \epsilon_\theta$ in Eq. (2.22), and solve the inequality for α to get

$$\alpha > \frac{2\left(1 + \frac{E_z h}{K_A}\right)}{2\nu^2 + \frac{E_z h}{K_A}(1 - \nu)}. \tag{2.30}$$

The bounds of Eqns. (2.27)-(2.30) are combined and shown in Fig. 2.3. Thermodynamic stability necessitates that valid (α, ν) pairs lie within the filled regions, while the checkered area indicates that (α, ν) additionally satisfy the axially dominated strain condition, $\epsilon_z > \epsilon_\theta$. In the positive ν axis, the stability bound of Eq. (2.27) intersects the two strain conditions at $\alpha = 4$ and $\nu = 1/2$. This intersection point corresponds to the case of zero deformation (i.e., $\epsilon_z = \epsilon_\theta = 0$), and is independent of the dimensionless parameter $\beta \equiv E_z h/K_A$. The yellow area defined by Eq. (2.28) lies far from the $\epsilon_\theta = 0$ curve, and selecting parameters within this region leads to large hoop strains and negative axial strains, thus we neglect further discussion of it. Hoop strains also exceed axial strains within the blue section, and

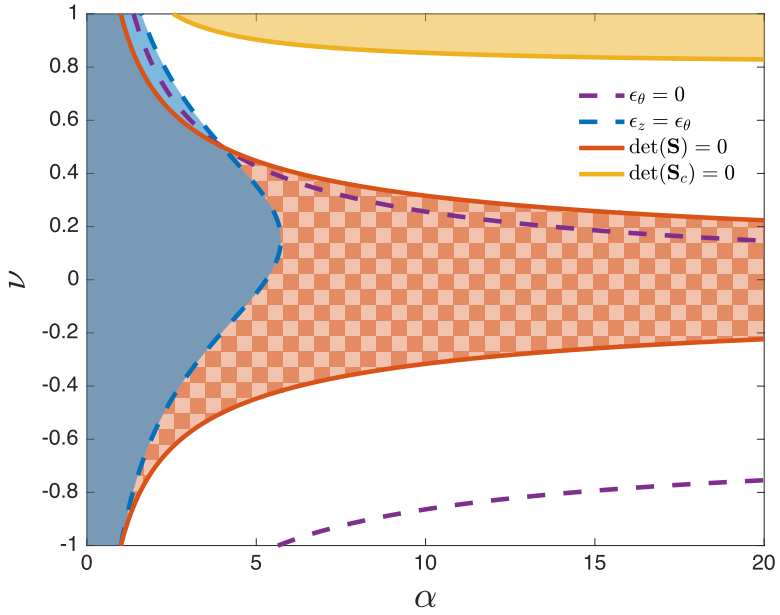

Figure 2.3: Restrictions on cell wall anisotropy $\alpha \equiv E_\theta/E_z$ and Poisson ratio ν. Thermodynamic stability (solid lines) requires (α, ν) to fall into the filled regions, while the checkerboard section additionally satisfies axially dominated strains ($\epsilon_z > \epsilon_\theta$). It is expected that (α, ν) will lie near the $\epsilon_\theta = 0$ curve (purple dashed line) within the checkered area. Material properties used in this figure are taken from Table 2.1: $E_z = 25\,\mathrm{MPa}$, $K_A = 60\,k_\mathrm{B}T/\ \mathrm{nm}^2$, and $h = 5\,\mathrm{nm}$.

we disregard it as well. Within the checkerboard section (Fig. 2.3), we expect (α, ν) to lie near the $\epsilon_\theta = 0$ curve. If we consider for the moment $0 < \nu < 1/2$ and $\beta < 1$, then we must have $\alpha > 4$. This finding indicates that for positive Poisson ratios, the circumferential elastic modulus E_θ is at least 4 times larger than that in the axial direction E_z. In fact, α can only approach the value of 4 when ν is very close to 1/2 (corresponding to the case of zero deformation), thus we expect a larger value. For $\beta > 1$, the minimum limit on α is marginally weakened, resulting in a shift of the $\epsilon_z = \epsilon_\theta$ curve to the left (see Figure in appendix). However, based on experimental determined material properties we expect the upper limit to be $\beta \approx 1.25$, which leads to an insignificant change on the minimum value of α.

Turning our attention to the negative ν axis, for $\alpha > 1$ there exists a lower thermodynamic bound that lies well above the $\epsilon_\theta = 0$ lower curve. As the Poisson ratio becomes increasingly negative, it also distances itself from the upper ϵ_θ strain condition. While negative values of ν cannot be immediately be disregarded, the fact that the zero hoop strain condition cannot be approached makes them far less likely.

To further study the α-ν relationship, hoop-to-axial and volumetric strain contours are displayed in Fig. 2.4, where $\nu \in [-1/2, 1/2]$. As the strains from Eq. (2.22) are both directly proportional to p, the ratio $\epsilon_\theta/\epsilon_z$ is independent of pressure and solely depends on material properties α, ν, and β. A narrow band highlighted by stripes depicts (α, ν) that satisfy $\epsilon_\theta/\epsilon_z = 0 \pm 0.2$, an approximation of where we expect $\epsilon_\theta/\epsilon_z$ to fall. Volumetric strain contour lines partially correlate with $\epsilon_\theta = 0$, and the strains near this curve are reasonable for pressures of one atm. Volumetric strains have been measured to be on the order of several percent for "small" hypoosmotic shocks [20], up to $\approx 20\%$ for larger changes in external osmolarity [21]. Negative values of ν lead to larger changes in volume, which corresponds to increases in membrane tension. With this additional evidence, we select new values of α and ν to satisfy all of these conditions, and carry out stress and strain calculations.

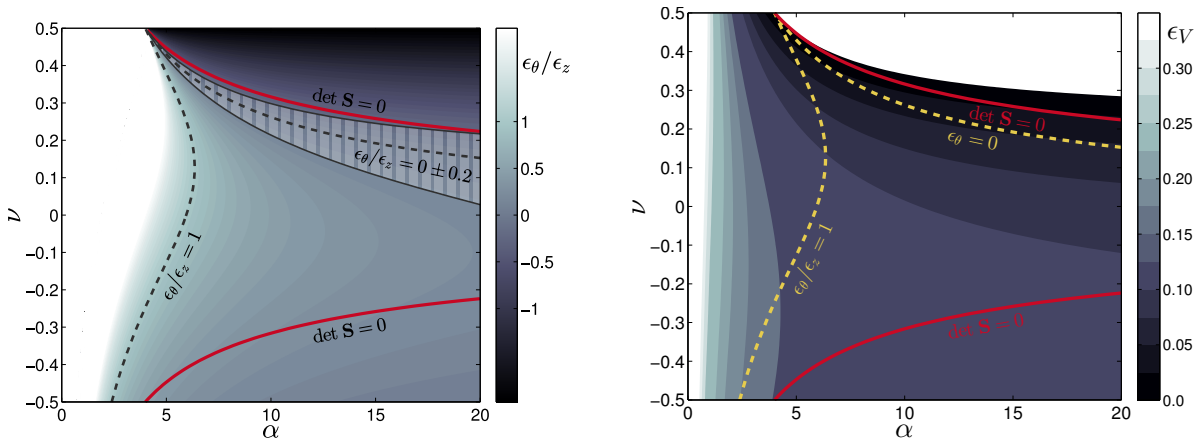

Figure 2.4: Left: Strain ratio $\epsilon_\theta/\epsilon_z$ contours plotted on α-ν axes using Table 2.1 parameters. Solid red lines indicate thermodynamic stability bounds, and dashed black lines show important strain curves. Experimental evidence shows that axial strains dwarf circumferential strains, the latter of which approaches a value near zero. Right: Volumetric strain ϵ_V at pressure $p = 1$ atm. Small volumetric strains $\lesssim 15\%$ are expected. Yellow lines mark strain conditions ($\epsilon_z = \epsilon_\theta$, $\epsilon_\theta = 0$) and red lines define stability bounds.

2.3.3 Recalculating Stresses and Strains with Greater Anisotropy

We revisit calculations performed in Section 2.3.1, this time selecting $\alpha = 8$ to satisfy $\epsilon_z > \epsilon_\theta$ and $\epsilon_\theta \approx 0$, based on restrictions determined in Section 2.3.2. The spherical modulus is recalculated due to its dependence on α, while all other parameters remain the same as in Table 2.1. The updated results are tabulated in Table 2.2.

For the cylindrical model, increasing α while holding all other parameters constant has the simple effect of strengthening the cell wall hoop modulus, E_θ. Consequently, the wall bears a larger portion of the pressure load, and alters deformation such that for $\alpha = 8$, the axial strain is roughly three times greater than the hoop strain. This shift to axially dominated deformation causes a reduction in fractional volume change, as ϵ_θ has twice the influence of ϵ_z on ϵ_V (2.24), and ϵ_θ is reduced by an order of magnitude for the chosen parameters. Likewise the change in surface area is diminished, decreasing membrane tension to sub-lytic values at $p = 1$ atm.

Although the spherical model provides reasonable results for membrane tension and vol-

Table 2.2: Membrane tension, wall stresses, and strains at $p = 1$ atm. The elastic modulus in the spherical model is $E_{\text{iso}} = E_z(\alpha+1)/2$, with $\alpha = 8$. Cylinder 1 uses $\alpha = 2$ and Cylinder 2 used $\alpha = 8$.

	Sphere	Cylinder 1	Cylinder 2
τ^{m} $[k_{\text{B}}T/\text{nm}^2]$	2.43	5.11	2.71
τ_z^{w} $[k_{\text{B}}T/\text{nm}^2]$	3.76	1.09	3.48
τ_θ^{w} $[k_{\text{B}}T/\text{nm}^2]$	3.76	7.28	9.67
ϵ_z [%]	2.03	−2.37	3.43
ϵ_θ [%]	2.03	10.9	1.10
ϵ_A [%]	4.05	8.51	4.52
ϵ_V [%]	6.08	19.4	5.62

ume change, the uniformity of the strains does not reproduce the characteristic axial swelling under pressure exhibited by *E. coli* cells. Furthermore, it is difficult to map the anisotropic material properties from the cylinder onto a sphere, and our method of averaging the elastic moduli to determine E_{iso} is simply an estimate. Though these shortcomings prevent us from using the spherical model to gain novel insights into the anisotropic cell wall properties, it nonetheless remains a valuable tool in assessing the cylindrical model's validity.

While the cylindrical strains shown in Table 2.2 are in general agreement with the lower end of prior estimates, further cell swelling will push membrane tension to and past lytic limits. It appears that the cell wall must still carry a greater portion of the pressure load, and the membrane areal stretch must not increase. It may be that the membrane areal stretch modulus resides on the low end of prior experimental results. We can also consider that bacteria contain an excess of membrane, such that the cell wall bears all of the pressure load up until a critical pressure is reached, and the membrane attaches to the cell wall.

2.3.4 Excess Membrane Area

The areal strains predicted by the cylindrical model are seen to decrease as α (and overall wall stiffness) increases, consequently lowering membrane tensions below those required for rupture (Table 2.2). However, the calculated volumetric strain falls well beneath observed estimates of 15 %. Simply reducing both cell wall elastic moduli (E_z and E_θ) by the same factor can increase volumetric deformation, but this coincides with increasing areal stretch, which places the membrane under greater stress. Using the linear areal stretch relationship from Eq. (2.4), rupture tensions of 2.5–3.5 $k_{\mathrm{B}}T/\mathrm{nm}^2$ are consistent with areal strains of only 4–6 %. To allow for increased cell swelling while preventing large membrane stretches that induce rupture we consider that under normal "turgor" pressure the membrane is tension free, with some reservoir of "excess" area available such that small swelling of the cell pulls from the reservoir without actually stretching the membrane. This residual area will allow the cell to initially undergo expansion without stretching the inner membrane.

We can construct a simple model of excess membrane area by adjusting Hooke's law to include a "pre-strain" parameter ϵ_0,

$$\tau_m = K_A(\epsilon_A - \epsilon_0)_+, \tag{2.31}$$

where we use "Macaulay brackets" to denote the ramp function

$$(x)_+ = \begin{cases} 0, & x < 0 \\ x, & x \geq 0. \end{cases} \tag{2.32}$$

We make the assumption that the "pre-strain" is exhausted in both the z and θ directions simultaneously. For a given amount of excess membrane area, we can write the critical pressure at which the membrane attaches to the wall as

$$p^* = \frac{2\alpha h E_z}{R(\alpha + 2 - 3\alpha\nu)}\epsilon_0. \tag{2.33}$$

An estimated membrane "pre-strain" of $\epsilon_0 = 5\,\%$ corresponds to a critical pressure $p^* \approx 0.5\,\mathrm{atm}$. As the excess membrane area is depleted the peptidoglycan layer becomes the

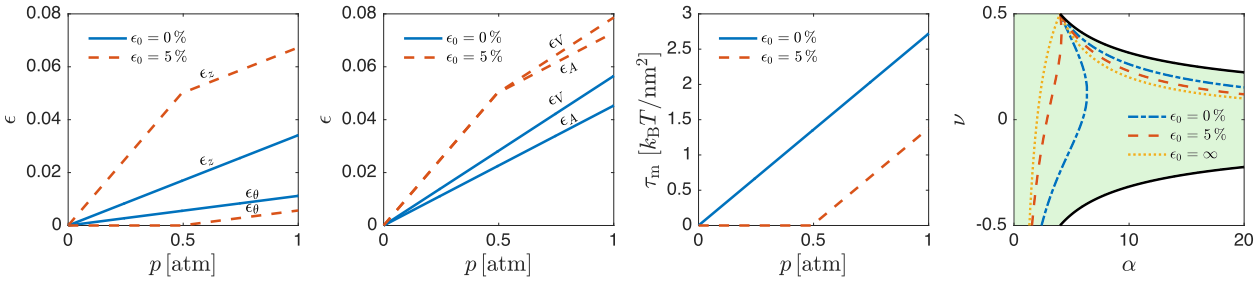

Figure 2.5: (a) With a pre-strain of $\epsilon_0 = 5\%$, cell lengthening becomes far more noticeable and the axial strain ϵ_z is roughly an order of magnitude larger than the circumferential strain ϵ_θ. Without excess membrane area, the cylinder deforms in a more uniform manner. (b) Areal and volumetric strains are seen to increase in the pre-strain model, as the cell wall is the sole stress-bearing layer until the areal strain reaches the pre-strain value. For $p < p^*$ we have $\epsilon_A = \epsilon_V$, as the hoop strain ϵ_θ is identically zero. (c) The membrane tension remains at zero until the membrane reservoir is exhausted, and then increases at the same rate as the original model. Pressures of fractions of an atmosphere are required to "use up" the excess area. (d) Parametric study of α and ν at $p = 1\,\text{atm}$. Solid black lines indicate stability bounds, and the various dashed curves show $\epsilon_\theta = 0$ (horizontal) and $\epsilon_z = \epsilon_\theta$ (vertical) for different pre-strain values. As pre-strain increases, the lower bound on α in the positive ν axis is reduced from 4 when $\epsilon_0 = 0$ to 2 when $\epsilon_0 = \infty$, and the range of suitable choices of α and ν is increased.

sole provider of resistance to internal pressure. This leads to a modified expression for the *effective* area-stretch modulus K_A^* that is obtained by taking $K_A \to 0$ in Eq. (2.23),

$$K_A^* = \frac{\alpha h E_z}{2 + \alpha\,(1 - 3\nu)}. \tag{2.34}$$

Using properties from Table 2.1 and selecting $\epsilon_0 = 5\,\%$, the strains, tension, and $\alpha - \nu$ relationship are calculated and displayed in Fig. 2.5.

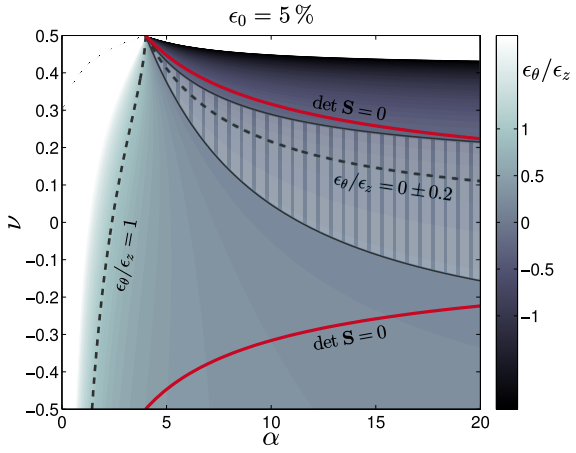

Figure 2.6: With $\epsilon_0 = 5\,\%$, the striped region indicating valid (α, ν) is expanded and shifted downward. Compared to the zero prestrain case, the striped area for $\alpha < 10$ is much larger. The critical pressure at which the membrane becomes taut is $p^* \approx 0.69\,\text{atm}$.

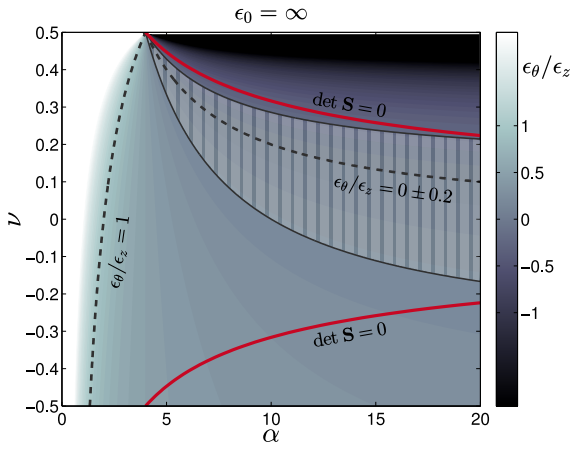

Figure 2.7: The case of infinite excess area is identical to having no membrane contribution in the model. This case does not differ significantly from that of $\epsilon_0 = 5\,\%$.

The most obvious consequence of excess membrane area is the reduction in membrane tension as the cell is pressurized (Fig. 2.5). In the original model where the membrane is taken to be attached to the cell wall, tensions approached those required for rupture ($\tau_m^{\text{rupture}} \approx 3.5 k_{\text{B}}T/\text{nm}^2$) at pressures less than one atmosphere. When an additional supply of membrane area is integrated into the model, the membrane remains in an un-stretched state at zero tension until the area reservoir is depleted. Even at small "pre-strains" of only a few percent, the tension is significantly reduced at $p = 1$ atm. At pressures less than that required to use up the excess area, p^*, the cell wall is solely responsible for resisting the internal pressure. The lack of a secondary stress-bearing lamina leads to increased areal and volumetric strains when biologically relevant parameters are selected, as shown in Fig. 2.5. While the overall area-stretch of the composite shell is seen to rise, the membrane stretch is lessened by the "pre-strain" ϵ_0.

Interestingly, excess membrane area alters the way in which the cell expands. As the membrane can only sustain a state of isotropic tension it encourages uniform deformation, a behavior that is opposed by the anisotropy of the peptidoglycan layer. When the bilayer contribution is nullified under "pre-strain" conditions, the strongly anisotropic peptidoglycan network encourages cell elongation.

When both lamina are connected and deform together, the conflicting deformation agendas of the membrane and wall require the cell wall anisotropy, α, to be especially large in order to exhibit strong axial deformation. A membrane "pre-strain" diminishes the effect of the membrane's preference for isotropic deformation, lessening the lower bound on α. As seen in Fig. 2.5 (d), a pre-strain of $\epsilon = 5\,\%$ shifts the strain curves ($\epsilon_z = \epsilon_\theta$ and $\epsilon_\theta = 0$), such that a lower α can reproduce large axial strains. This less stringent requirement allows α to take on a value that is in closer agreement with prior estimates [1]. However, if we consider the limiting case where $K_A \to 0$ (cell wall alone bears the pressure load), and also make the reasonable assumption that $\epsilon_z > 2\epsilon_\theta$, we again recover the requirement that $\alpha > 4$ for all valid ν. This indicates that while excess membrane area or a smaller K_A value allow the cell to expand further without threatening membrane rupture, the requirement that $\alpha > 4$ remains.

2.4 Discussion

A composite thin shell model consisting of a lipid bilayer membrane and peptidoglycan cell wall was constructed to investigate the mechanics of bacterial cells under internal turgor pressure, and determine the elastic properties of the anisotropic cell wall. The mechanics of the cell envelope in bacteria are hypothesized to play a vital role in failure mechanisms of cells subjected to variations in pressure induced by osmotic shock. Prior bacterial mechanics research depicts the cell wall as the exclusive stress-bearing structure, though it is known that the inner membrane must take a portion of the load, as tension is required to gate MS channels that act to release internal pressure. The continuum approach taken herein finds that by coupling the mechanical deformation of the two layers, the fluid membrane makes significant stress-bearing contributions, such that the cell wall is not exclusively responsible for resisting structural loads. Furthermore, it is found that the peptidoglycan framework composing the cell wall displays a circumferential Young's modulus that is far greater than that in the axial direction (Fig. 2.4). Experimental evidence has shown that extension and contraction under pressure variations of bacteria such as *E. coli* occurs primarily in the axial direction, believed to be a consequence of the relatively stiff glycan strands that form hoop-like structures along the circumference of the cell. To emulate this behavior, the ratio of elastic moduli E_θ/E_z must be larger than previous findings have shown (Fig. 2.4).

By introducing a membrane component into the mechanics model, we are able to investigate how membrane tension behaves as a function of pressure. This relationship is of vital importance when studying how cells respond to osmotic shocks, as tension-dependent channels located within the membrane regulate the transport of water and solute, allowing the cell to survive large fluctuations in pressure. Previous research has focused primarily on cell wall mechanics, and how the interaction between the membrane and wall influences cell mechanics is largely unknown. Our results show that the membrane plays a significant structural role, and future work utilizing composite models may lead to an understanding of how failure mechanisms such as blebbing and rupture occur.

The model shows that the cell wall in rod-shaped bacteria has a circumferential elastic

modulus that is several multiples larger than its axial modulus, specifically it must be at least four times larger for the axial strain to exceed the hoop strain. Furthermore, our study of the relationship between the elastic constants and Poisson ratios (Section 2.3.2) can provide guidance to experimentalists looking to measure mechanical properties of the cell wall. Bacteria unsurprisingly grow along their axis in a similar manner to how they expand under pressure. An understanding the anisotropic material properties of the wall can further endeavors in the field of how the disorded network is arranged, and how this relates to cell growth.

We also consider that when a cell is under standard turgor pressure, there may be a small amount of excess membrane area stored in folds, such that the membrane is not fixed to the cell wall. This would allow the cell to expand without stretching the membrane until the excess is depleted, at which point it would attach to the cell wall and the two layers would deform together. Since the membrane does not bear any of the internal pressure load until it attaches to the wall, a reduction in tension is seen, and tensions required for rupture are not reached until the cell is under several atmospheres of pressure. Furthermore, areal and volumetric strains are seen to increase when the membrane does not contribute to bearing the initial pressure load, and the material properties of the extensible cell wall leads to more prominent axial deformation. With a "pre-strain" parameter included in the model, not only do the strains and stresses align more closely with experimental results, but the minimum requirement on α is lowered, placing it closer to values previously determined by AFM and molecular dynamics.

Axially directed peptide links are generally thought to exist in a disordered state. As a cell is placed in a hypotonic solution and water is drawn into the cytoplasm, these strands are hypothesized to align and stretch to their full potential, explaining the elastic nature of the cell in the longitudinal direction. Moreover, the orthogonal glycan hoops appear to undergo stress stiffening (requiring a non-linear material model), encouraging a pressurized cell to expand longitudinally. Both layers form a composite material that exhibits time-dependent viscoelastic characteristics. Future studies may explore the active mechanical properties of the bacterial cell wall that are modified as the cell grows and undergoes changes induced by

pressure, solute concentration, and damage.

CHAPTER 3

Transport

Most cells live in a watery medium filled with the key ions that make life possible. However, sometimes these cells are subjected to sudden changes in their osmotic environment that can result in the damaging flow of water in or out of the cell, resulting in changes in volume and mechanical stresses on the cell wall and bounding membranes. A class of channels within the bacterial inner membrane known as mechanosensitive channels have been shown to provide osmoprotection to cells subjected to these shocks, whereas cells that have been deprived of their entire complement of mechanosensitive channels can die when subjected to such shocks. In this section we explore a physical model of the osmotic shock response of bacterial cells and examine the build up of tension after such a shock as a function of key control parameters such as the number of channels of each type and the rate at which the shock is prescribed. These results allow us to predict channel survivability as a function of these key control parameters.

Interestingly, cells from all domains of life are equipped with a class of membrane proteins known as mechanosensitive (MS) channels that are gated by tension in the surrounding membrane. In *E. coli* alone, there are seven distinct MS channels [22], with the number of copies of each type ranging from a few to well into the thousands [3, 23]. While the "large" (MscL) and "small" (MscS) conductance channels are known to play the role of emergency pressure release valves [24], the functions of other channel types, such as the MscS homologs MscK and YbdG, are not well characterized. It has been hypothesized that these other channels activate under certain environmental conditions to selectively release specific ions, as is the case for the potassium channel MscK. Furthermore, a variety of experiments demonstrate that in the absence of the full complement of these channels, cells

subjected to osmotic shock do not survive [25, 26, 27, 9, 28, 21]. However, other experiments have shown that overexpressing *ybdG* can provide a high level of osmoprotection, provided the channels are present in large enough numbers, indicating an apparent redundancy in function between different channel types.

Thus, the situation is complicated: the survival of a cell depends not only upon which channels are present, but also on how fast the shock is applied and how many channels decorate the cell's inner membrane [9, 28, 21]. As a result, we were inspired to undertake both experimental and theoretical studies that allow us to explore bacterial response as a function of these key parameters. The results of our systematic experiments in which we control both channel number and shock rate will be presented elsewhere, while here we focus on a theoretical study to see if we can relate the number of channels, their conductivity, and which ones are present, to volume change. Specifically, we use the volume change as a window onto membrane tension and use the rupture tension as a way to assess bacterial survival probability.

We begin in Section 3.1 with a description of the mechanics of water and solute flow across the cell membrane and how these flows alter membrane mechanics and hence, the channel open probability. With the model formulation in hand, we then turn in Section 3.2 to an analysis of the implications of the model for different choices of the knobs that control the osmotic shock response of bacterial cells.

3.1 Model of Osmotic Transport

We study the variation of the volume enclosed within a complex membrane that may contain water channels (e.g., aquaporins) and solute channels (e.g., MscL), after an osmotic shock has been performed by changing the medium outside the membrane-enclosed structure. In the following, C_{in} (C_{ext}) will be used for the concentration describing the inside (outside) of the membrane-bound structure. The extracellular region with solute concentration C_{ext} will be thought of as a spatially uniform reservoir and dictated by experimental conditions (the osmotic shock).

In what follows, P_i and Π_i denote the hydrostatic and osmotic pressure in compartment i, respectively. We will use the ideal gas law for the osmotic pressure, namely, $\Pi_i = k_{\rm B}TC_i$, where C_i is the solute concentration in compartment i, though nonlinear corrections might be needed to treat concentrations found in some experiments. Inside the cell, $C_{\rm in} = N/V$ is related to the number of solute molecules $N(t)$ and the cell volume $V(t)$. Generically, we can compute the rate of change of the volume and solute number by using mass conservation in the form of flux laws, namely,

$$\dot{V} = -J_V, \tag{3.1}$$

$$\dot{N} = -J_N, \tag{3.2}$$

where the fluxes of volume J_V ($\mathrm{m^3 s^{-1}}$) and of solute J_N ($\mathrm{s^{-1}}$) are defined as positive when material goes from in $\rightarrow$ ext. Note that contrary to some conventional notation, here the quantities J_V and J_N are not reckoned on a per unit area basis and give us the total mass flow across the entire membrane.

3.1.1 Kedem-Katchalsky (K-K) Equations

The fluxes of solute and solvent across a flat, rigid membrane are phenomenologically related to gradients of osmotic and hydrostatic pressures by the K-K equations [29], which involve three parameters: a permeability to water μ, a permeability to solute α, and a reflection coefficient σ for the solute molecules contacting the membrane. In particular, these mass transfer rates are given by

$$J_V^{(i\rightarrow j)} = \mu((P_i - P_j) - \sigma(\Pi_i - \Pi_j)). \tag{3.3}$$

$$J_N^{(i\rightarrow j)} = \alpha(\Pi_i - \Pi_j) + (1-\sigma)C_{ij}J_V^{i\rightarrow j} \tag{3.4}$$

In (3.4), C_{ij} is the average of the concentrations C_i and C_j on either side of the membrane.

The meaning of the permeabilities (μ, α) is straightforward since they are simply mobilities which relate flows to gradients of chemical potentials (in the linear response approximation). With these definitions, the units of these transport coefficients are given by $[\mu] = \mathrm{m^3\,Pa^{-1}\,s^{-1}}$ and $[\alpha] = \mathrm{Pa^{-1}\,s^{-1}}$. The dimensionless reflection coefficient (σ), on the

other hand, is more subtle. From a phenomenological point of view, it can be understood by looking at particular limits [30]. When $\sigma = 0$, J_V is directly proportional to ΔP, which is the equivalent of Darcy's law for the flow across a porous medium, with no osmotic effect. This case thus corresponds to a membrane perfectly permeable to both water and solute (or to no membrane at all). When there is no solvent flow ($J_V = 0$), eqn. 3.3 and 3.4 gives $\Delta P = \sigma \Delta \Pi$, which means that one needs to apply an osmotic pressure difference proportional to the hydrostatic pressure difference in order to prevent water flow as a response to an osmotic gradient. If $\sigma = 1$, it gives $\Delta P = \Delta \Pi$, which is the Van't Hoff relation for an ideal semi-permeable membrane (hence the name *reflection* coefficient). It is clear that in this case, $\alpha =$ (no solvent flux), so α and σ are clearly related, but they can be varied independently [31]. Intuitively, we see that when $\sigma = 0$, this means that solute molecules are free to cross the membrane, going along for the ride with water molecules as is seen in equation (3.3), even if there is no osmotic gradient. For the case in which $\sigma = 1$, even if there is water flow, no solute molecules will be carried along by the water. Also, for this case, as seen in equation (3.4), there will be a flow of water across the membrane whenever there is a concentration gradient of solutes.

3.1.2 Separating membrane and channel fluxes

A difficulty arises when applying the K-K equations ((3.3) and (3.4)) to the mechanosensitive (MS) bacterial interface. While the permeabilities and reflection coefficient remain fixed for the inner membrane itself, they are tension-dependent for mechanosensitive channels. To deal with this we can separate the fluxes through the membrane from those through the channels by defining separate transport parameters for each case.

Lipid membranes such as the inner membrane found in bacterial cells, are to some extent permeable to water, while they are largely impermeable to ions and proteins [32]. Accordingly, we model the membrane as an ideal semi-permeable barrier, with constant water permeability μ^{m}, solute permeability $\alpha^{\mathrm{m}} = 0$, and reflection coefficient $\sigma^{\mathrm{m}} = 1$. With these choices the membrane contribution to solute flux vanishes in equation (3.4), while any dif-

ference in hydrostatic and osmotic pressures between the inner and outer compartments will lead to volume exchange through the membrane.

In contrast to the lipid bilayer, mechanosensitive channels permit the passage of both water and osmolytes, and their permeabilities (μ^{c} and α^{c}) and reflection coefficient ($0 \leq \sigma_{\mathrm{c}} \leq 1$), depend upon membrane tension τ. Therefore, the solute flux is confined solely to the channels, while the total water flux becomes a composition of membrane and channel parts

$$\begin{aligned} J_V^{(i\to j),\mathrm{m}} &= \mu^{\mathrm{m}}((P_i - P_j) - (\Pi_i - \Pi_j)) \\ J_V^{(i\to j),\mathrm{c}} &= \mu^{\mathrm{c}}((P_i - P_j) - \sigma(\Pi_i - \Pi_j)) \\ J_N^{(i\to j),\mathrm{m}} &= 0 \\ J_N^{(i\to j),\mathrm{c}} &= \alpha^{\mathrm{c}}(\Pi_i - \Pi_j) + (1-\sigma^c)C_{ij}J_V^{i\to j,\mathrm{c}}. \end{aligned} \tag{3.5}$$

The water permeability through the membrane μ^{m} describes the average properties of the entire membrane. However, the channel parameters depend on the number and variety of channels present in their opened state. For the situation where multiple types of channels present, equation (3.5) will be modified such that each channel type has its own volume and solute flux, and the total fluxes are their sum.

3.1.3 Mechanosensitivity of the Channel Parameters

For two-state models of ion-channel gating, the opening probability is generally of the form

$$\mathcal{P}_{\mathrm{open}} = \frac{e^{-\beta(\epsilon_{\mathrm{open}} - \Delta G_{\mathrm{driving}})}}{e^{-\beta(\epsilon_{\mathrm{open}} - \Delta G_{\mathrm{driving}})} + e^{-\beta\epsilon_{\mathrm{closed}}}}, \tag{3.6}$$

where $\beta = 1/k_{\mathrm{B}}T$, ϵ_{open} and $\epsilon_{\mathrm{closed}}$ are the energies of the open and closed states of the channel, respectively, and $\Delta G_{\mathrm{driving}}$ is the free energy contribution coming from the driving force (e.g. voltage, tension, ligand concentration) that tilts the free energy balance in favor of the open state. For the tension-driven case considered here, this leads to

$$\mathcal{P}_{\mathrm{open}}(\tau) = \frac{e^{-\beta(\epsilon_{\mathrm{open}} - \tau\Delta A)}}{e^{-\beta(\epsilon_{\mathrm{open}} - \tau\Delta A)} + e^{-\beta\epsilon_{\mathrm{closed}}}}, \tag{3.7}$$

where $\Delta A = A_{\mathrm{open}} - A_{\mathrm{closed}}$. The opening probability of MS channels described by equation (3.7) and shown in Fig. 3.1 follows a sigmoidal curve with an open probability of zero at low

membrane tension and unity at high membrane tension, characterized by a gating tension $\tau^* = (\epsilon_{\text{open}} - \epsilon_{\text{closed}})/\Delta A$ at which the probability is equal to one half, and a "sensitivity" $\delta\tau = 1/(\beta\Delta A)$ as the tension scale over which the probability changes significantly. However, the specific choice of gating function probably makes little difference since the essence of such a function is simply the change in membrane permeability with tension. The key features of this mechanosensitivity function are that it vanishes in the low tension limit, reaches one in the high tension limit, and transitions between these two states over some relatively narrow tension range.

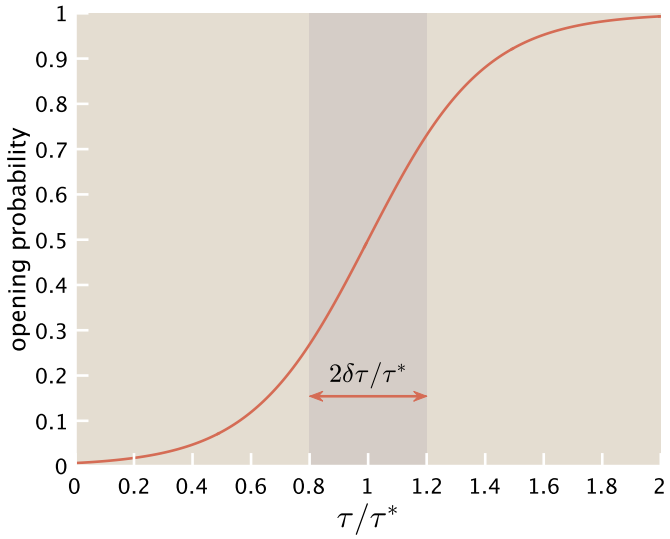

Figure 3.1: The channel opening probability as a function of membrane tension, assuming a thermodynamic equilibrium.

In the model, we consider the solute and water transport contributions from three varieties of MS channels: MscL, MscS, and YbdG. Each of these channel types has a unique set of transport properties that are dependent on their size, population, gating threshold. We first define reference quantities μ_0^c, α_0^c, and σ_0^c as the cell-wide properties of a single channel type in its fully opened state. These reference quantities are calculated using channel flow equations and literature values of pore size, gating tension, and channel populations. Membrane and MS channel parameters used herein are given in Table 3.3, while further discussion of the values is provided in the appendix. The permeability parameters of channel i

as functions of membrane tension τ_{m} then satisfy

$$\mu_i^{\mathrm{c}}(\tau_m) = \mu_{0,i}^{\mathrm{c}}\mathcal{P}_{\mathrm{open},i}, \qquad \alpha_i^{\mathrm{c}}(\tau_m) = \alpha_{0,i}^{\mathrm{c}}\mathcal{P}_{\mathrm{open},i}, \qquad \sigma_i^{\mathrm{c}}(\tau_m) = 1 - (1 - \sigma_{0,i}^{\mathrm{c}})\mathcal{P}_{\mathrm{open},i}. \tag{3.8}$$

On a cell-wide basis, the channel permeabilities are obtained by summing contributions from each type of channel (i.e., $\mu^{\mathrm{c}} = \sum_i \mu_i^{\mathrm{c}}$, etc.). In light of the various definitions and assumptions laid out above, we can write the kinetic equations for water and solute flow as

$$\dot{V} = -\left((\mu^{\mathrm{m}} + \sum_i \mu_i^{\mathrm{c}})\Delta P - (\mu^{\mathrm{m}} + \sum_i \mu_i^{\mathrm{c}}\sigma_i^{\mathrm{c}})\Delta\Pi\right), \tag{3.9}$$

and

$$\dot{N} = \sum_i \left(-\alpha_i^{\mathrm{c}}\Delta\Pi + (1 - \sigma_i^{\mathrm{c}})C_{ij}\mu_i^{\mathrm{c}}(\sigma_i^{\mathrm{c}}\Delta\Pi - \Delta P)\right). \tag{3.10}$$

3.1.4 Constitutive Relationships

For the case of a hypoosmotic shock considered here, the water flow into the cell leads to a surge in hydrostatic pressure that stretches the cell envelope and results in an increase in membrane tension. This tension, in turn, is what drives channel gating and hence leads to transient changes in the permeability of the membrane to solutes and water. As a result, we need to describe the mechanical response of the membrane itself. Furthermore, the cell wall provides additional structural support in sustaining the internal pressure load, and its mechanics can be modeled using continuum elasticity theory. Then, to couple the mechanics of the membrane and cell wall, we assume that the two layers form a composite shell and remain in contact as they deform, such that the strains are equal in each lamina. In the following we derive relationships between membrane tension, pressure, and cell volume that can be inserted into equations (3.9) and (3.10) to provide a connection between osmotic transport and the mechanical response of the cell.

Spherical Geometry

We begin by considering an idealized mechanical model with spherical geometry and isotropic cell wall properties. As the cell expands the fractional increase in surface area to first order is

$\Delta A/A_{\text{ref}} = 2\Delta R/R_{\text{ref}} = 2\epsilon$, where $\epsilon \equiv \Delta R/R_{\text{ref}}$. At high tensions $\gtrsim 0.1 k_{\text{B}}T/\text{nm}^2$ consistent with MS channel gating, increases in membrane area are related to a reduction in lipid surface density and are directly proportional to tension [18]. Therefore, we can write a Hookean relationship between membrane tension and area, specifically, $\tau_m = K_A^m(A - A_{\text{ref}})/A_{\text{ref}}$, where K_A^m is the area-stretch modulus, A is the area, and A_{ref} is the reference area. Then, applying the assumption that the PG cell wall behaves as an isotropic elastic solid yields a tension-area relation akin to that of the membrane, $\tau_w = K_A^w \Delta A/A_{\text{ref}}$, where $K_A^w \equiv Eh/2(1-\nu)$ is the wall stretch modulus, E is the elastic modulus, h is the thickness, and ν is the Poisson's ratio. Adding the two tension-area constitutive expressions we obtain the tension in the composite shell $\tau = \tau_m + \tau_w = (K_A^m + K_A^w)\Delta A/A_{\text{ref}}$. By defining a normalized volume $v = V/V_{\text{ref}}$, the tensions in each layer can be expressed in terms of volume,

$$\tau_m = \frac{2}{3}K_A^m(v-1), \qquad \tau_w = \frac{2}{3}K_A^w(v-1), \tag{3.11}$$

and the fractional change in volume is $\Delta V/V_{\text{ref}} = v - 1 = 3\Delta R/R_{\text{ref}}$.

In order to close the problem, we need a relationship between size (the volume) and Laplace pressure, P_L. To satisfy mechanical equilibrium the combined stresses in the membrane and cell wall τ must balance the pressure difference between the cell and its surrounding medium. We can then write the jump in hydrostatic pressure across the composite shell as the Laplace pressure, namely, $P_{\text{in}} - P_{\text{ext}} = 2\tau/R \equiv P_L$, with R the radius of curvature of the cell envelope. Substituting the composite tension above into the Laplace pressure gives

$$P_L = \frac{2}{3}K(v-1), \tag{3.12}$$

where $K = 2(K_A^m + K_A^w)/R_{\text{ref}}$. The membrane tension may also be written as the Laplace-Young equation with a renormalized stiffness

$$K_A^* = K_A^m + K_A^w, \qquad \rightarrow \qquad \tau_m = \frac{K_A^m}{K_A^*}\frac{P_L R}{2}. \tag{3.13}$$

Cylindrical Geometry

The spherical model neglects two important features, the effects of which we also wish to assess. First, in contrast to spherical GUVs, bacterial cells such as *E. coli* are closer to sphe-

rocylindrical. Second, this *morphological anisotropy* is matched by a *structural anisotropy*: the cell wall is more compliant when stretched along the long axis of the cell than perpendicular to it.

A standard result from the engineering mechanics of cylindrical pressure vessels tells us that the pressure jump across the composite shell gives rise to a tension $f_z = P_L R/2$ along the axis, which is half of that in the perpendicular (hoop) direction $f_\theta = P_L R$. These tensions are balanced by the internal membrane tension τ_m and the cell wall tensions $\tau_{z,\theta}$,

$$f_z = \frac{P_L R}{2} = \tau_m + \tau_z, \qquad f_\theta = P_L R = \tau_m + \tau_\theta. \tag{3.14}$$

These relations are a consequence simply of cylindrical geometry. For the composite cylindrical shell, we model the structurally anisotropic cell wall by assuming a general 2-D (orthotropic) Hookean relationship between the wall stress resultants (τ_z, τ_θ) and strains $(\epsilon_z, \epsilon_\theta)$, along with the membrane isotropic response,

$$\begin{bmatrix} \epsilon_z \\ \epsilon_\theta \end{bmatrix} = \frac{1}{E_z h} \begin{bmatrix} 1 & -\nu_{\theta z} \\ -\nu_{\theta z} & E_z/E_\theta \end{bmatrix} \begin{bmatrix} \tau_z \\ \tau_\theta \end{bmatrix}, \qquad \tau_m = K_A^m \frac{\Delta A}{A_{\text{ref}}}, \tag{3.15}$$

where E_z and E_θ are the Young's moduli in the axial and perpendicular (hoop) directions, $\nu_{\theta z}$ is a Poisson's ratio, and h is the wall thickness. The cylindrical strains are

$$\epsilon_z = \frac{\Delta L}{L_{\text{ref}}}, \qquad \epsilon_\theta = \frac{\Delta R}{R_{\text{ref}}} \tag{3.16}$$

and can be related to the area and volume change as

$$\frac{\Delta A}{A_{\text{ref}}} = \epsilon_z + \epsilon_\theta, \qquad \frac{\Delta V}{V_{\text{ref}}} = \epsilon_z + 2\epsilon_\theta. \tag{3.17}$$

Equations (3.14)–(3.17) are solved to obtain a composite constitutive law for pressure, membrane tension, and volume,

$$\tau_m = \frac{K_A}{K_A^*} \frac{P_L R}{2}, \qquad K_A^* = K_A \frac{1 - 2\nu + \frac{E_z}{E_\theta}(1 + \frac{hE_\theta}{K_A})}{1 - 3\nu + 2\frac{E_z}{E_\theta}} \tag{3.18}$$

$$v - 1 = \frac{1}{K} P_L, \qquad K = \frac{2K_A}{R} \frac{1 + \frac{E_\theta}{E_z}(1 - 2\nu_{\theta z} + \frac{hE_z}{K_A})}{4 + \frac{E_\theta}{E_z}(1 - 4\nu_{\theta z}) + \frac{K_A}{hE_z}(1 - \frac{E_\theta}{E_z}\nu_{\theta z}^2)}. \tag{3.19}$$

Estimates

One remaining concern is whether it is reasonable to assume that the membrane and cell wall are in contact as osmotic pressure rises and causes the cell to deform. Under favorable environmental conditions that facilitate growth, a cell maintains turgor pressure that is set by the solute concentration difference between the cell and its surrounding medium. Estimates for turgor pressure vary over a wide range from 10^4 to 3×10^5 Pa [1], and if this pressure is insufficient to press the membrane up against the cell wall then a gap between the two layers may exist. In *E. coli*, the periplasmic space between the inner and outer membranes is 10–40 nm thick, with greater spacing at the poles than along the length of the cell [33]. The cell wall resides within the periplasm approximately 5–10 nm from the outer membrane and has thickness $h \approx 5\,\text{nm}$, thus the region between the inner membrane and cell wall cannot exceed 15–20 nm in width. If this gap does exist, then any subsequent rise in pressure will be solely sustained by the membrane until it stretches sufficiently to fill the vacant region between both laminae. The tension associated with this in-plane stretch from a gap width of 5 nm, assuming a spherical membrane of radius $R_0 = 1\,\mu\text{m}$ and tension-area relationship $\tau_m = K_A \epsilon_A = K_A(R^2/R_0^2 - 1)$, is $\tau_m \approx 0.5\, k_\text{B}T/\text{nm}^2$, exceeding the gating thresholds of several classes of MS channels. Furthermore, the pressure change consistent with this tension is on the order of 10^{-2} atm, which is 10 to 100 times less than turgor pressure, and even smaller compared to the osmotic pressures encountered in standard downshock experiments. As channel gating tensions should not be attained by such small fluctuations in pressure, we can conclude that if any gap exists between the inner membrane and cell wall it must be less than a few nanometers, and any subsequent increase in pressure will push the membrane in contact with the cell wall, and the two layers will continue to deform together allowing the cell wall to contribute to resisting the pressure load.

In light of the conclusion that the inner membrane and cell wall deform as a composite shell with equal strains in both layers, naturally the next step is to investigate the stresses. Of specific interest is the relative stress-bearing contribution of each layer, and whether one layer plays a dominant role. One way to compare the stiffnesses of the two laminae is through

their resistance to in-plane stretching, which is defined by their area-stretch moduli. If we make the naive assumption that the cell wall is homogeneous, isotropic, and obeys Hooke's law, the area-stretch modulus can be written as $K_A^w = Eh/2(1-\nu)$. The elastic modulus E of the peptidoglycan network constituting the cell wall has been inferred by means of AFM and has an estimated value of $\approx$ 25–100 MPa [1, 2]. Though the Poisson ratio ν has not been reliably measured, we can choose a typical value of 0.25, which along with thickness $h = 5$ nm leads to $K_A^w \approx 20 - 100\, k_{\mathrm{B}}T/\mathrm{nm}^2$. Interestingly this result shows that K_A^w is comparable in magnitude to K_A^m, validating the use of a composite model that considers the cell wall and inner membrane to determine the mechanical response of the cell under pressure.

Finally, the Laplace pressure P_L dictates the stresses and strains in the cell envelope during an osmotic shock, which ultimately determine whether or not a cell remains mechanically viable. We can estimate the pressures associated with channel gating and membrane failure by taking experimentally determined critical values of membrane tension and plugging them into the modified composite Laplace-Young relation derived above (3.13). Experiments on giant spheroplasts have shown that gating of the largest channel MscL requires a bilayer tension of $\tau_m^{\mathrm{gate}} \approx 2.5\, k_{\mathrm{B}}T/\mathrm{nm}^2$, just beneath the rupture limit of $\tau_m^{rupture} \approx 3.5\, k_{\mathrm{B}}T/\mathrm{nm}^2$. Consequently, tensions between these two thresholds are expected during large, survivable downshocks, and the corresponding pressures are within the range 0.3 to 2.5 atm, depending on the specific choice of mechanical properties. Notably, this estimate demonstrates that the pressures required for membrane rupture are relatively small, on the order of turgor pressure, and roughly an order of magnitude lower than the osmotic pressure induced in standard shock experiments. Thus, the bilayer's limited extensional capacity prevents large increases in hydrostatic pressure even if the osmotic pressure is large.

Nondimensionalization, Reference State, and Active Transport

In order to reduce the number of parameters, we normalize equations (3.9) and (3.10) by writing various parameters in dimensionless form. This requires us to define a reference configuration, which we choose to correspond with a state where the membrane is unstretched,

and any further swelling will place the membrane under tension. Therefore, we begin nondimensionalizing by defining the reference volume V_{ref} as the cell volume where membrane tension vanishes. All other volumes are then normalized by scaling them to V_{ref}. Next, we set the initial concentration of solute molecules within the cell as C_{ref}, which allows us to write a similar rescaling for the number of solute molecules, $N_{\text{ref}} \equiv V_{\text{ref}} C_{\text{ref}}$. The reference pressure is defined through a rescaling of the reference concentration by $k_{\text{B}}T$, $P_{\text{ref}} \equiv C_{\text{ref}} k_{\text{B}} T$. As a result, we rescale all pressures including the composite stretching coefficient K by dividing by P_{ref}. Lastly, channel permeabilities μ^{c} and α^{c}, and time t are normalized by the water permeability of the membrane μ^{m}. Rewriting all of these parameters in dimensionless form, we have

$$\begin{aligned} v &\equiv \frac{V}{V_{\text{ref}}} \qquad p_i \equiv \frac{P_i}{P_{\text{ref}}} \qquad c_i \equiv \frac{C_i}{C_{\text{ref}}} \qquad n \equiv \frac{N}{N_{\text{ref}}} \\ k &\equiv \frac{K}{P_{\text{ref}}} \qquad \bar{t} \equiv \frac{\mu^{\text{m}} P_{\text{ref}}}{V_{\text{ref}}} t \qquad \bar{\mu}_i \equiv \frac{\mu_i^{\text{c}}}{\mu^{\text{m}}} \qquad \bar{\alpha}_i \equiv \frac{\alpha_i^{\text{c}}}{\mu^{\text{m}} C_{\text{ref}}}. \end{aligned} \tag{3.20}$$

This implies that the normalized equations with a sum i over each channel type can be written as

$$\dot{v} = -\left(1 + \sum_i \bar{\mu}_i\right) p_L + \left(1 + \sum_i \bar{\mu}_i \sigma_i\right) \left(\frac{n}{v} - c_{\text{ext}}\right) \tag{3.21}$$

and

$$\dot{n} = -\left(\frac{n}{v} - c_{\text{ext}}\right) \sum_i \bar{\alpha}_i + \frac{1}{2}\left(\frac{n}{v} + c_{\text{ext}}\right) \sum_i (1 - \sigma_i)\, \dot{v}_i^{ch}. \tag{3.22}$$

In (3.22), the average of the internal and external concentrations c_{ij} is written as $c_{ij} = (n/v + c_{\text{ext}})/2$, p_L is the normalized Laplace pressure, and the rate of flow through channel i is

$$\dot{v}_i^{ch} = \bar{\mu}_i \left(\sigma_i \left(\frac{n}{v} - c_{\text{ext}}\right) - p_L\right). \tag{3.23}$$

The direction of solvent flow determines whether the cell shrinks or swells, and it is dependent on the competition between the Laplace and osmotic pressures. This relationship is complicated by the channel reflection coefficients, but can be simplified by defining the *effective* osmotic pressure as

$$\pi^* \equiv \frac{1 + \sum_i \bar{\mu}_i \sigma_i}{1 + \sum_i \mu_i} \pi, \tag{3.24}$$

where $\pi = n/v - c_{\text{ext}}$ is the normalized osmotic pressure. Thus, shrinking and swelling of the cell requires $p_L > \pi^*$ and $p_L < \pi^*$, respectively. As written, equations (3.21) and (3.22) do not admit of intuitive analysis, but they have the virtue of being a highly simplified picture of the essential features of the dynamics of our membrane bound system after an osmotic shock.

To this point, we have assumed that the reference state is characterized by an unpressurized cell with respect to its surroundings, and both the membrane and cell wall are stress free. However, when *E. coli* cells are immersed in environments favorable to growth they maintain a near constant turgor pressure if the solute concentration of the surrounding medium does not undergo large fluctuations. Under these steady-state conditions, net flows of volume and solute are negligible. If this equilibrium is disturbed and the internal pressure decreases (e.g., hyper-osmotic shock), cells must accumulate solute molecules that, in turn, draw water into the cytoplasm and restore turgor. Therefore, cells must be equipped with some mechanism, such as a set of transmembrane ion transporters or pumps, that drives solutes against the concentration gradient into the cell. These "active" transporters require an energy source such as ATP to move solutes in the "uphill" direction, and are typically selective in terms of the ions that traverse them. While specific details of the mechanisms involved in active transport in *E. coli* remain unclear, we can nonetheless include a simple active transport term in (3.22), which will allow the model to maintain a small turgor pressure under steady-state conditions.

3.1.5 Values of the Parameters

Equations (3.21) and (3.22) involve five dimensionless parameters; three related to membrane transport: $(\bar{\mu},\ \bar{\alpha},\ \sigma)$, one related to the interfacial mechanics: k, and one related to the external perturbation: c_{ext}, which is the control parameter that dictates the cell's response. These normalized parameters are calculated using the reference quantities shown in Table 3.1.

Table 3.1: Parameters used in transport calculations. For the cylindrical model, cell wall properties are selected that lead to small hoop strains and much larger axial strains. For the spherical model, the elastic modulus is set equal to the average of the two moduli used in the cylindrical model.

Description	Symbol	Value
Radius	R_0	$0.5\,\mu m$
Length	L_0	$2\,\mu m$
Surface Area	A_0	$6.28\,\mu m^2$
Volume	V_{ref}	$1.57\,\mu m^3$
Concentration	C_0	$1.0\,M$
Pressure	P_0	$\sim 25\,atm$
Membrane stretch modulus	K_A^m	$50\ k_B T/nm^2$
Membrane thickness	h_m	$3\,nm$
Cell wall axial modulus	E_z	$8\,MPa$
Cell wall hoop modulus	E_θ	$80\,MPa$
Cell wall isotropic modulus	E_{iso}	$80\,MPa$
Poisson ratio	ν	0.25
Wall thickness	h	$6\,nm$
Membrane permeability	μ^m	$10^{-24}\ m^3/Pa/s$

Table 3.2: Protein counts in a single *E. coli* cell, adapted from [3]. Channel numbers are deduced based on the number of proteins and their structure.

Gene	MOPS 1	MOPS 2	MOPS 3	Structure	Channels per cell
mscL	2802	2481	1804	Pentameric	500
mscS	4271	2927	2193	Heptameric	500
ybdG	357	91	127	Heptameric	50

Table 3.3: MS channel parameters [4, 5, 6, 7].

Description	Symbol	MscL	MscS	MscM	Units
Pore diameter (open)	d_{op}	3.0	1.2	0.5	nm
Area difference	ΔA	7	5	4	nm^2
Free energy difference	ΔG	17.5	7.5	3	$k_{\mathrm{B}}T$
Gating tension	$\tau_{1/2}$	2.5	1.5	0.75	$k_{\mathrm{B}}T/\mathrm{nm}^2$
Water permeability	μ^{c}	6.6×10^{-25}	1.7×10^{-26}	5×10^{-28}	$\mathrm{m}^3\,\mathrm{Pa}^{-1}\,\mathrm{s}^{-1}$
Solute permeability	α^{c}	570	90	15	$\mathrm{Pa}^{-1}\,\mathrm{s}^{-1}$
Reflection coefficient	σ	0.01	0.05	0.5	

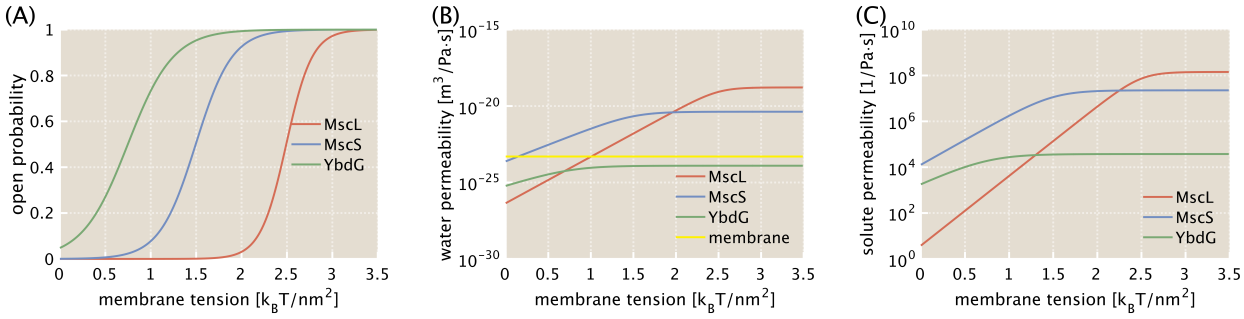

Figure 3.2: Open probabilities and permeabilities of MS channels through their gating tension transitions. (A) The open probability of each channel type. (B) Cell-wide water permeabilities of the MS channels and membrane. The channel permeabilities are calculated at the full cell level by multiplying a single channel permeability by its total population. (C) Total solute permeability of each channel.

3.2 Results

Response of the wild-type model cell to hypo-osmotic shock

In the simplest scenario a hypo-osmotic shock is applied to the model cell by starting from a stationary state with a given C_{ext}, and then abruptly reducing C_{ext} by the shock magnitude ΔC_{ext} at $t = 0$. In general, this is how osmotic shock unfolds experimentally, with typical values for the drop in external concentration ΔC_{ext} ranging from 0.1 – 1.0 M. We begin by simulating a sudden downshock of 0.5 M on a wild-type cell containing native populations of MscL, MscS, and YbdG (Figs. 3.3 & 3.4). Immediately after the shock is imposed at $t = 0$, the change in osmotic potential ($p_L < \pi^*$) generates an inward flow of water and the cell begins to expand. This initial influx of water occurs almost entirely through the lipid membrane with negligible transport via MS channels, and this behavior continues until the bilayer tension reaches the lowest channel gating transition ($\tau^* - \delta\tau/2$). The opening threshold of the smallest channel YbdG is reached first, followed by that of MscS, and finally MscL. As the gating probabilities increase and channels transition from their closed to open states, solute molecules are released from the cell leading to a reduction in intracellular concentration and osmotic pressure across the cell envelope. We note that it is not a requirement for any channel type to surpass its critical gating tension τ^* to release solute molecules, especially in situations where the shock magnitude is small. Simultaneous volume influx and solute efflux continue until the Laplace and effective osmotic pressures attain equilibrium ($p_L = \pi^*$), which coincides with peak values of cell volume, pressure, and membrane tension. At this point the direction of water flow is reversed from inward to outward as the Laplace pressure drives water out of the cell ($p_L > \pi^*$). In contrast to the membrane dominated influx of water, MS channels contribute significantly to the expulsion of water until the tension drops to levels sufficient to return them to their closed states. Solute flux remains outward throughout the hypo-osmotic shock response. As the cell continues to relax the outward flux of water and solute slows, and the cell volume decreases and tends asymptotically toward an equilibrium state where $p_L = \pi^*$.

In the preceding paragraph, we have described the general evolution of cell volume, solute

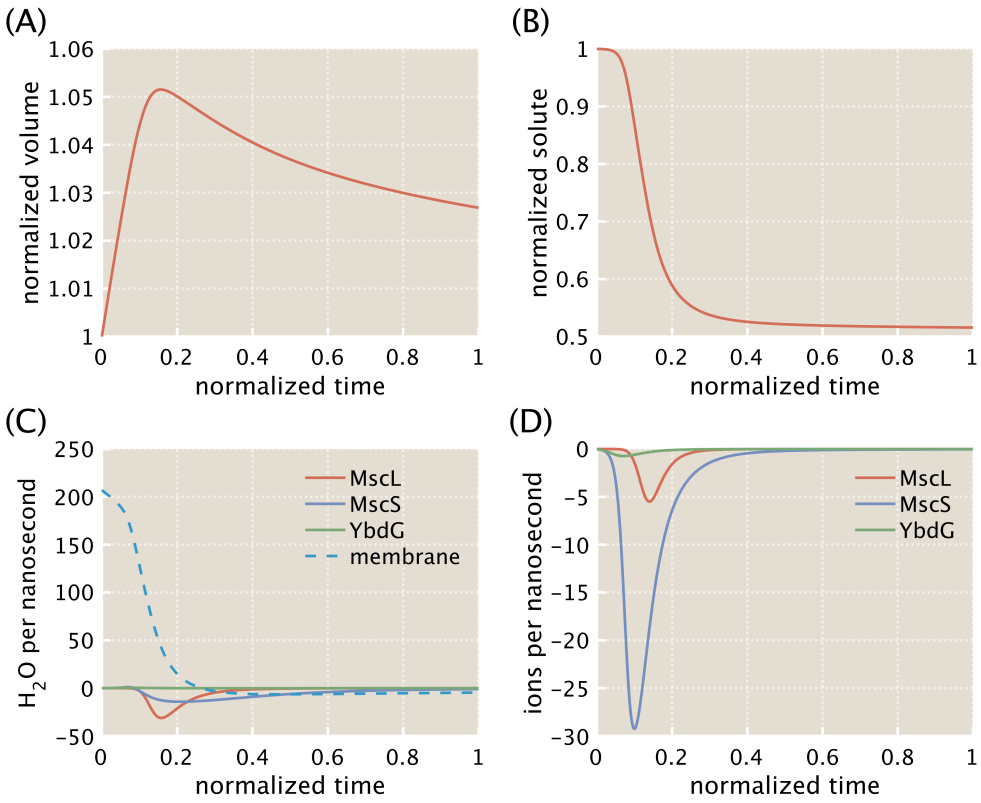

Figure 3.3: Evolution of cellular volume and solute in a downshocked cell containing full complements of all three channel types (WT strain). The external concentration decreases by 0.5 M at $t = 0$. (A) Normalized volume rapidly reaches its peak value, and then slowly decreases towards unity. (B) The normalized number of solute molecules remains nearly unchanged until channels open, at which point the solute concentration quickly decreases. Once channels begin to close, solute molecules slowly leak out of the cell and the internal concentration asymptotically approaches the external concentration. (C) Flux of water molecules through the membrane and MS channels. There is a short period of time where water is carried out of the cell by channels while simultaneously entering the cell through the membrane. This is a consequence of the channel reflection coefficients, and the ability of channels to transport both water and solute. (D) Flux of solute molecules through MS channels. YbdG contributes little to solute efflux due to its relatively small population and narrow pore, while on the other hand MscS is responsible for releasing the largest quantity of solutes.

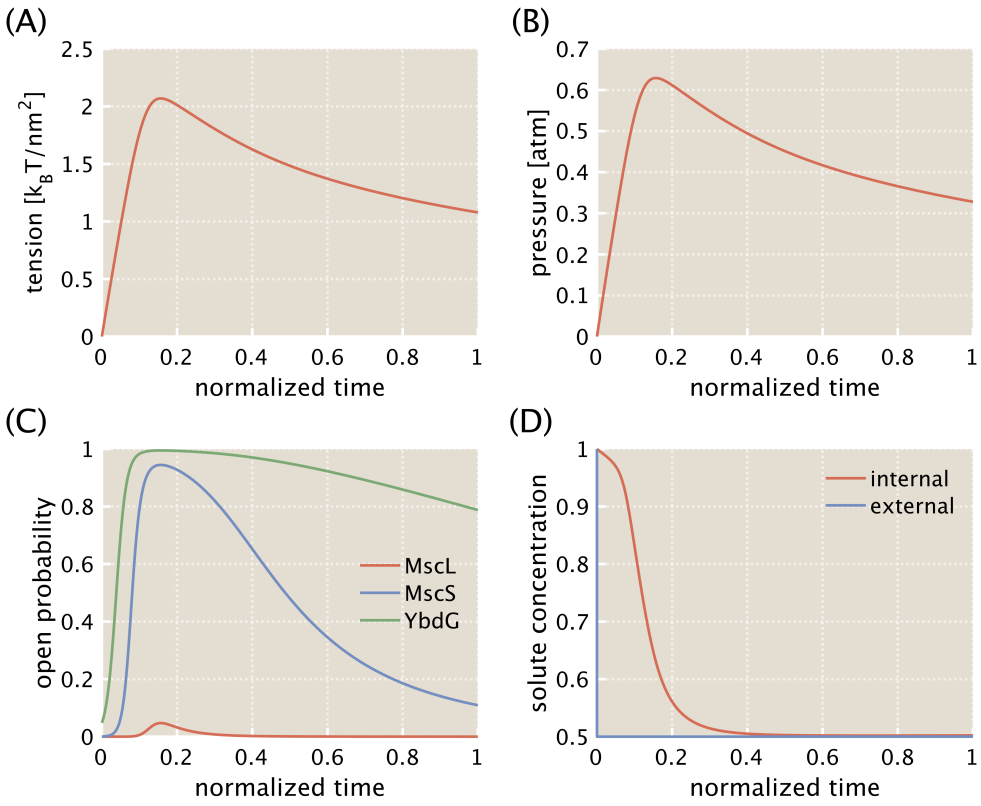

Figure 3.4: Temporal evolution of membrane tension (A), pressure (B), channel open probability (C), and solute concentration (D) of the WT model strain after a downshock of 0.5 M at $t = 0$. (A) Membrane tension remains beneath the lytic limit and reaches a peak value between the gating transitions of MscS and MscL. (B) Laplace pressure remains small relative to the osmotic pressure. (C) Open probabilities of each channel type. YbdG and MscS pass through their gating transitions, while only a small fraction of MscL channels gate. (D) The internal solute concentration rapidly decreases once channels open. When the majority channels close, the concentration slowly approaches external concentration from above.

concentration, pressure, and membrane tension in a hypo-osmotically shocked cell. Next, we point out some of the less obvious details that have important relationships with cell survivability. The model cell responds on sub-second time scales to the 0.5 M downshock, with the peak volume being attained within tens of milliseconds, in agreement with experimental estimates of 30 to 50 ms [34]. Partial solute equilibrium occurs within 100 ms of shock onset, slightly faster than previous estimates of $\sim$ 200 ms [34]. Fluctuations in cell volume remain relatively small throughout the hypo-osmotic shock, with peak values of volumetric strain barely exceeding 5 %, in line with prior research (references). Membrane tension reaches a maximum just above 2 $k_{\mathrm{B}}T/\mathrm{nm}^2$, above gating thresholds of YbdG and MscS, but beneath that of MscL. Furthermore, and of greater importance, membrane tension remains well below the rupture strength of 3.5 $k_{\mathrm{B}}T/\mathrm{nm}^2$, suggesting that a 0.5 M downshock likely does not lead to membrane failure in a WT cell with a full complement of channels.

One interesting feature, which should be conserved regardless of the details of the model, is that there is a maximum volume (hence a maximum tension) at some point in time, since volume increases after the shock and until channels open, and volume decreases (because of solute leakage) after channels have opened. The maximum tension shown in Figure 3.4 lies just beyond the channel opening transition region of membrane tension for MscS $\tau^* - \delta\tau/2 \rightarrow \tau^* + \delta\tau/2$, but other values of parameters can show a maximum tension far superior to $\tau^* + \delta\tau/2$, namely much higher than the critical tension for rupture. The interesting thing is that the value of this maximum tension (hence the likelihood of cell rupture) is not solely determined by the shock level, but also on factors that can vary from cell to cell, such as the level of initial stress, the number of channels, and shock rate.

What happens when the shock rate is varied?

Recent single-cell assays show that the rate of shock strongly influences cell viability, with survival probabilities increasing linearly with decreasing shock rate [9]. We can model the effects of rate dependence by imposing a linearly decreasing change in external concentration (i.e., $C_{\mathrm{ext}}(t) = -\dot{C}_{\mathrm{ext}}t + C_0$), with shock rate $\dot{C}_{\mathrm{ext}}$. A 0.5 M shock applied at a rate of 1/s

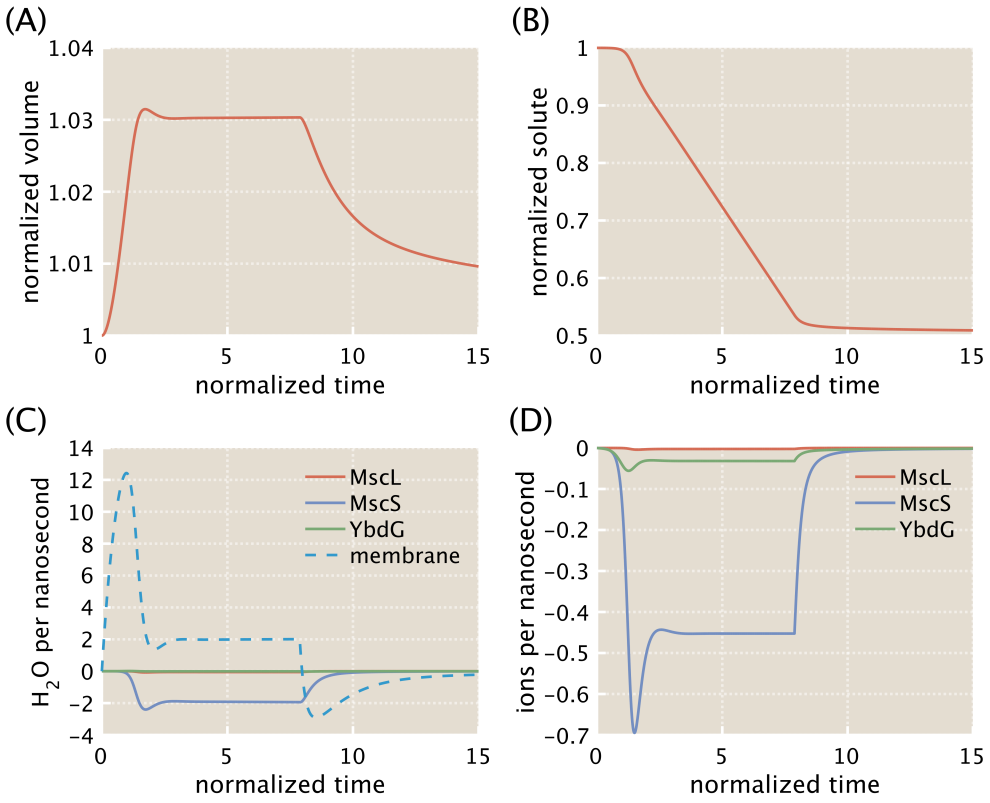

Figure 3.5: Progression of normalized cellular volume v and solute n and their fluxes in a cell subjected to a 0.5 M *linearly* varying downshock with shock rate 1/s. (A) Volume increases at the start of the shock, then decreases by a small amount before remaining at a near constant value for a period of time where $p_L = \pi^*$. The cell volume decreases once the shock ends. (B) Except for a brief period of time when the shock is initially applied, the amount of solute present in the cell decays at a constant rate until the shock ends. (C) During the period where the net exchange of volume is effectively zero the efflux of water through MS channels is matched by an equivalent influx of water through the membrane. (D) MscS has the largest contribution to discharge of solute molecules for this linear shock and specific choice of parameters. Membrane tension does not reach sufficiently high levels to gate a significant portion of MscL channels.

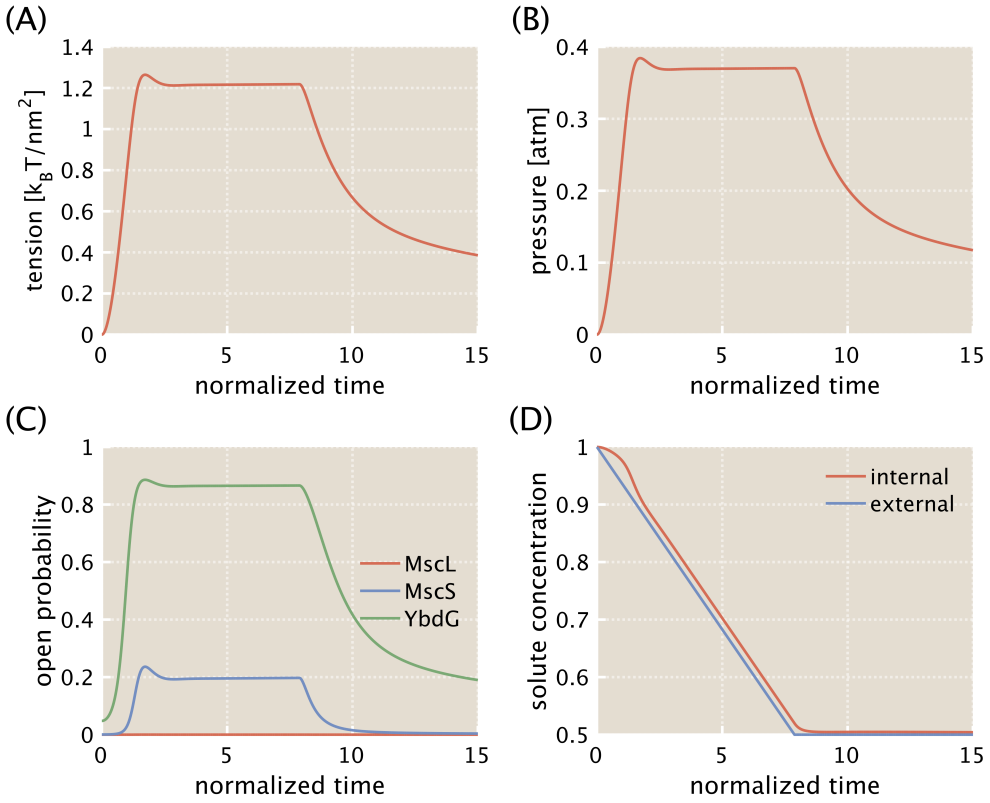

Figure 3.6: Membrane tension (A), Laplace pressure (B), channel open probability (C), and solute concentration (D) for a 0.5 M time-varying shock applied at a rate of 1/s.

leads to the response shown in Figs. 3.5 and 3.6.

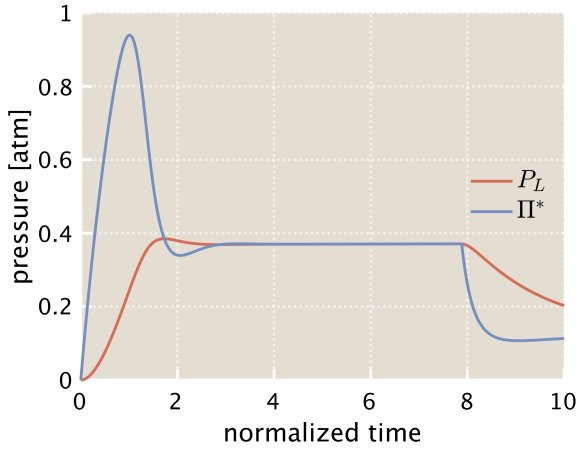

Figure 3.7: Progression of Laplace pressure P_L and effective osmotic pressure Π^* in a WT cell during a 0.5 M downshock applied at a rate of 1/s. After the shock is initiated at $\bar{t} = 0$ and a sufficient number of channels have gated, the cell reaches a state of pressure equilibrium ($P_L = \Pi^*$) that is maintained until the shock terminates at $\bar{t} \approx 8$.

The most obvious difference in the shock rate-dependent response of the model cell is the period of sustained pressure equilibrium where $P_L = \Pi^*$, and the net exchange of water between the cell and its surroundings is negligible (Fig 3.7). In other words, the intracellular concentration "keeps up" with the shock rate. Although net volume flux is zero, transport continues as membrane influx and channel efflux balance one another. Hydrostatic pressure, membrane tension, and channel opening probabilities are effectively constant throughout this stage. Another interesting feature is the small overshoot in volume, tension, and pressure immediately prior to the extended dynamic equilibrium as the cell takes on more water than necessary to equalize pressures across the cell envelope. This qualitative overshoot is diminished when the shock rate is slow ($\ll 0.1$)).

3.2.1 Survivability

Numerical results of several mutant strains subjected to a 0.5 M instantaneous shock are shown in this section. These mutants contain different combinations of the three channels

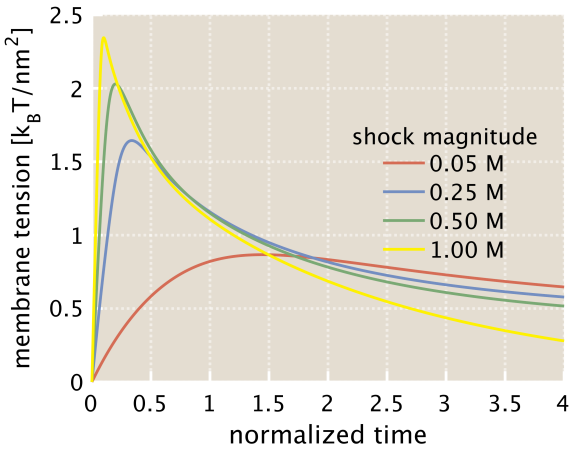

Figure 3.8: Membrane tension as a function of dimensionless time for various downshock magnitudes C_{ext}. Larger shocks have higher peak values of tension. Interestingly, since a larger shock imposed upon a cell leads to a greater abundance of gated channels, membrane tension decreases more rapidly than relative to a smaller shock once the maximum value is reached.

found in the model WT cell (MscL, MscS, and YbdG), with the requirement that at least one channel type is deleted. The results that follow within this section use parameters from Tables 3.1 and 3.3.

Mutants lacking both MscL and MscS are known to have difficulty surviving hypo-osmotic shocks $\gtrsim 0.05\,\text{M}$ [35, 36]. The simulated response of a double knockout model cell shows a near 30 % increase in volume, membrane tension ~ 4 times that required for rupture, and a much slower overall response time that exceeds 1 s. The double mutant's diminished solute efflux abilities require the cell to take on significantly more water than the single mutants to balance the concentration gradient. Although pressure equilibrium occurs within hundreds of milliseconds, solute and solvent efflux remain poor leading to sustained levels of tension above rupture.

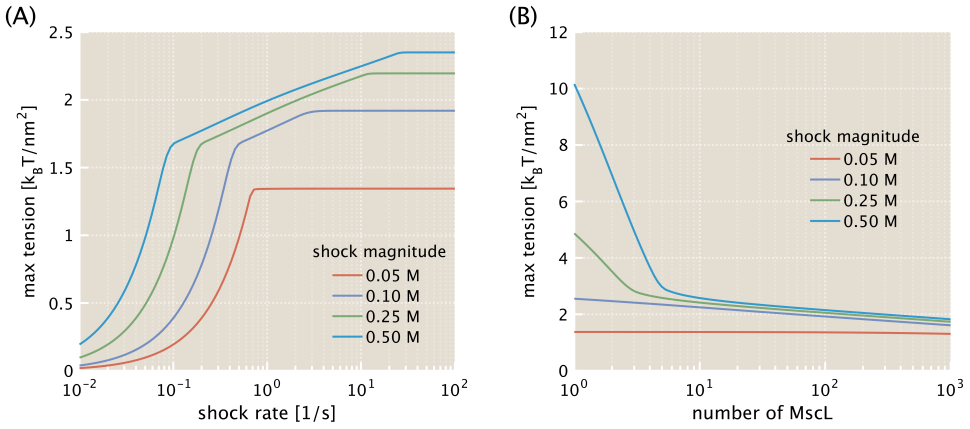

Figure 3.9: Variation of peak membrane tension with shock rate (A) and number of MscL channels (B), for various downshock magnitudes ΔC_{ext}. In both (A) and (B), the number of MscS and YbdG channels is set to zero such that MscL is the only channel type present. (A) The number of MscL channels is set to 300. For all shock magnitudes shown the maximum tension plateaus at some *fast* shock rate, and this tension is consistent with the peak value obtained during an instant shock. (B) The shock rate is set to 1/s. A cell requires fewer than 10 MscL channels to keep the membrane tension from exceeding the rupture limit of $3.5\,k_{\text{B}}T/\text{nm}^2$.

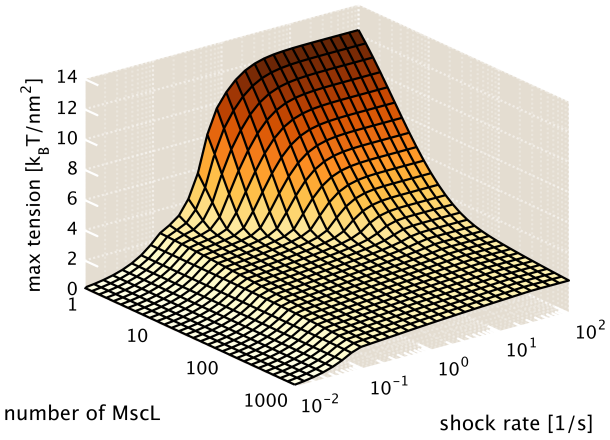

Figure 3.10: Peak values of membrane tension with varying shock rate and number of MscL channels. The downshock magnitude is 0.5 M and the populations of MscS and YdbG channels are set to zero.

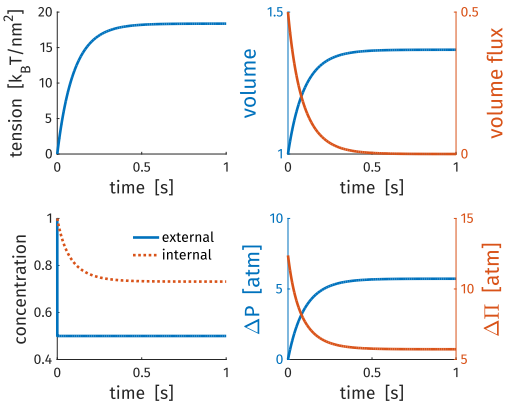

Figure 3.11: $\Delta mscL$ $\Delta mscS$ $\Delta mscM$: When no channels are present, solute cannot be released and water is drawn into the cell until $\Delta P = \Delta\Pi^*$.

Over-expression of YbdG reduces membrane tension and response time

Experiments indicate that survivability depends only weakly on the number of MS channels in a cell, unless both MscL and MscS are not present. As noted in Table 3.2, the number of "mini" channels in a single cell is roughly an order of magnitude lower than MscL and MscS, with some estimates falling as low as a few channels [25]. Here we further investigate how double knockout cells respond to osmotic shock, and vary the number of channels to simulate over-expression of *ybdG*. A previous study demonstrated that mutant cells lacking MscL, MscS, and MscK lose the ability to survive all but the smallest of shocks ($\sim$ 80% survival under a shock of 0.05 M) [35]. As the shock magnitude is increased to 0.25 M, survival probability dwindles to less than 10 %. However, over-expression of *ybdG* was shown to increase survival probability to values $\gtrsim$ 90 %. We first simulate the effect of two different shocks (0.05 M, 0.25 M) on a double mutant strain ($\Delta mscL$, $\Delta mscS$) , and then investigate the impact of over-expressing *ybdG*.

Under exposure to an instantaneous 0.05 M hypo-osmotic shock, the double mutant cell model reaches a peak tension just greater than 1.0 k_BT/nm^2, which falls well below what is required for membrane rupture (Fig. 3.12). The opening probability does not reach 100 % before channels begin closing, indicating that the cell is equipped with more than enough channels to regulate the shock. However, when the shock magnitude is raised to 0.25 M,

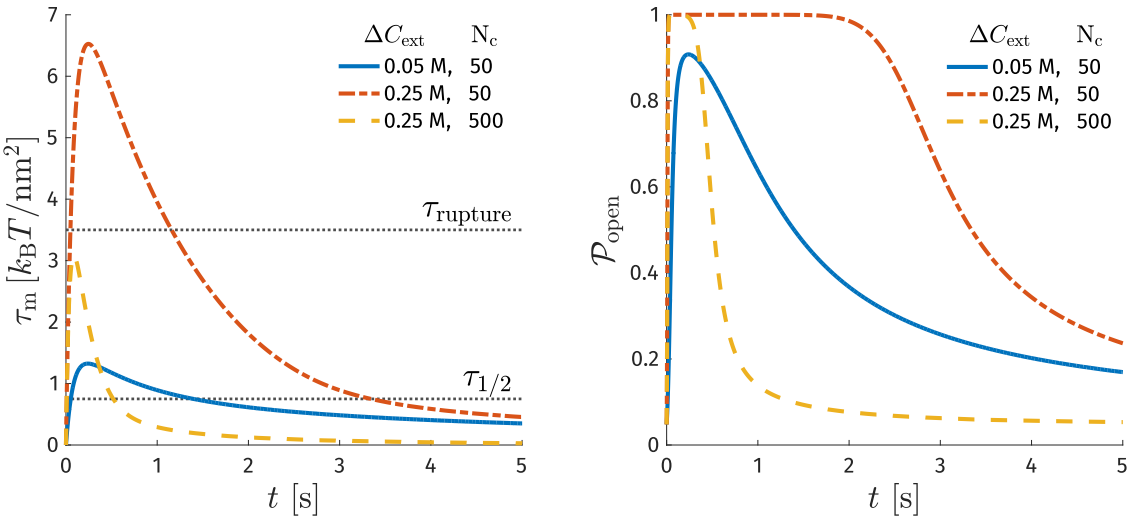

Figure 3.12: [Left] Membrane tension and opening probability for three different combinations of shock magnitude (ΔC_{ext}) and channel population (N_c).

the entire channel population gates almost immediately, and membrane tension increases to nearly $7.0\,k_\text{B}T/\text{nm}^2$. Not only does tension exceed the critical rupture value, it remains above this threshold for longer than one second. The model also predicts that YbdG channels are in a fully opened state for over two seconds, far longer than observed activation times for other channels such as MscS ($\approx 150\,\text{ms}$).

To model the over-expression of YbdG, the number of channels N_c is increased ten-fold from 50 to 500. By enhancing the cell's ability to discharge intracellular contents, the results show a significant reduction in both peak membrane tension and response time ($< 1\,\text{s}$). While YbdG alone osmoprotects against small fluctuations in external concentration that may not even constitute a "shock", over-expression or the presence of other channels is required to keep membrane stress below the lytic limit for standard experimental shocks.

Membrane tension exceeds lytic limit in double mutants

Failure of biomembranes such as those found in bacterial cells have traditionally been defined by a material constant known as the rupture strength. When membrane tension exceeds the rupture strength, lipids within the bilayer are ripped apart leading to the rapid formation of

a hole. While small defects can be repaired, large rupture events ultimately lead to cell lysis. For *E. coli*, the critical rupture tension is $\tau_{cr} = 3.5\,k_{\mathrm{B}}T/\mathrm{nm}^2$. Though this constant value is generally agreed upon, it has been shown that membrane rupture is in fact a kinetic process, and that rupture strength is inherently a dynamic property [37]. Taking these kinetics into account, the rupture strength depends on the loading rate and can be categorized into a fast and slow loading regimes. Up to a two-fold increase in rupture strength is seen under fast loading conditions (such as those featured during typical hypo-osmotic shocks), raising it to $3.5\,k_{\mathrm{B}}T/\mathrm{nm}^2 \lesssim \tau_{\mathrm{cr}} \lesssim 7.0\,k_{\mathrm{B}}T/\mathrm{nm}^2$.

We look to connect dynamic rupture strength to the model by first investigating the membrane loading rate during a shock. In all cell model strains, instantaneous 0.5M shocks result in fast loading rates on the order of hundreds of mN/m/s. These can be classified in the defect-limited (fast loading) regime defined by Evans et. al. [37], leading to increased rupture strength up to $2\tau_{cr}$. However, when the same shock is applied over 1 s to WT and double knockout ($\Delta mscL\,\Delta mscS$) cells, maximum loading rates reduce to 42 mN/m/s and 51 mN/m/s, respectively (units follow [37]). Further decreasing the shock rate to a "slow" $0.1\,\mathrm{s}^{-1}$ reduces loading rates to 5.7 mN/m/s and 5.9 mN/m/s for the same two mutants, such that they fall near the transition between slow and fast loading regimes. We can treat the constant $\tau_{cr} = 3.5 k_{\mathrm{B}}T/\mathrm{nm}^2$ as a lower bound for membrane failure, and $2\tau_{cr}$ as an upper limit for "fast" shocks.

Cells can survive spikes in tension to levels exceeding the static rupture strength, as long as the load is relieved quickly. Loading rate is primarily a function of volume influx through the membrane, thus it is weakly dependent on channels populations. The double knockout cell reaches a tension in excess of $10\,k_{\mathrm{B}}T/\mathrm{nm}^2$ under "fast" loading, while it is reduced to $\approx 6\,k_{\mathrm{B}}T/\mathrm{nm}^2$ when the shock rate is $0.1\,\mathrm{s}^{-1}$.

3.3 Discussion

E. coli cells utilize MS channels to mediate changes in pressure and volume induced by osmotic shock. In this work we have simulated the response of bacterial cells to osmotic

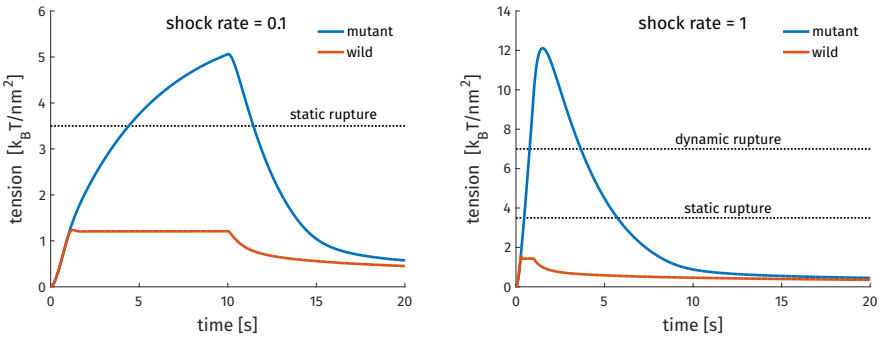

Figure 3.13: Membrane tension showing failure criteria for slow [left] and fast [right] shocks. Shock rates are 0.1 s^{-1} and 1.0 s^{-1} (left and right). Shock magnitude is 0.5 M.

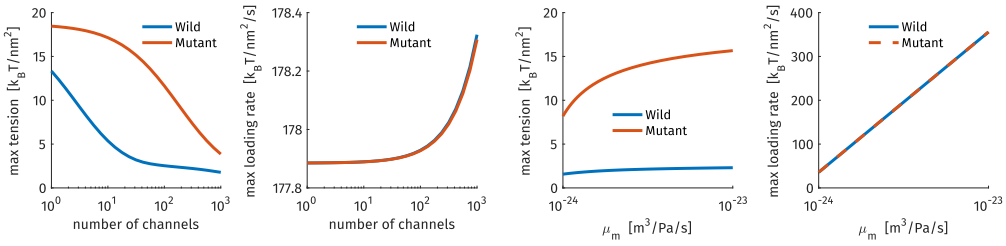

Figure 3.14: Peak values for membrane tension and loading rate versus number of channels (left) and membrane permeability μ_m (right). Peak tension values show weak and strong dependence on channel populations for wild type and mutant strains, respectively. Same behavior is seen for membrane permeability. Loading rate is effectively insensitive to channel populations, while it is linearly dependent on membrane permeability.

downshock by coupling transport equations with models of MS channels and cell envelope mechanics. Our results show that bacteria survive sudden down-shifts in external osmolarity by first absorbing water through the permeable inner membrane, and then discharging solute molecules through tension-activated channels. Water transport occurs primarily via the lipid membrane through pathways such as aquaporins, while solute efflux is dominated by MS channels. In cells with native level channel populations, we find that cells adapt to shocks on sub-second timescales, in agreement with previous research [34]. The cell wall and inner membrane sustain the internal pressure load, keeping volume expansion small and membrane tension below limits required for rupture. Together, these mechanisms protect bacterial cells from large, sudden changes in external osmolarity.

Mechanosensitive channels are viewed as pressure release valves designed to discharge intracellular contents and regulate osmotic pressure. Protein counts have shown that the two major channel types (MscL and MscS) are far more abundant than their smaller relatives [3], though channel distributions may exhibit high variability from cell-to-cell. We investigated how different MS channels contribute to osmo-protection by incorporating three channel types in our model, and varying their populations to simulate deletion and over-expression. MS channels act primarily as solute transporters, though they do assist in water efflux when hydrostatic pressure exceeds osmotic pressure. MS channels provide a negligible contribution to volume influx, as activation tensions are not attained for several tens of milliseconds after shock initiation, giving the cell adequate time to reduce osmotic pressure by absorbing water through the membrane. Channel water flux is largely insensitive to osmosis.

The MscL and MscS families are the foremost contributors to shock regulation due to their relative large pore sizes, transport capabilities, and overall abundance. MscL, viewed as the last line of defense against hypo-osmotic shock activates in small numbers when subjected to a 0.5 M downshock. This suggests that cells can withstand more extreme osmotic changes in their surrounding environment. Our model provides evidence of this, as membrane tension does not increase dramatically beyond the gating threshold of MscL when the shock magnitude is increased. Once MscL reaches its gating transition, pressure is rapidly reduced within tens of milliseconds preventing the cell from swelling further. MscL

may exist in large numbers to provide extended protection in hazardous environments, while MscS appears to be the main regulator of turgor pressure.

Standard shock assays have demonstrated that deletion of MscL, MscS, and MscK proteins in *E. coli* leads to lysis upon severe downshock [36]. Small channels such as YbdG can provide protection against small ($\lesssim 0.05\,\mathrm{M}$) osmotic challenge without the need for larger channels to gate. Furthermore, mini channel types aid in reducing cell volume after larger and more permeable channels have inactivated. These roles may be reason enough for the existence of mini channels. Furthermore, neglecting ion channel selectivity, we have shown that over-expression of YbdG provides adequate protection against moderate shocks by increasing the cell's capacity to efflux solutes, emulating previous experimental results [35].

In order to survive hypo-osmotic challenge, bacterial cells must relieve high intracellular pressure within a time period of roughly 1 s. Once gating tensions are reached, MS channels activate within milliseconds, beating cell swelling and protecting cells from structural failure. Evidence of the requirement to rapidly adjust to changes in external osmolarity lies within one specific death phenotype, typically described as "bursting," which occurs mere seconds after the shock begins. "Bursters" suffer catastrophic failure of the structures constituting the cell envelope. However, cell death can also occur over several minutes, inferred from decaying fluorescence levels during shock experiments. This suggests a slow leak of intracellular contents through nanometer scale perforations in the membrane. Mechanical failure of the lipid bilayer is quantified by its rupture strength, which we use to relate membrane tension to survival probability.

Membrane rupture is inherently a dynamic process and the critical value for failure depends on the loading rate [37]. Rupture strength is categorized into "slow" and "fast" loading regimes [37], and we find that moderate to large hypo-osmotic shocks fall into the latter group, resulting in up to a two-fold increase in lytic tension values. The loading rate is governed primarily by the membrane water permeability μ_m. Thus, the distribution of channels is largely insignificant unless MscL *and* MscS are not present. Our results demonstrate that *E. coli* cells containing full complements of either MscL or MscS respond

similarly to downshock, characterized by minimal volume strains and membrane tensions that remain below lytic thresholds. In contrast, we find that double mutants experience sustained tension above static and rate-dependent limits, suggesting that membrane failure is one of the mechanisms responsible for decreases in mutant cell viability observed in survival assays [35, 27]. Large volumetric strains ($\gtrsim 25\,\%$) accompany high tensions in double mutant cells, which may increase interstrand spacing in the peptidoglycan cell wall and lead to localized membrane protrusions called blebs. Under pressures of ~ 1 atm experienced by the model, these bulges may form if holes in the cell wall reach approximately 20 nm in diameter [38]. An understanding of cell wall failure is currently in its developmental stages, though we can infer from our model that when the structural load is shared between the cell wall and membrane, the stresses in each lamina are of the same order of magnitude. However, it is unclear how the two structural layers interact under normal turgor pressure, specifically if the membrane is pressed up against the wall. If a reservoir of excess membrane area exists, the brunt of the pressure load will then be carried by the cell wall. With pre-strain $\epsilon_0 \sim 5\,\%$, membrane tension experiences a dramatic decrease in wild-type cells while volumetric strains increase to levels in agreement with AFM predictions of approximately 12 % per atm [2].

It has been shown that cell survivability depends not only on the shock magnitude, but also the rate of medium osmolarity change [9]. We examined how the response of a cell is affected by a time-dependent ramp shock, finding that the response of double mutants is highly rate-sensitive, with significant changes in volume and membrane tension as the shock rate increases. These effects are far less pronounced in wild type cells (Fig. 3.5). Altering the rate of medium exchange influences the rate at which water enters the cell, consequently affecting membrane loading and the time needed to gate channels. During "moderate" to "fast" shocks, double knockout cells continue to inflate after all channels have gated, with membrane tensions exceeding lytic limits for sustained periods of 1 s or more. These prolonged stretches of high tension may lead to inactivation of certain channel types, further worsening the cell's ability to alleviate pressure. It may also be that tension in the membrane is spatially non-uniform, causing certain channels to remain inactive. Only "slow" shocks can be regulated by double mutants without surpassing critical limits for membrane failure,

implying that survival probabilities are both rate-dependent and strongly linked to stress in the cell envelope. We hypothesize that molecular-scale defects form within the membrane as its tension surpasses the lower bound for rupture. These small defects may leak intracellular contents across the cell envelope at a very slow rate, providing a possible explanation for long time-scale death. If the imposed shock causes the cell to continue expanding, small defects then evolve into larger holes increasing leakage rate, which may explain the variation in survival time after shock in cells that experience "rupture" type deaths. What remains clear is that mutant cells missing populations of the two dominant channel types (MscL and MscS) experience membrane tensions that not only exceed critical values for rupture, but do so for significant periods of time.

In conclusion, we use models of mechanics and transport to quantitatively describe the response of bacterial cells to hypo-osmotic shock. Although MscL channels are present in high numbers, only small fractions are required to protect against typical levels of shock used in experiments. On the other hand, smaller channels must be complemented by significant populations of MscS and/or MscL, otherwise membrane tension will exceed lytic limits.

CHAPTER 4

Finite Growth Mechanics

In this chapter we succinctly outline the theory of finite growth mechanics in biological tissues. We begin with a brief introduction that covers the current state of the field and its origins, followed by a discussion of the mathematical framework. Finally, we conclude the chapter with several simple numerical examples that illustrate how various growth related quantities evolve in time. In the final two examples we focus on the growth of the bacterial cell wall.

4.1 Introduction

Biological structures have the ability to respond to environmental stimuli by growing larger, smaller, or changing their density by modifying their microstructural makeup. They are a form of active matter. The terms growth, remodeling, and morphogenesis have all been used to describe growth-related processes in the mechanics community. Growth is defined by the addition of mass to a living structure that is accompanied by either a change in density or volume. Hard tissues such as bone grow primarily due to an increase in mass density. On the other hand, soft tissues including skin, tumors, cell walls, and hearts grow by maintaining near constant density while increasing their volume, which is sometimes referred to as swelling. Atrophy is defined as the opposite process of growth where mass resorption occurs and density or volume decreases. Remodeling of a biological tissue concerns changes in its microstructural composition such as reorientation of collagen fibers in growing skin, and the anisotropic growth of cardiac tissue in response to myocardial infarction. Morphogenesis is characterized as a change in a structure's shape or geometry, which typically involves

growth, remodeling, or both. In this thesis we focus primarily on volumetric growth of soft tissue at constant density, which we can reasonably assume is the case for an elongating bacterial cell wall.

4.2 Theory

The following section is devoted to introducing the theoretical foundations of finite growth mechanics discipline. We attempt to keep the discussion concise and only explain key topics related cell wall growth in detail. For a more thorough read, see [39, 40, 41, 42].

4.2.1 Kinematics

To describe the finite kinematics of bacterial cell wall growth, we begin by writing the deformation gradient as $\boldsymbol{F} = \nabla_{\boldsymbol{X}} \boldsymbol{\varphi}(\boldsymbol{X}, t)$, where $\boldsymbol{\varphi}(\boldsymbol{X}, t)$ maps positions $\boldsymbol{X}$ in the reference (material) configuration $\mathcal{B}_0$ onto positions $\boldsymbol{x}$ in the deformed (spatial) configuration $\mathcal{B}$ (Fig. 4.1). We then utilize the multiplicative decomposition of the deformation gradient $\boldsymbol{F} = \boldsymbol{F}^e \boldsymbol{F}^g$, where the tensors $\boldsymbol{F}^e$ and $\boldsymbol{F}^g$ describe reversible elastic and irreversible growth deformations, respectively. This approach was originally developed for finite crystal plasticity [43], before being applied to growth of soft elastic tissues [44]. Volume elements in the

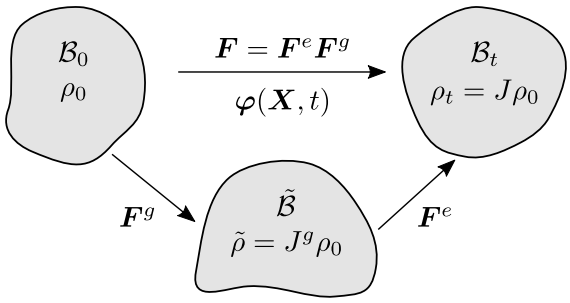

Figure 4.1: Multiplicative decomposition $\boldsymbol{F} = \nabla_{\boldsymbol{X}} \boldsymbol{\varphi} = \boldsymbol{F}^e \boldsymbol{F}^g$.

reference, growth (intermediate), and current configurations are defined as dV^0, dV^g, and dV, respectively. From this we can define the Jacobian associated with each deformation

gradient as follows

$$J = \det(\boldsymbol{F}) = J^e J^g \tag{4.1}$$

$$J^g = \det\left(\boldsymbol{F}^g\right) = \frac{dV^g}{dV^0} \tag{4.2}$$

$$J^e = \det\left(\boldsymbol{F}^e\right) = \frac{dV}{dV^g} = \frac{J}{J^g}. \tag{4.3}$$

In (4.1)–(4.3), the three scalar Jacobians define the total, growth, or elastic changes in volume of the body, which are all strictly greater than zero. Next we introduce two additional measures of deformation, the total right and left Cauchy-Green deformation tensors:

$$\boldsymbol{C} = \boldsymbol{F}^T\boldsymbol{F}, \quad \boldsymbol{b} = \boldsymbol{F}\boldsymbol{F}^T, \tag{4.4}$$

and their elastic counterparts are

$$\boldsymbol{C}^e = \boldsymbol{F}^{e^T}\boldsymbol{F}^e, \quad \boldsymbol{b}^e = \boldsymbol{F}^e\boldsymbol{F}^{e^T}. \tag{4.5}$$

Using the definitions of $\boldsymbol{C}$ and $\boldsymbol{C}^e$,the total and elastic Green-Lagrange strains tensors are given as

$$\boldsymbol{E} = \frac{1}{2}\left(\boldsymbol{C} - \boldsymbol{I}\right), \quad \boldsymbol{E}^e = \frac{1}{2}\left(\boldsymbol{C}^e - \boldsymbol{I}\right). \tag{4.6}$$

The spatial velocity gradient is defined as

$$\boldsymbol{\ell} = \nabla_{\boldsymbol{X}}\boldsymbol{v} = \dot{\boldsymbol{F}}\boldsymbol{F}^{-1}, \tag{4.7}$$

where the spatial velocity is $\boldsymbol{v} = \dot{\boldsymbol{\varphi}}$. Decomposing the spatial velocity gradient into elastic and growth parts

$$\boldsymbol{\ell} = \boldsymbol{\ell}^e + \boldsymbol{\ell}^g \tag{4.8}$$

leads to

$$\boldsymbol{\ell}^e = \dot{\boldsymbol{F}}^e\boldsymbol{F}^{e^{-1}}, \tag{4.9}$$

$$\boldsymbol{\ell}^g = \boldsymbol{F}^e\dot{\boldsymbol{F}}^g\boldsymbol{F}^{g^{-1}}\boldsymbol{F}^{e^{-1}}. \tag{4.10}$$

As we will see in the following, the growth velocity gradient $\boldsymbol{L}^g$ plays an important role in the evolution of $\boldsymbol{F}^g$ and is defined, along with the elastic velocity gradient $\boldsymbol{L}^e$, as follows:

$$\boldsymbol{L}^e = \boldsymbol{F}^{e^{-1}}\boldsymbol{\ell}^g\boldsymbol{F}^e = \dot{\boldsymbol{F}}^g\boldsymbol{F}^{g^{-1}}, \tag{4.11}$$

$$\boldsymbol{L}^e = \boldsymbol{F}^{e^{-1}}\boldsymbol{\ell}^e\boldsymbol{F}^e = \boldsymbol{F}^{e^{-1}}\dot{\boldsymbol{F}}^e. \tag{4.12}$$

4.3 Balance Equations

In classical continuum mechanics the reference configuration $\mathcal{B}_0$ has fixed volume and mass density ρ_0. This condition must be relaxed in the theory of growth, which allows for changes in density. Considering an open system with a rate of referential density change $\dot{\rho}_0$, mass flux $\boldsymbol{R}$, and mass source R_0, the balance of mass can be written as

$$\dot{\rho}_0 = \nabla_{\boldsymbol{X}} \cdot \boldsymbol{R} + R_0. \tag{4.13}$$

Following [45], the volume specific form of the balance of linear momentum can be written as

$$\dot{\rho}_0 \boldsymbol{v} + \rho_0 \dot{\boldsymbol{v}} = \nabla_{\boldsymbol{X}} \cdot \boldsymbol{P} + \rho_0 \boldsymbol{b}_0. \tag{4.14}$$

If we assume a quasi-static state and also make the assumption that the speed of growth is much smaller than $\boldsymbol{v}$, (4.14) simplifies to

$$\nabla_{\boldsymbol{X}} \cdot \boldsymbol{P} + \rho_0 \boldsymbol{b}_0 = \boldsymbol{0}, \tag{4.15}$$

where $\boldsymbol{P}$ is the first Piola-Kirchoff stress.

The Clausius-Duhem inequality ensures that dissipation remains non-negative. If we consider an additional entropy $\mathcal{S}$ and assume temperature remains constant, the dissipation inequality can be written as

$$\rho_0 \mathcal{D} = \frac{1}{2} \boldsymbol{S} : \dot{\boldsymbol{C}} - \rho_0 \psi - \theta^* \rho_0 \mathcal{S} \geq 0, \tag{4.16}$$

where θ^* is the temperature, $\boldsymbol{S}$ is the second Piola-Kirchoff stress, and ψ is an elastic strain energy.

In the reference configuration, the mass of an infinitesimal element is $dm_0 = \rho_0 dV_0$, while a grown mass element in $\mathcal{B}_g$ and $\mathcal{B}_t$ is $dm = \rho_g dV_g = \rho dV$. Considering a mass source per unit volume R_0 acting over time $[t_0, t]$, the grown mass element is the combination of the initial reference mass and that produced by R_0

$$dm = dm_0 + \int_{t_0}^{t} R_0 \, dt dV. \tag{4.17}$$

The grown mass in the intermediate and reference configurations are $\rho_g = \rho J_e$, and $\bar{\rho}_0 = J\rho_t = J_g\rho_g$, respectively.

It is assumed that material is inserted into a stress-free incompatible configuration $\tilde{\mathcal{B}}$, and that within this intermediate configuration mass density ρ_g remains constant during growth. The rate of change of the intermediate mass density is then $\dot{\rho}^g = \rho_0/\dot{J}^g + \dot{\rho}_0/J^g = 0$, which allows us to write the time evolution of the referential mass density as $R_0 = \dot{\rho}_0 = \rho_0 \mathrm{tr}\,(\boldsymbol{L}^g)$, where $\boldsymbol{L}^g$ is the growth velocity gradient.

4.4 Numerical examples

4.4.1 Example 1: Stress-dependent isotropic growth

The first example is used as a means of implementation validation. We consider an example found in [46], namely, the uniaxial deformation of a compressible Neo-Hookean solid undergoing stress-dependent growth. The strain energy function is given as

$$\psi = \frac{\lambda}{8} \ln^2 I_3^{\boldsymbol{C}^e} + \frac{\mu}{2} \left(I_1^{\boldsymbol{C}^e} - 3 - \ln I_3^{\boldsymbol{C}^e} \right), \tag{4.18}$$

where λ and μ are the Lame constants, $I_1^{\boldsymbol{C}^e} = \mathrm{tr}\,\boldsymbol{C}^e$, and $I_3^{\boldsymbol{C}^e} = \det \boldsymbol{C}^e$. Isotropic growth is considered in this case, with the growth deformation gradient taking the form

$$\boldsymbol{F}^g = \vartheta \boldsymbol{I}, \tag{4.19}$$

where ϑ is typically referred to as the growth multiplier or stretch ratio. The growth velocity gradient follows as

$$\boldsymbol{L}^g = \frac{\dot{\vartheta}}{\vartheta} \boldsymbol{I}. \tag{4.20}$$

In this example, the stress-driven evolution of ϑ depends linearly on the trace of the Mandel stress tensor $\boldsymbol{M}^e = \boldsymbol{S}^e \boldsymbol{C}^e$,

$$\dot{\vartheta} = k_\vartheta(\vartheta)\, \mathrm{tr}\, \boldsymbol{M}^e. \tag{4.21}$$

Table 4.1: Parameters used in numerical examples 1 and 2.

Parameter	Symbol	Example 1	Example 2
Elastic modulus	E	1.0 MPa	1.0 MPa
Poisson ratio	ν	0.3	0.3
Growth coefficient	k_ϑ^+	2.0	0.5
Resorption coefficient	k_ϑ^-	1.0	–
Growth limit	ϑ^+	1.1	$[1.10, 1.25, 1.50, 2.00]$
Resorption limit	ϑ^-	0.5	–
Growth exponent	m_ϑ^+	1.0	2.0
Resorption exponent	m_ϑ^-	4.0	–
Initial reference density	ρ_0^*	$1000\,\mathrm{kg/m^3}$	$1000\,\mathrm{kg/m^3}$

The growth coefficient k_ϑ was first defined by [40] and takes the form

$$k_\vartheta(\vartheta) = k_\vartheta^+ \left(\frac{\vartheta^+ - \vartheta}{\vartheta^+ - 1} \right)^{m_\vartheta^+} \quad \text{for } \operatorname{tr} \boldsymbol{M}^e > 0, \tag{4.22}$$

$$k_\vartheta(\vartheta) = k_\vartheta^- \left(\frac{\vartheta - \vartheta^-}{1 - \vartheta^-} \right)^{m_\vartheta^-} \quad \text{for } \operatorname{tr} \boldsymbol{M}^e < 0. \tag{4.23}$$

In (4.22) and (4.23), ϑ^+ and ϑ^- are the maximum and minimum limits of the stretch ratio ϑ, while k_ϑ^+, k_ϑ^-,m_ϑ^+, and m_ϑ^- are material parameters that influence the rate of growth (resorption) at a given stretch ratio. Values for the parameters can be found in Table 4.1. In this example a uniaxial stretch F_{11} is applied that varies below and above the growth limit ϑ^+ to showcase the response at specific levels of stretch (Fig. 4.2). The applied stretch smoothly varies between values every time increment $\Delta t = 80$. When the stretch is below the limit ϑ^+, growth occurs until biological equilibrium—a stress free configuration attained after growth has occurred—is eventually restored. If the stretch exceeds the growth limit then elastic deformation occurs to balance forces. The true density in the spatial frame evolves in time while the intermediate density remains constant.

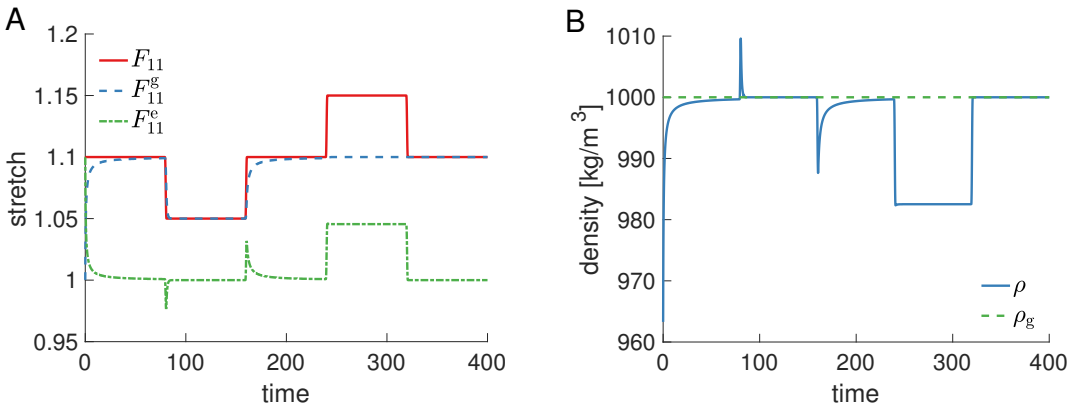

Figure 4.2: Evolution of stretch and density during growth of a body under uniaxial extension. A) The total applied stretch F_{11} (red) oscillates between 1.05 and 1.15, and the block responds to the applied deformation by growing, shrinking, or deforming elastically. Except for the time period $240 < t < 320$, the growth stretch $F^{g}_{11} = \vartheta$ (blue) quickly attains a value approaching that of the applied stretch. When $F_{11} = 1.15$ the growth limit $\vartheta^{+} = 1.1$ is exceeded and elastic deformation occurs (green). B) Evolution of the spatial ρ (blue) and intermediate ρ_g (green) configuration densities. The actual density changes abruptly when the total stretch is modified. If the growth limit is not exceeded, the spatial density returns to its initial value. When elastic deformation occurs, the current density decreases. Density in the intermediate or growth configuration ρ_g remains constant.

4.4.2 Example 2: Stretch-driven isotropic growth

Next we investigate the stretch-driven growth of a block under triaxial deformation. We again consider a block of Neo-Hookean material defined by the strain energy given in (4.18) undergoing isotropic growth, $\boldsymbol{F}^g = \vartheta \boldsymbol{I}$. A simple stretch-driven evolution of ϑ will depend linearly on the trace of the right Cauchy-Green elastic deformation tensor,

$$\dot{\vartheta} = k_\vartheta(\vartheta)(I_1^{\boldsymbol{C}^e} - 3), \tag{4.24}$$

where $I_1^{\boldsymbol{C}^e} = \operatorname{tr} \boldsymbol{C}^e$, and $I_1^{\boldsymbol{C}^e} = 3$ in the stress-free reference configuration. The growth coefficient k_ϑ takes a similar form to (4.22) and (4.23) except that it is written in terms of $\boldsymbol{C}^e$,

$$k_\vartheta(\vartheta) = k_\vartheta^+ \left(\frac{\vartheta^+ - \vartheta}{\vartheta^+ - 1} \right)^{m_\vartheta^+} \quad \text{for } \operatorname{tr} \boldsymbol{C}^e > 3, \tag{4.25}$$

$$k_\vartheta(\vartheta) = k_\vartheta^- \left(\frac{\vartheta - \vartheta^-}{1 - \vartheta^-} \right)^{m_\vartheta^-} \quad \text{for } \operatorname{tr} \boldsymbol{C}^e < 3. \tag{4.26}$$

For simplicity we consider a monotonically increasing applied triaxial stretch, and as a consequence resorption defined by (4.26) does not occur. We investigate the effect of growth limit parameter ϑ^+ by setting its value equal to 1.1, 1.25, 1.5, and 2.0. The applied stretch $F_{\text{app}} = F_{11} = F_{22} = F_{33}$ is modified every time increment of $\Delta t = 80$, and other parameters used in this example are given in Table 4.1.

Results for the stretches and densities are shown in Fig. 4.3. A stress-free biological equilibrium is only realized if the applied stretch does not eclipse ϑ^+. By $t > 160$, the growth limits $\vartheta^+ = 1.1$ and $\vartheta^+ = 1.25$ have both been exceeded, leading to sustained elastic deformation and a corresponding reduction in actual density of the compressible block. If the block was made of a incompressible material, the spatial density should remains constant under any combination of growth and elastic deformation. The evolution of the driving stretch displays the same characteristics as the elastic deformation gradient $\boldsymbol{F}^e$ (Fig. 4.4). For example, $I_1^{\boldsymbol{C}^e} - 3$ vanishes when the growth multiplier ϑ matches the prescribed deformation, consequently inhibiting further growth.

These elementary numerical examples illustrate how stress and stretch driven growth are modeled in the mechanics community. The implementation of these models can be performed

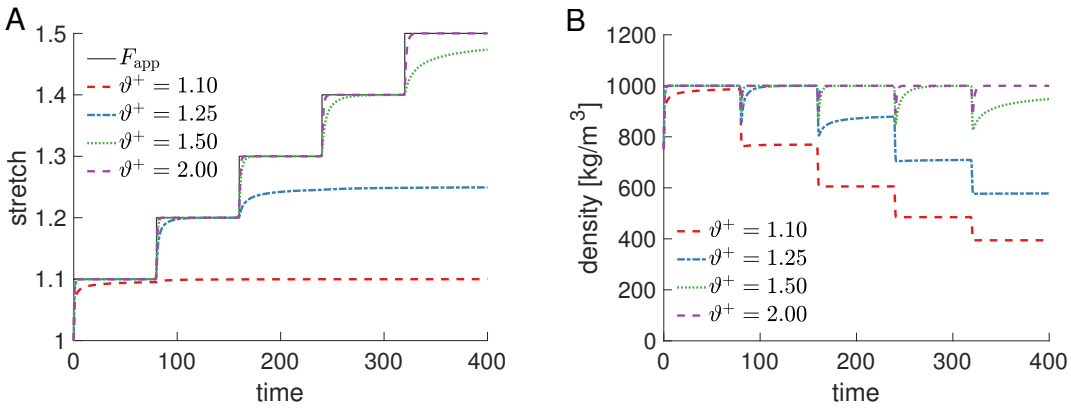

Figure 4.3: Evolution of stretch and density during isotropic growth of a block under triaxial extension. A) The total applied stretch F_{app} increases from 1.1 to 1.5 in increments of 0.1 over the time period of $t = 400$. As the block is stretched, sustained elastic deformation occurs in the cases $\vartheta^+ = 1.10$ and $\vartheta^+ = 1.25$ as their growth limits are surpassed. In the other two cases ($\vartheta^+ = 1.5$ and $\vartheta^+ = 2.0$) there is no sustained elastic deformation, however, biological equilibrium is attained much faster when the growth limit is higher due to the form of (4.25). B) The evolution of spatial densities is shown for various values of ϑ^+. Similar to the behavior shown in Fig. 4.2, the spatial frame density ρ returns to its initial value ρ_0^* if the growth limit is not exceeded.

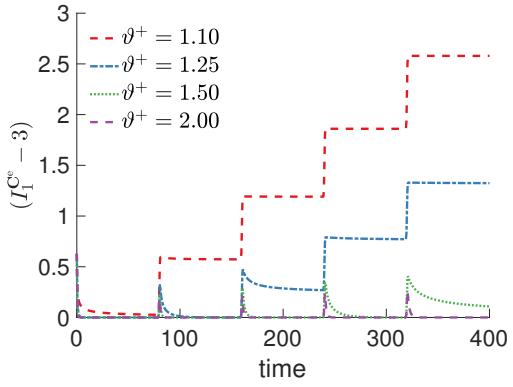

Figure 4.4: Evolution of the driving stretch in an isotropically growing block. The elastic driving stretch $I_1^{\boldsymbol{C}^e} - 3$ recovers to the initial rest reference configuration value of zero unless the total applied stretch exceeds the limiting growth value ϑ^+.

in commercial software such as COMSOL and ABAQUS, although writing custom code is necessary for advanced models.

4.4.3 Example 3: Transversely-isotropic cell wall growth

Next we consider transversely-isotropic growth of a rod-shaped cell under internal pressure. Biological tissues frequently grow in one or two directions defined aligned with their microstructural or fiber orientations. However, it is not a requirement that the (hyper-) elastic material model exhibits the same degree of anisotropy as the growth model. For simplicity we use the isotropic Saint-Venant Kirchhoff model in this example, which has a strain-energy density function of the form

$$\Psi = \frac{\lambda}{2} \operatorname{tr} (\boldsymbol{E}^e)^2 + \mu \boldsymbol{E}^e : \boldsymbol{E}^e, \tag{4.27}$$

where λ and μ are the linear elastic Lame constants. To capture growth in a single direction we can write $\boldsymbol{F}^g$ as

$$\boldsymbol{F}^g = \boldsymbol{I} - (\vartheta^g - 1)\, \boldsymbol{N} \otimes \boldsymbol{N}, \tag{4.28}$$

where $\boldsymbol{N}$ is a unit vector pointing in the direction of growth. Here we assume that $\boldsymbol{N}$ is aligned with the cylindrical axis of the cell, and that the spherical end-caps are inert and only undergo elastic deformation ($\det \boldsymbol{F}^g = 1$). Rather than being coupled with a mechanically dependent field (stress, strain), we assume that the growth rate depends on the current length of the cell $L(t)$ as has been observed in single cell experiments [47], and that the cylindrical section of the cell grows uniformly without any form of spatial-dependence. The change in length of the cell can be written as

$$\frac{dL}{dt} = \alpha L(t), \tag{4.29}$$

where α is a constant and the solution is of the form

$$L(t) = L_0 \exp(\alpha t), \tag{4.30}$$

where L_0 is the initial cylindrical length. By setting the doubling time to be $\tau_{\text{dbl}} = 20\,\text{min} = 1200\,\text{s}$, we obtain $\alpha = \log 2/\tau_{\text{dbl}}$. Substituting the growth multiplier ϑ^g for the cell length in

(4.29) then leads to

$$\dot{\vartheta} = \alpha\vartheta. \tag{4.31}$$

Table 4.2: Parameters used in numerical example 3.

Parameter	Symbol	Example 1
Elastic modulus	E	$50.0\,\mathrm{MPa}$
Poisson ratio	ν	0.3
Doubling time	τ_{dbl}	$20\,\mathrm{min}$
Growth coefficient	α	$3.466 \times 10^{-2}\,\mathrm{min}^{-1}$
Initial radius	R_0	$500\,\mathrm{nm}$
Initial length	L_0	$1.0\,\mu\mathrm{m}$
Thickness	h	$6\,\mathrm{nm}$
Pressure	p	$30\,\mathrm{kPa}$

We plot the normalized cell length and average stresses (Fig. 4.5) over the doubling period of twenty minutes using parameters from Table 4.2. The evolution of the cell length matches the exact solution from (4.30), and the average stresses remain roughly constant as the cell grows. The linear elastic solution for the stresses in a pressurized thin cylinder show that the hoop stress is twice the axial stress. Additionally, the axial stress of the cylinder is equal to the spherical pressure vessel stress of the same thickness and radius. In the geometrically nonlinear FEM solution the circumferential stress in the cylinder must decrease by roughly a factor of two as the spherical end-caps are approached. As the cell wall elongates, this transition zone decreases in size relative to the cell length, which explains the slight increase in circumferential stress $\sigma_{\theta\theta}$ over time. The cell wall is loaded with a relatively small turgor pressure $p = 30\,\mathrm{kPa}$ that results in only small volumetric swelling. As a consequence, the stresses remain close to those calculated using the linear elastic solution. Mises stress contours at four points in time are shown in Fig. 4.6. Any changes in the stress field away from the poles during growth are difficult if not impossible to perceive. At the

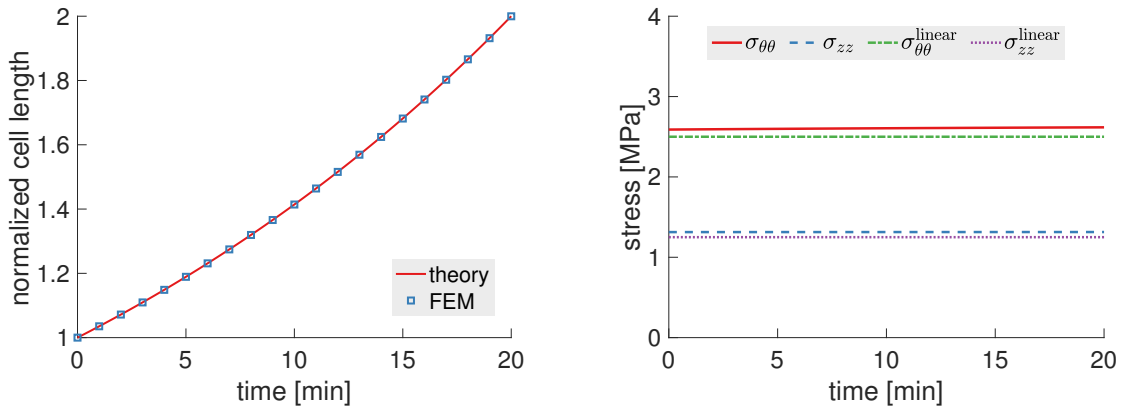

Figure 4.5: Length and stress evolution of a uniformly growing transversely-isotropic cell wall. Left: Normalized cell length for theoretical and finite element solutions. The two solutions are in agreement and the cylindrical section of the cell wall doubles in length over the time period of twenty minutes. Right: Average circumferential and axial stresses in the cylindrical section of the cell wall. The hoop and axial stresses (red and green) remain nearly constant during growth, exhibiting a very small increase as a result of the spherocylindrical geometry. The linear elastic solutions for cylindrical pressure vessels are displayed for reference $\left(\sigma_{\theta\theta}^{\text{linear}} = \frac{pR_0}{h},\ \sigma_{zz}^{\text{linear}} = \frac{pR_0}{2h}\right)$.

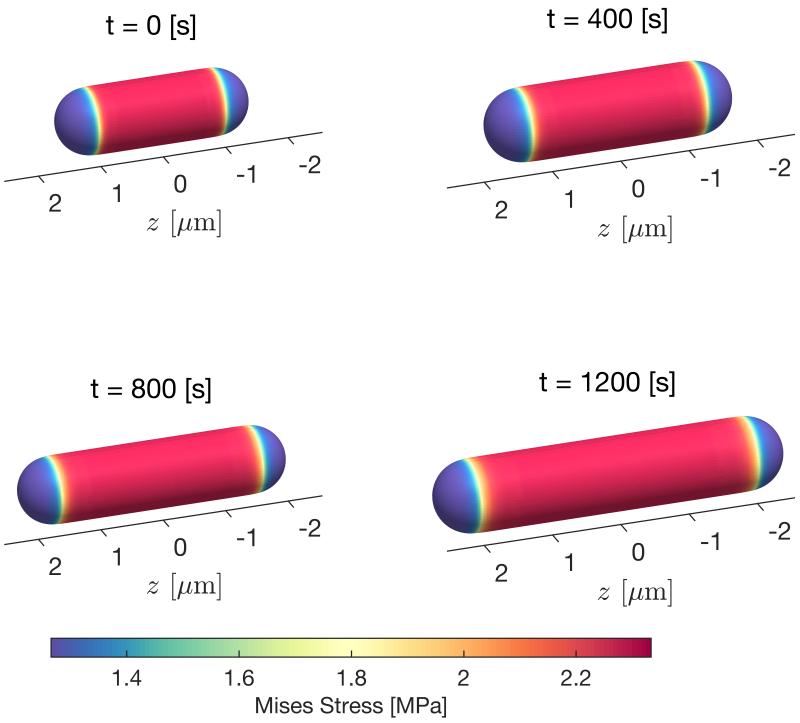

Figure 4.6: Mises stress contours displayed on the deformed shape of a uniformly growing cell wall. The stresses in the wall remain approximately constant as the cell extends to twice its initial length.

sphere-cylinder interface the transition zone becomes slightly larger. Only one-eighth of the spherocylinder was used in the FEM calculation along with symmetry boundary conditions, and since the growth is uniform the problem can be solved using an axisymmetric model.

4.4.4 Example 4: Spatially-dependent transversely-isotropic cell wall growth

The final example in this chapter is aimed at explaining a simplified version of the peptidoglycan strand extension model that is utilized in the full cell wall growth framework discussed in the following chapter. An *E. coli* cell grows axially by extending a pre-existing circumferentially aligned (on average) glycan strand or by inserting a brand new glycan chain into the peptidoglycan network. To define $\boldsymbol{F}^g$, we assume that these two processes are identical and can be idealized as the addition of a partial strip of circumferentially oriented material that only contributes to the axial component of the growth deformation gradient, F^g_{zZ}, which in turn, lengthens the cell. Furthermore, the incomplete strip should lead to the formation of a stress concentration at each of its two ends. Ideally, the growth-induced stress field should resemble that of an edge dislocation on an infinite thin cylinder with a Burger's vector oriented axially, as in [48, 49, 50].

To start, we introduce cylindrical coordinates in the reference (R, Θ, Z) and current (r, θ, z) configurations, respectively. The cell wall thickness is much smaller than the initial radius ($h \ll R_0$), thus we make the assumption that volume growth occurs uniformly through the thickness allowing F^g_{zZ} to be independent of the radial coordinate $r(R, t)$. To facilitate growth we need to track the positions of active MreB proteins as they traverse the cell wall. In the reference configuration we can express the position of an arbitrary growth site or motor as $\boldsymbol{X}_i^{\text{mtr}} = (\Theta_i^{\text{mtr}}, Z_i^{\text{mtr}})$, and similarly as $\boldsymbol{x}_i^{\text{mtr}} = (\theta_i^{\text{mtr}}, z_i^{\text{mtr}})$ in the current configuration. Without delving into the biological details that regulate the growth of the cell wall (see Ch. 6), we approximate the addition of volume by writing it as a flux through the thickness. This has the same effect as modeling a source embedded within the cell wall that adds mass that is constant in the thickness direction at the growth site locations.

Next we can write down a growth law that will add a small amount of material at the

position of an active motor $\boldsymbol{x}_i^{\text{mtr}}$. To emulate a dislocation without a singular core, we model the L_{zZ}^g as a two-dimensional Gaussian blob that is a function of $(\theta_i^{\text{mtr}}, z_i^{\text{mtr}})$,

$$\dot{\vartheta}^i = \vartheta_0 \exp\left[-\left(c_\theta(\theta-\theta^i)^2 + c_z(z-z^i)^2\right)\right], \tag{4.32}$$

where ϑ_0 is a constant representing the amount of material addition, and the parameters c_θ and c_z control the dimensions of the blob in the θ and z directions, respectively.

We are now ready to consider motion of an active motor and its effect on the growth law given in (4.32). For the sake of simplicity we can assume that the insertion machinery only moves in the θ direction, thus z^i remains constant. During a given increment in time, each active growth site either makes a *small* circumferential move and deposits material into the cell wall or it remains stationary without adding material. The discrete steps taken by the growth machinery lead to lack of accuracy in the simulations unless the time increment is very small. In full growth simulations that require tens of active motors and hundreds of inactive sites the stress field in the cell wall quickly becomes highly disordered, and as a result the error incurred by the discrete motion of the motors has a negligible effect on the solution. Additionally, if the turgor pressure is sufficiently large the corresponding stresses can be many orders of magnitude larger than the stresses induced by the defects, ultimately masking the error. In situations such as the insertion of a complete hoop of material into a mostly ordered cylindrical cell wall, small time increments are necessary.

It may be beneficial to write the growth law in a different form that allows for larger time steps. To implement this alternative method we draw upon the previous examples in this chapter. Instead of using (4.32) directly, we can write the motor's position assuming constant velocity as $\theta^i(t) = \theta_0^i + v_0 t$, where θ_0^i is the initial θ position of the motor and v_0 is a velocity. Then, integrating the expression with respect to time we obtain

$$\vartheta^i \sim \exp\left[A_0 \exp\left(-c_z(z-z^i)^2\right)\left(\operatorname{erf}\left[\sqrt{c_\theta}\left(\theta_B^i-\theta\right)\right] - \operatorname{erf}\left[\sqrt{c_\theta}\left(\theta_A^i-\theta\right)\right]\right)\right], \tag{4.33}$$

where A_0 is a constant and we have replaced θ^i and θ_0^i with θ_A^i and θ_B^i, which denote the circumferential coordinates of the two ends of the strip of new material. Rather than using (4.33) to directly prescribe $\boldsymbol{F}^g$, we can use the expression to define an upper limit on ϑ as

was performed in the previous examples. Rearranging (4.33) we can define upper growth limit at an arbitrary point considering contributions from all motors as

$$\vartheta^{\max} = \exp\left[\sum_i A_0 \exp\left(-c_z(z-z^i)^2\right)\left(\operatorname{erf}\left[\sqrt{c_\theta}\left(\theta_B^i-\theta\right)\right]-\operatorname{erf}\left[\sqrt{c_\theta}\left(\theta_A^i-\theta\right)\right]\right)\right]. \quad (4.34)$$

Finally, the evolution equation is

$$\dot{\vartheta} = \frac{1}{\tau_\vartheta}\langle \vartheta^{\max} - \vartheta \rangle, \quad (4.35)$$

where τ_ϑ is a time constant that regulates how quickly $\vartheta^{\max}$ is attained.

CHAPTER 5

Growth of the Bacterial Cell Wall

It is well known that rod-shaped bacterial cell walls—a thin shell made of a disordered peptidoglycan network—grow rapidly in length. This speed allows cells to divide several times per hour. However, fast growth requires the cell to rapidly add material to a highly pressurized (osmotically) shell without bursting. The basic mechanism for growth is actively driven dislocations plowing through the shell in the circumferential direction. These motor-driven defects introduce new material (MreB filaments) into the shell but generate stress concentrations surrounding the moving defects. Motivated by the large deformations inherent in bacterial growth, we develop a nonlinear continuum mechanics model with actively driven dislocations to describe the growth of the cell wall. Using numerical simulations, we study the interaction of stress fields that arise as these filaments are added to the existing peptidoglycan mesh. Furthermore, we investigate how the growth mechanics are affected by fluctuations in turgor pressure, and the presence of heterogeneities and defects in the cell wall that can form during an osmotic shock or antibiotic treatment.

5.1 Finite Growth

Rod-shaped bacterial cells rapidly grow and divide, while simultaneously maintaining their spherocylindrical geometry. The cell wall, constructed from a disordered network of peptidoglycan chains that form a porous barrier between the cytoplasmic contents of the cell and its surroundings, plays a prominent role in both growth and shape maintenance [51]. In gram-negative negative *E. coli* cells, the cell wall is at most a few layers of peptidoglycan in thickness, and is materially anisotropic, with relatively stiff glycan strands oriented around

the circumference of the cell that are cross-linked by flexible peptides [11]. This nanometer scale thin network resists the mechanical stress induced by osmotic pressure, which may be upwards of several atmospheres. For the cell wall to expand, it must incorporate newly synthesized material into its existing structure. However, the mechanisms responsible for coordinating this procedure are not fully understood. While the growth of other cellular organisms such as plant cells are driven by internal pressure alone, there are multiple mechanisms that govern bacterial growth. Furthermore, how cells remodel and repair defects in the cell wall is a remaining question. Recent experimental and theoretical works have highlighted the importance of the actin-like protein MreB in the growth of the cell wall, which guides the insertion of new material along tracks primarily oriented in the circumferential direction [52]. A more detailed understanding of the mechanics involved in cell wall remodeling and growth in the presence of defects could lead to novel methods for antibiotics to attack and break down the cell wall, aiding in the significant problem of antibiotic resistance.

The morphology of bacteria is remarkably robust. *E. coli* cells grow almost exclusively along their cylindrical axis, and exhibit little to no change in diameter. Interestingly, colonies of bacteria living in the same environment have vastly different lengths (depending on where they are in the division cycle), but nearly identical widths. This behavior is thought to be a result of curvature sensing MreB filaments that orient themselves primarily in the circumferential direction. MreB filaments (patches) travel in this preferred orientation around the periphery of the cell aided by biomolecular motors, and insert new cell wall material [53]. Rather than forming complete rings, MreB inserts material in strips that span a fraction of the cell circumference. The filaments can become dislodged from their tracks if they encounter another defect (static or active), and may then hop onto another track and continue the process, provided synthesized material is readily available.

In contrast with typical engineering materials with properties that remain constant, the peptidoglycan cell wall undergoes significant changes as it elongates. These permanent or irreversible modifications are initiated when covalent bonds holding the cell wall network together are broken to accommodate glycan strand extension or growth site nucleation. Furthermore, the two-fold change in length of an *E. coli* cell is far greater than the *small*

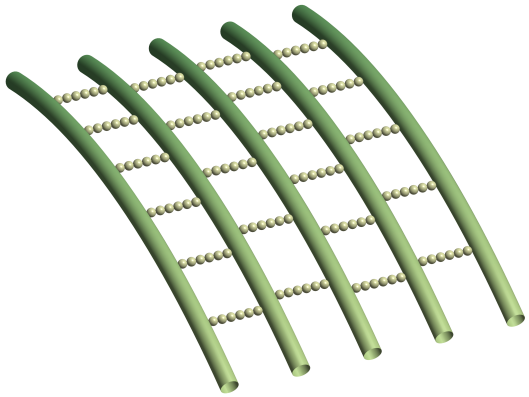

Figure 5.1: Depiction of the peptidoglycan network that makes up the cell wall. Stiff glycan strands (green) are linked together by relatively flexible peptides.

displacements required by linear elasticity theory. For these reasons, we utilize a nonlinear continuum mechanics framework coupled with finite growth kinematics to model cell wall elongation and morphogenesis. In the following we develop a nonlinear cell wall growth model, which encompasses the localization of active growth sites, finite processivity of the machinery that coordinates growth, and a mechanical description of the material insertion process. Further details of the kinematics and nonlinear mechanics are included in the SI.

Recent experiments have uncovered that *E. coli* cells bend when placed in confining environments, and robustly recover their characteristic rod-like geometry when they are removed [54]. Similarly, cells under external hydrodynamic drag forces grow in a curved manner, and straighten once the applied load is extinguished [55, 56]. For cells to exhibit shape recovery in these forms, active growth sites must preferentially localize in regions that induce straightening of the cell wall. While it remains unclear which mechanisms are responsible for this, two prevailing theories have emerged to address: (1) MreB and other molecules related to peptidoglycan strand extension localize to regions of negative Gaussian curvature [57, 58]; (2) Insertion of new material is dependent on mechanical stress, with regions of high tensile stress being favored. We adapt the latter theory herein, with both nucleation and strand extension depending on the local state of stress within the cell wall.

The membrane-bound protein MreB forms filaments (or patches) that are responsible for spatially coordinating the insertion of glycan strands into the cell wall. These filaments—driven by biomolecular motors—navigate around the circumference of the cell and insert material along the way, allowing the cell to maintain its rod-like shape. However, what determines the regions in the cell wall where these filaments localize remains in question. One possible theory is that MreB localizes in regions of negative Gaussian curvature, introducing new material in these locations that ultimately leads to cell straightening [59, 52, 57, 58]. This theory of geometry-based growth, however, cannot explain the experimental observations of filamentous *E. coli* exposed to hydrodynamic drag forces that cause cell to adopt curved geometries [55, 56]. From the results of these experiments, it is suggested that MreB establishes PG growth sites in regions of high areal strains [60]. Recent work has hypothesized that cell elongation is dependent on areal strain, with molecular mechanisms sensing changes in pore sizes residing in the cell wall [60]. It is proposed that the insertion of glycan strands is decomposed into strain-dependent and strain-independent parts, with the former working towards straightening the cell while the latter drives cell elongation. We take an approach that is complementary to the latter mechanically-based growth theory, and hypothesize that the stress concentrations that form at the tips of glycan strands as they are introduced in the PG network govern the locations of new growth.

5.1.1 Kinematics of Transversely Isotropic Growth

The kinematics of growth are described in Chapter 4. Here we focus on the cell wall which we assume only grows in the direction aligned with its cylindrical axis.

For the specific case of rod-shaped cell walls with transversely isotropic material properties, we define the structural vector $\boldsymbol{A}$ along the more flexible axial direction in the reference configuration. Assuming growth occurs exclusively in the direction of $\boldsymbol{A}$, the growth velocity gradient takes the form

$$\boldsymbol{L}^g = \frac{\dot{\rho}_0}{\rho_0} \boldsymbol{A} \otimes \boldsymbol{A}. \tag{5.1}$$

We are then able to update $\boldsymbol{F}^g$ in time using the relation $\dot{\boldsymbol{F}}^g = \boldsymbol{L}^g \boldsymbol{F}^g$, with $\boldsymbol{F}^g = \boldsymbol{I}$ at $t = 0$.

Evidently only one component of $\boldsymbol{F}^g$ varies in time, such that $\boldsymbol{F}^g$ can be written in terms of a growth multiplier ϑ^g,

$$\boldsymbol{F}^g = \boldsymbol{I} + (\vartheta^g - 1)\, \boldsymbol{A} \otimes \boldsymbol{A}. \tag{5.2}$$

Physically, the scalar ϑ^g can be interpreted as the stretch in the direction of $\boldsymbol{A}$ attributed to growth. It follows that

$$\boldsymbol{L}^g = \dot{\boldsymbol{F}}^{g-1}\boldsymbol{F}^g = \frac{\dot{\vartheta}^g}{\vartheta^g}\boldsymbol{A} \otimes \boldsymbol{A}, \tag{5.3}$$

and the scaling of $\boldsymbol{A}$ due to growth is $\boldsymbol{A}^g = \boldsymbol{F}^g\boldsymbol{A} = (\vartheta^g - 1)\boldsymbol{A}$.

5.1.2 Constitutive Equations

To describe the material anisotropy of the peptidoglycan cell wall, we consider a transversely isotropic St. Venant Kirchhoff constitutive model that can be expressed as the sum of isotropic and anisotropic free energies written in terms of invariants of the Green-Lagrange strain tensor $\boldsymbol{E}^e = \frac{1}{2}(\boldsymbol{C}^e - \boldsymbol{I})$,

$$\psi = \psi_{\text{iso}} + \psi_{\text{aniso}} \tag{5.4}$$

$$= \frac{\lambda}{2} I_1^E + \mu_T \left[\left(I_1^E\right)^2 - 2I_2^E \right] + \alpha I_1^E I_4^E + 2\left(\mu_L - \mu_T\right) I_5^E + \frac{\beta}{2}\left(I_4^E\right)^2. \tag{5.5}$$

This is simply the linear elastic free energy extended to the finite deformation regime, where $\boldsymbol{E}^e$ is substituted for the small strain tensor $\boldsymbol{\varepsilon}^e$, and the give independent material parameters (λ, μ_T, μ_L, α, β) can be written in terms of the transversely isotropic elastic moduli and Poisson's ratios (details in appendix). The anisotropic term is expressed as a function of the pseudo-invariants of $\boldsymbol{E}^e$ defined as

$$I_4^e = \boldsymbol{A} \cdot \boldsymbol{E}^e \boldsymbol{A}, \quad I_5^e = \boldsymbol{A} \cdot \left(\boldsymbol{E}^e\right)^2 \boldsymbol{A}, \tag{5.6}$$

where $\boldsymbol{A}$ is a vector oriented in the axial direction in the reference configuration. The elastic second Piola-Kirchhoff symmetric stress tensor in the intermediate configuration is defined as $\boldsymbol{S}^e = 2\frac{\partial \psi}{\partial \boldsymbol{C}^e}$. Through a pull back operation we can obtain the total second Piola-Kirchhoff stress in the reference configuration, $\boldsymbol{S} = \boldsymbol{F}^{g-1}\boldsymbol{S}^e\boldsymbol{F}^{g-T}$. Pushing forward to the current configuration provides the Cauchy or true stress $\boldsymbol{\sigma} = \frac{1}{J}\boldsymbol{F}\boldsymbol{S}\boldsymbol{F}^T$. Finally, the Mandel stress

in the intermediate configuration is $\boldsymbol{M}^e = \boldsymbol{S}^e\boldsymbol{C}^e$. This generally non-symmetric tensor is work-conjugate to the growth (or plastic) velocity gradient $\boldsymbol{L}^g$, and is a commonly used stress measure in plasticity and growth mechanics [41].

5.2 Evolution of Growth

To complete the set of growth equations presented above we need to describe the evolution of the growth multiplier ϑ^g via (5.3). As the cell wall thickness h is small relative to its radius R, we assume that growth is constant through the thickness. Therefore, the mass source can be written as $R_0 = j/h$, where j is a normal flux. The addition of new material is spatially heterogeneous, occurring exclusively at active growth sites in a process organized by filaments of the membrane-bound protein MreB. This actively driven growth process differs from that found in most biological materials. Powered by biomolecular motors, these filaments traverse the cell wall circumference at near constant velocity, extending circumferentially oriented glycan strands along the way. To model this growth process, we make a few simplifying assumptions. First, we assume that the motors travel in a plane perpendicular to the cylindrical axis in the reference configuration, such that upon completing a full revolution, a defect will encounter its other end. We also assume that when a filament is in motion it moves through an angle $\Delta\theta$ at each step. These simplifications are reasonable if the cell wall remains approximately cylindrical in shape as it grows. In an ad-hoc approach we write the contribution to $\dot{\vartheta}$ from a single active growth site ϑ^i with position $\mathbf{r}(\theta^i, z^i)$ in spatial cylinder coordinates as a two-dimensional Gaussian function

$$\dot{\vartheta}^i = \vartheta_0 \exp\left[-\left(c_\theta(\theta - \theta^i)^2 + c_z(z - z^i)^2\right)\right], \tag{5.7}$$

where ϑ_0 is a constant describing the rate of material addition, θ^i and z^i are the circumferential and axial positions of the moving growth site, and c_θ and c_z are constants related to the interstrand spacing of glycan chains and peptide links within the cell wall. In *E. coli* cells, several tens of active sites simultaneously move and add material to the cell wall. Summing

the contributions of N growth sites we obtain

$$\dot{\vartheta} = \sum_{i}^{N} \dot{\vartheta}^i = \vartheta_0 \sum_{i}^{N} \exp\left[-\left(c_\theta(\theta - \theta^i)^2 + c_z(z - z^i)^2\right)\right]. \tag{5.8}$$

5.2.1 MreB Dynamics

The positions of the MreB growth machinery are modeled as points embedded within the cylindrical section of the cell wall, and it is at these locations that material is inserted leading to growth (we neglect growth in the hemispherical endcaps). We hypothesize that the local axial stress is a significant driving mechanism behind cell wall growth. As a new strip of material is inserted into the existing wall, tensile stress concentrations arise at the ends of the strip, creating a stress field that resembles that of an edge dislocation. These regions of high tension then encourage the insertion of new material to prevent tearing or fracture. We can quantify this by writing a probability of insertion described by the Boltzmann factor $\exp(-\Delta G/k_{\mathrm{B}}T)$, where ΔG is the free energy of activation. Considering mechanical stress contributions to this energy barrier, we can rewrite the activation energy as

$$\Delta G = \Delta G_0 - S^e_{IJ}\Omega_{IJ}, \tag{5.9}$$

where ΔG_0 is the free energy at zero stress, S^e_{IJ} are the components of the elastic second Piola-Kirchoff stress tensor, and Ω_{IJ} are the components of the activation volume tensor, which is proportional to the amount of material inserted. Analogous to dislocation theory, the rate at which this energy barrier is overcome is $\sim \nu \exp(-\Delta G/k_{\mathrm{B}}T)$, where ν is an attempted insertion frequency. Using (5.9), we write the probability of an active dislocation inserting material and moving a step in a given time increment as

$$P = \exp\left(-\frac{\Delta G_0 - \boldsymbol{S} : \boldsymbol{\Omega}}{k_{\mathrm{B}}T}\right), \tag{5.10}$$

where we have absorbed the coefficient ν into P.

The stress based probability allows filaments to continue moving at roughly constant velocity until they encounter a region of low tensile stress (or compressive stress), or they reach their processive limit of a few hundred nanometers. The former situation is realized

when two active pieces of machinery moving in opposite directions collide, a motor runs into the back of another insertion strip or defect in the wall, or the head of a motor forms a complete loop and runs into its tail end. In all of the cases described above, the tensile stress concentration vanishes when two defects collide.

In Eq. (5.10) the values of ΔG_0 and Ω_{IJ} are unknown, but we can estimate them by assuming only the axial component of $\boldsymbol{S}$ contributes to Eq. (5.9), and by reducing $\boldsymbol{\Omega}$ to a scalar. Starting with the activation volume, we consider a small volume element of material with length proportional to the average glycan unit length $\ell \sim 1\,\mathrm{nm}$, width of the glycan interstrand spacing $w \sim 3\,\mathrm{nm}$, and height equal to the cell wall thickness $h \sim 5\,\mathrm{nm}$. Multiplying these three values, we obtain an estimated scalar activation volume $V_{ac} \approx 1\,\mathrm{to}\,5\,\mathrm{nm}^3$. For ΔG_0, we note that under standard turgor pressures the cell wall rapidly grows, indicating that this activation threshold must be low enough to allow for growth. If we express ΔG_0 as the product of a critical axial stress and the activation volume, and then substitute the axial stress of a cylindrical pressure vessel we obtain $\Delta G_0 \approx p_0 R/2hV_{ac}$, where p_0 is the turgor pressure. Finally, plugging in a turgor pressure on the lower end of estimates $p_0 = 0.3\,\mathrm{atm}$ leads to $\Delta G_0 \approx 10 k_\mathrm{B} T$.

5.2.2 Growth Site Activation and Inactivation

To express the elongation machinery dynamics of a growing bacterial cell wall, we follow a recent study that describes the growth mechanics using dislocation dynamics [48]. These dislocations are classified into active and inactive categories, with the former being both mobile and responsible for adding new material to the cell wall. The number of active and inactive growth sites are denoted by N_ac and N_in.

In the simple case of an elongating cylindrical cell with constant radius R, the rate of change in cell length L can be expressed in terms of the number of active growth sites

$$\frac{dL}{dt} = \frac{vw}{2\pi R} N_\mathrm{ac}, \tag{5.11}$$

where v is the average motor velocity and w is roughly the width of a single glycan chain, which we take to be the inter-strand spacing. By rewriting (5.11) in terms of an active motor

Table 5.1: Values of the parameters used in the growth simulations.

Parameter Name	Symbol	Value	Reference
Number of active MreB motors	N_{ac}	~ 30	[48]
Glycan interstrand spacing	λ_g	1 nm to 4 nm	[61]
MreB processivity	ℓ_{MreB}	$\sim$100 nm to 500 nm	[62]
MreB speed	v_m	5 to 25 nm/s	[63]
Elastic modulus (θ-direction)	E_θ	50 MPa	[1]
Elastic modulus (z-direction)	E_z	25 MPa	[1]
Cell wall thickness	h	5 nm	–
Cell radius	R	500 nm	–
Cell length (cylindrical region)	L	1 μm	–
Free energy at zero stress	ΔG_0	10 $k_{\mathrm{B}}T$	–
On-rate of growth sites (nucleation)	R_{on}	$1.3 \times 10^5\,\mathrm{s}^{-1}\mathrm{m}^{-1}$	–
Off-rate of growth sites (finite processivity)	R_{off}	~ 0.005 to $0.01\mathrm{s}^{-1}$	–
Inactive-to-active rate	R_{in}	$2.5 \times 10^{-4}\,\mathrm{s}^{-1}$	–

density $n_{\mathrm{ac}}(t) = N_{\mathrm{ac}}/L$ we obtain

$$\frac{dL}{dt} = \frac{vw}{2\pi R} n_{\mathrm{ac}} L. \tag{5.12}$$

Assuming the active motor density remains constant throughout growth, the steady-state lengthening of the cell is

$$L(t) = L_0 \exp\left(\frac{vw}{2\pi R} n_{\mathrm{ac}} t\right). \tag{5.13}$$

To supplement (5.11), we need to describe the rates of activation and inactivation of growth sites. We assume that sufficient nutrients are available to the cell in its surrounding environment, and that the density per unit length of both active and inactive sites remain approximately constant as the cell grows. The first process we consider is the insertion of a new strip of material into the cell wall, with one end activating while the other remains inactive. Each of these nucleation events is analogous to the creation of a dislocation pair, and it is assumed that they occur at a rate proportional to the cell length, with rate constant R_{on}.

Another pathway for material insertion is via the activation of inactive sites. In this process, biomolecular motors hop onto a vacant end of any partial glycan strand and continue its extension around the cell periphery. The rate of this activation process depends on the number of unoccupied sites N_{in}, and is denoted by R_{in}.

Finally, growth site activation is complemented by an inactivation process arising from the finite processivity of MreB that guides growth machinery. The extensional machinery falls off the tracks assembled by MreB once it reaches its limit of a few hundred nanometers, resulting in strips of new material that typically cover only a fraction of the circumference. Inactivation, with rate constant R_{off}, is proportional to the number of active growth sites.

From the nucleation, activation, and inactivation processes described above, the time evolution of active and inactive growth sites can be written as

$$\frac{dN_{\mathrm{ac}}}{dt} = R_{\mathrm{on}} L + R_{\mathrm{in}} N_{\mathrm{in}} - R_{\mathrm{off}} N_{\mathrm{ac}} \tag{5.14}$$

and

$$\frac{dN_{\mathrm{in}}}{dt} = R_{\mathrm{on}} L - R_{\mathrm{in}} N_{\mathrm{in}} + R_{\mathrm{off}} N_{\mathrm{ac}}. \tag{5.15}$$

Combining the above with (5.11) and substituting the densities $n_{\text{ac}} = N_{\text{ac}}/L$ and $n_{\text{in}} = N_{\text{in}}/L$, we obtain the following relationships for the steady-state densities

$$\frac{dn_{\text{ac}}}{dt} = 0 = R_{\text{on}} - R_{\text{off}} n_{\text{in}} - \frac{vw}{2\pi R} n_{\text{ac}}^2 + R_{\text{in}} n_{\text{in}}, \tag{5.16}$$

$$\frac{dn_{\text{in}}}{dt} = 0 = R_{\text{on}} - R_{\text{in}} n_{\text{in}} + n_{\text{ac}} \left(R_{\text{off}} - \frac{vw}{2\pi R} n_{\text{in}} \right). \tag{5.17}$$

We now have a set of equations for the growth site dynamics, where biological processes govern the on and off rates. However, it is plausible that the nucleation and activation processes are also spatially dependent, with new growth sites targeting regions of high stress that may include damage. Thus, for both the activation of an inactive site and a nucleation event, the probability in (5.10) governs the location of activation. In the simulations the rates of activation and inactivation are modeled as Poisson processes.

5.3 Results

5.3.1 Elongation Rate of the Cell

The model reproduces the exponential growth rate observed experimentally with a doubling time of 20 minutes, assuming the activation threshold governed by ΔG_0 is set low enough to allow growth sites to freely move around the cell wall at constant velocity (Fig. 5.2). Further decreasing ΔG_0 has no effect on the model since each defect is limited to either move a constant distance or remain stationary in a given time step. When ΔG_0 is set high enough to prevent continuous motion of MreB filaments, the activation volume V_{ac} acts as a sensitivity parameter determining how rapidly the probability falls off. It appears likely that defects are able to overcome this energy barrier relatively easily based on experiments showing that the average speed of MreB remains largely unaffected by moderate osmotic shocks, and recovers rapidly after more extreme variations in pressure. It may be that by regulating turgor pressure the cell can maintain a high growth rate, a rate that only decreases when the pressure drops to levels that approaching those associated with plasmolysis.

During a typical growth cycle of 20 minutes, the average axial and circumferential stresses remain nearly constant (Fig. 5.4). However, the maximum stresses show a rapid increase

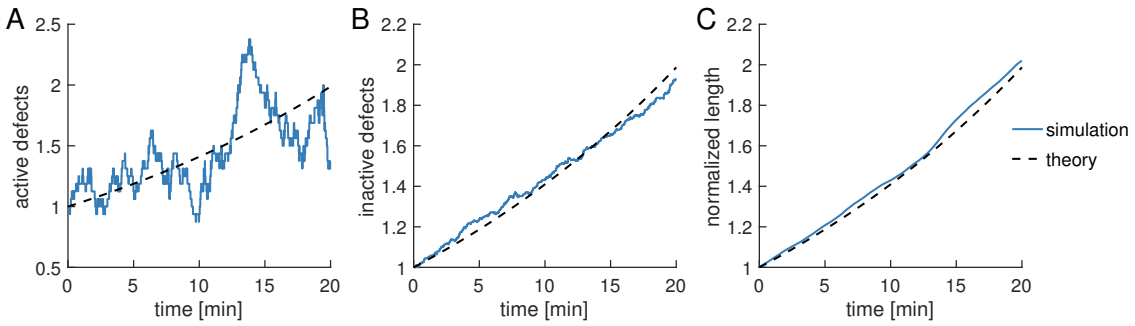

Figure 5.2: Evolution of normalized defect concentrations and cell length over a time period of 20 minutes. The threshold ΔG_0 is set very low, such that the motors move continuously. The blue lines show the results from a single representative simulation, and the black dashed line shows the theoretical value obtained by solving the set of equations above. Parameters are chosen that lead to the cell length doubling in approximately 20 minutes. A) Normalized number of active defects. Large fluctuations are observed in the active growth site concentration, though this behavior does not carry over to the cell lengthening rate. B) The normalized number of inactive defects increases more steadily than the active defect concentration, which is a consequence of $N_{in} \gg N_{ac}$. C) The cell length steadily increases to roughly twice its initial value after 20 minutes, with a slight kink between 10 and 15 minutes corresponding to the rapid drop and subsequent spike in active defects. The cell length is calculated as the average difference between the two surfaces on the ends of the cylinder.

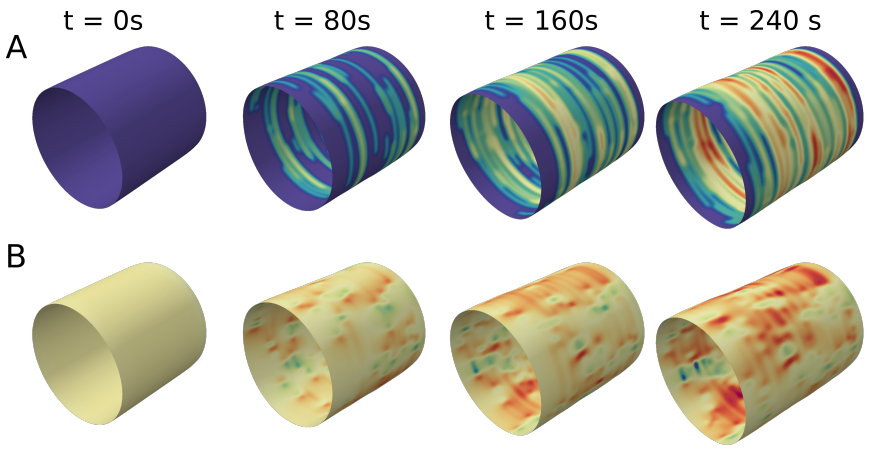

Figure 5.3: Evolution of growth multiplier ϑ (top) and axial stress σ_{33} (bottom). Top: Stochastic insertion of new material leads to an increasingly nonuniform cell wall as it elongates. Bottom: Starting from a stress free initial state, the peak stress values increase as the motion of active growth sites results in the formation of stress concentrations around the cell. Once the cell wall has reached a significantly disordered state, the increase in stress slows drastically allowing the cell to continue to elongate.

over the first few minutes accompanied by large fluctuations. The increase in peak stress values stems from the initial state being defect free, while the rapid fluctuations result from the interaction of defects as the move past one another. As the cell continues to grow the maximum stresses appear to approach a plateau, remaining within a small region.

5.3.2 Comparison with Linear Elastic Theory

To explore the effects of the nonlinear growth model we evaluate the axial and hoop Cauchy stress distributions over the cylindrical section of the cell (Fig. 5.5). The stresses are computed at the element quadrature points at a few time increments over the growth cycle of the cell. In the case of the compressible isotropic St. Venant Kirchhoff material model, the stresses generally increase with growth at a slow rate and their distributions widen. While the latter behavior is reproduced by the linear elastic theory, the rise in average stress values–corresponding to a shift in the distribution to the right–is a characteristic of the nonlinear model. This relatively slow increase in stress is a product of non-uniform or differential

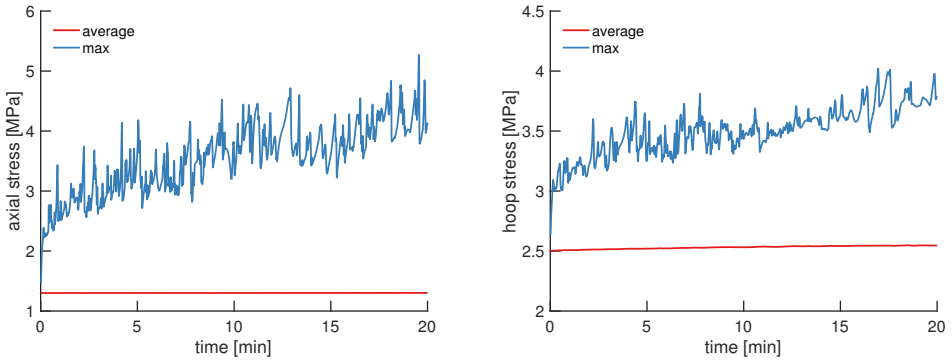

Figure 5.4: Evolution of axial and circumferential Cauchy stress (σ_{zz} and $\sigma_{\theta\theta}$). The average stress over the cell domain remains approximately constant during growth, while peak stress values generally increase with large transient fluctuations. As more material is added to the cell wall the disorder in the stress field increases, resulting in higher stresses. Interestingly, peak values of the axial and hoop stress are comparable in magnitude. On average, the hoop stress is a factor of two larger than the axial stress as expected.

growth, where the addition of a partial band of material produces a pair of stress concentrations, located at either end of the strip. While additional growth in the surrounding region can alleviate these stress concentrations, the stochastic nature of the model coupled with the fixed size of each piece of inserted material renders this unlikely. As a consequence the cell wall remains in a state of disorder characterized by an inhomogeneous stress field, augmenting the typical residual stresses associated with finite growth mechanics. Geometric nonlinearities are responsible for the initial shift of the distributions to the right prior to the onset of growth but after the cell has been loaded by an internal pressure. In Fig. 5.6 the axial and circumferential stress distributions are shown for an *incompressible* transversely isotropic St. Venant Kirchhoff material ($J^e = 1$). The response is markedly different from that of the compressible model, with drastic increases in stress and the formation of multiple peaks in the distributions. Defect interactions play a stronger role when incompressibility is enforced at the material level.

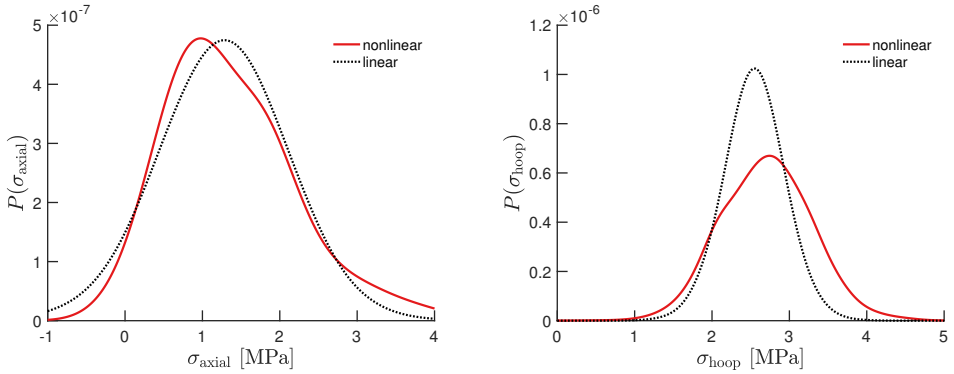

Figure 5.5: Axial (left) and hoop (right) stress distributions for an isotropic cell with 500 inactive defects. The midpoints of the nonlinear distributions are shifted slightly to the right as a consequence of large displacement theory. Furthermore, the tail at the higher end of the axial distributions increases in size with the number of defects.

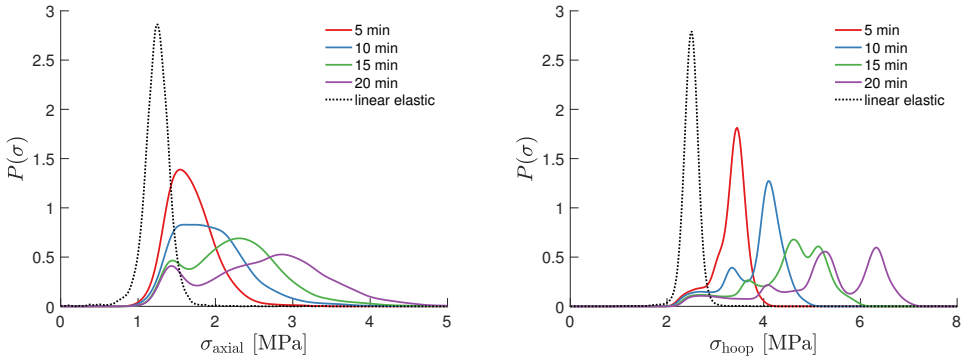

Figure 5.6: Axial (left) and hoop (right) stress distributions using a transversely isotropic incompressible material model.

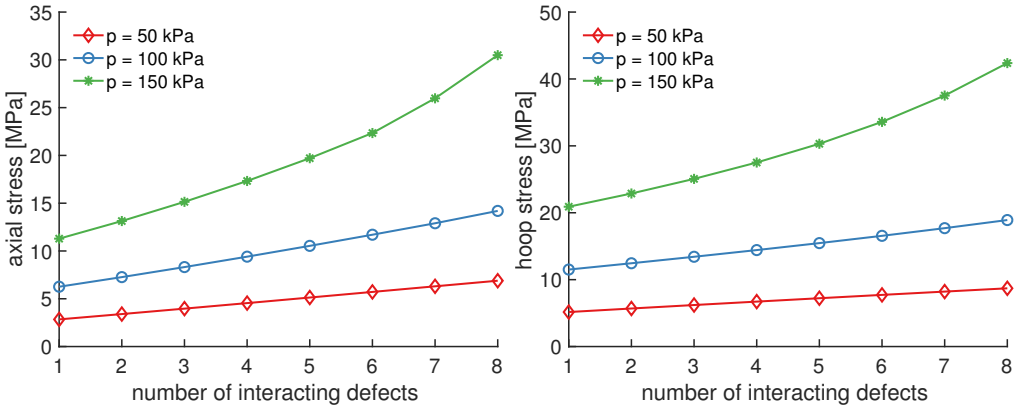

Figure 5.7: Effects of defect interactions and internal pressure on the axial (left) and circumferential (right) Cauchy stress (σ_{zz} and $\sigma_{\theta\theta}$). At low pressure the stresses appear directly proportional to the number of interactions, while the relationship becomes nonlinear at higher pressure.

5.3.3 Parametric Analysis

In the parametric study that follows we analyze a cell with a strip of new material that has nearly completed a full revolution. As a result of the small gap between the ends of the strip, a region of relatively large tensile stresses forms. Additional layers of material are then repeatedly added on top of the incomplete strip and the axial and hoop stresses are calculated while varying the pressure, wall thickness, and defect geometry. Herein we present and discuss the nonlinear effects of pressure on the stresses and include the remainder of the parametric studies in the Appendix.

Typical turgor pressures in *E. coli* cells range between approximately 0.3 atm and 3 atm. Towards the low end of this pressure range the maximum axial and hoop stresses increase almost linearly with the number of interacting defects (Fig. 5.7). However, at higher pressures the relationship is clearly nonlinear, as the peak stresses begin to increase rapidly with only a small number of interactions.

5.4 Discussion

In this work we developed a mechanical growth model with finite kinematics to study a growing rod-shaped bacterium. In addition to the nonlinear mechanics model, we set up a system of differential equations to regulate the positions of the MreB growth machinery and control their state (active/inactive). Furthermore, the motion and activation of the PG insertion machinery are governed by a stress dependent probability, with regions of high tensile stress encouraging greater motion of active defects and activation of inactive defect. By selecting reasonable parameters, using the steady-state solutions of the rate equations as initial conditions and setting a low barrier to motion, the model readily reproduces exponential growth as expected.

As seen in Fig. 5.4, the stresses on average remain roughly constant as the cell grows. Therefore, the probability that an arbitrary active growth site will make a move during a given time step stays at nearly the same value as the cell elongates. The situation is different though in the case of hyperelastic or incompressible materials. For these materials the average stresses do in fact increase significantly, leading to a situation where growth promotes faster growth. This is another example of the St. Venant Kirchoff material producing a different result than other materials models. While biological materials are typically not modeled well by the SVK material, the current mechanical understanding of the PG network makes it difficult to justify the use of a more complicated hyperelastic model.

By analyzing how the cell wall stresses evolve throughout the growth cycle we demonstrated the important nonlinear effects that are recovered by the finite deformation model, and showed how modulating various parameters including the density of active and inactive growth sites, turgor pressure, and mechanical properties influences growth. Perhaps most intriguing is the significant rise in stress as defect density increases for a turgor pressure $p = 150\,\mathrm{kPa}$, as shown in Fig. 5.7. This is a relatively low density, thus, it may be a reasonable assumption that normal turgor pressures are $\lesssim 1$ atm or lower, in agreement with recent consensus.

It is clear that the large deformations inherent in bacterial growth necessitate the use of

finite kinematics to accurately capture the mechanical behavior of the cell wall. In future studies, consideration of a more intricate hyperelastic material model may provide insight into the predicted stress-stiffening behavior of the cell wall. Alternatively, incorporating a continuum damage mechanics model into the existing framework may provide an additional way to investigate cell lysis caused by a defective cell wall. Finally, the inner and outer membranes support isotropic tensions and likely grow isotropically as well. A differential growth model may lead to a better understanding of the stress-states of the inner and outer membranes under normal growth conditions, and provides clues as to how the membrane bound protein MreB can aid in growing the cell wall while being attached to an adjacent layer.

CHAPTER 6

Conclusions and Future Directions

6.1 Conclusion

In this thesis, three different directions were taken to investigate the mechanics of bacteria. First, a thin shell model was developed to gain insight into the material properties of peptidoglycan cell wall. The mechanical contributions of the lipid inner membrane were incorporated into this model, which has not previously been considered. The inner membrane is capable of sustaining a state of isotropic tension, which provides a signal to membrane dwelling mechanosensitive channels to regulate turgor pressure. Two separate approaches were taken to build a mechanical model for the bacterial cell envelope. An analytical composite shell model was constructed using linear elastic pressure vessel mechanics, and bounds on the mechanical properties of the cell wall were determined through the use of material stability requirements and experimentally observed strains. It was found that rod-shaped bacteria such as *E. coli* have highly anisotropic cell walls, with a circumferential elastic modulus that is at least four-fold greater than the axial direction stiffness. Furthermore, the inner membrane was determined to bear a substantial portion of the turgor pressure load that can be on the same order of magnitude as the cell wall. By providing significant structural support, the inner membrane encourages even greater levels of cell wall anisotropy in order for the bacterium to maintain its spherocylindrical geometry. Additionally, key relationships between pressure, volume, and membrane tension were derived. To validate the analytical work, an axissymmetric thin shell finite element model accounting for geometric nonlinearity was implemented. The computational model considers stretching and bending of both lamina, and the mechanical behavior under internal pressure loading generally agrees

with those calculated by the analytical model, indicating that bending effects are negligible. The composite shell model brings new insights into the mechanical properties of the cell wall that have proven difficult to ascertain experimentally, and acts as stepping stone into the study of cellular transport.

Next the remarkable ability of bacteria withstand large, sudden changes in external osmolarity known as osmotic shock was investigated using the previously discussed mechanical model and the Kedem-Katchalsky transport framework. Specifically, simulations of osmotic downshock are carried out by rapidly decreasing the external solution concentration and then monitoring the evolution of various quantities until equilibrium is restored. The mechanics are coupled to the transport dynamics via the pressure-volume relationship derived for the composite shell model. Furthermore, three non-specific types of mechanosensitive channels of varying sizes with tension dependent gating are integrated into the model, allowing for the release of intracellular solute and augmenting the water transport of the semipermeable inner membrane. Following osmotic shock experiments, a variety of shock magnitudes and rates are numerically simulated. The model cell's response to a linearly varying shock is drastically different than the response to instantaneous downshock, with the cell exhibiting the ability to withstand the change in environmental conditions by opening only the number of channels required to effectively match the shock rate. The peak value of membrane tension and the rate at which it is loaded largely determine cell survivability on short time scales, and the model predicts an increase in survivability as the shock rate decreases, providing quantitative evidence for experimental observations. A detailed analysis of the permeability parameters and the effect of channel populations on survival is carried out, and it is determined that only a handful of large channels are necessary to withstand all but the largest of osmotic shocks, aligning with experimental work. Overall, the model provides evidence that cell lysis on short time scales induced by osmotic is governed by transport dynamics, with failure of the inner membrane being a likely cause. Although geometry and anisotropic constitutive laws qualitatively affect the shape of the cell during swelling, they do not greatly affect the likelihood of survival on short time scales. However, cell lysis on the time scales of growth cannot be fully explained by transport alone, which leads into the final study on

cell wall growth.

To further understand how lysis occurs tens of minutes following an osmotic shock, we implement a nonlinear finite growth model of the cell wall to determine if defects in the peptidoglycan network can result in the cell growing itself to death. While most mechanical growth laws for biological tissues are uniform throughout the material, a spatially-dependent growth constitutive equation is constructed to accurately capture the strip-like insertion and extension of circumferentially aligned glycan strands. Furthermore, the motion of active growth sites regulated by the protein MreB is governed by a stress-dependent probability, as are the dynamics that control where the activation of new growth sites occurs, and which previously inactive sites receive growth machinery and become active. Starting from a stress-free reference configuration with spherocylindrical geometry, the non-uniform addition of peptidoglycan into the cell wall leads to an increasingly disordered cell wall and a corresponding increase in stress. The model cell wall typically grows relatively straight while stresses in the cell wall can exhibit transient spikes when the stress fields generated by growing strips interact with one another. Further analysis of the stresses and their dependence on the density of defects shows that on long time scales a damaged cell can worsen its situation by adding material in disadvantageous positions. It is also clear that a nonlinear model is necessary to capture the large displacements that accompany finite growth and the large strains that form adjacent to freshly inserted strips. Finally, it is shown that hyperelastic and incompressible materials, which are common in biology, show increasingly nonlinear behavior when defects interact.

6.2 Future Work

Currently, one of the biggest questions in bacterial mechanics is: What is the driving force behind cell wall growth? Many studies have given conflicting results and two main theories have endured. Curvature-driven growth is one of these theories, which stems from experiments that provide evidence of MreB proteins localizing to regions of negative Gaussian curvature. This geometry based theory is supported by its ability to maintain cell shape,

and keep growth away from the poles. However, experiments that induce cell wall bending appear to show the opposite behavior. As the bending forces are removed, curvature driven growth should lead to a snap-back type response, but this does not occur. Both of these theories can be investigated computationally using shell finite elements, which will reduce the computational cost and allow for a simple calculation of the curvature. A straightforward test would be to initialize the cell in the reference configuration with an irregular geometry and simulate its response. Experiments have shown that cells grow back into their normal rod-shaped geometry after being placed in confining environments.

Another question that is still not fully understood is: Why is there such a variety in mechanosensitive channels and what is the reason for their large populations? Recent work on this topic including the work in this thesis lacks a full explanation to this question. The general consensus is that the extra channels provide additional protection in case environmental conditions worsen. Surprisingly, recent protein counts have indicated that channel numbers may be an order of magnitude higher than previously thought. If this is so, it indicates that the channel flow models are drastically overestimating the amount of solute and water that can flow through them. Furthermore, the inner membrane may be better modeled by a set of aquaporin channels rather than a continuous semi-permeable layer.

Finally, a very important topic that can be addressed by the mechanics community is that of antibiotic resistance. As a large class of antibiotics act by attacking the cell wall, coupling a continuum damage model with finite growth mechanics may lead to a further understanding of how damage progresses and evolves in a cell, and what type of initial defects are required to lead to specific death phenotypes. A microstructural model may also be of benefit here, where the glycan chains and peptides can be modeled individually as rods with bending and stretching stiffness. Binding and unbinding rules can easily be implemented in a rod-based model, which can then be used to study how damaged can sometimes repair themselves, or to simulate antibiotic induced lysis via insertion of defective material that is coupled with model for its evolution.

APPENDIX A

Axisymmetric Composite Finite Element Model

A displacement based finite element analysis is utilized in this work to validate the cylindrical composite shell model derived in Section 2.1. Kirchhoff shell theory is applied and axisymmetric elements are used to construct a laminate model that fully accounts for the nonlinearities intrinsic to the spherocylindrical geometry of a bacterial cell. Deformation of both layers is coupled, such that only one set of nodes and elements is necessary to describe equilibrium configurations under internal pressure loads. The shell surface geometry and kinematics are briefly outlined before details of the energy models are discussed. A variational approach is taken in deriving the governing equations, leading to a weak form minimization problem that is approximated using the finite element method [64].

A.1 Geometry and Kinematics

The spherocylindrical shell geometry can be described using axisymmetry by first noting the revolution symmetry about the longitudinal z-axis. Reflection symmetry about the $z = 0$ plane leads to the simple curved geometry shown in Fig. A.1. As the displacement analysis of the shell is performed exclusively along the meridional line, 1-D finite elements are used to approximate the deformed shape.

The reference surface Ω is parametrized by introducing two curvilinear coordinates $\{s^1, s^2\}$ that tangentially follow the shell surface. Current positions on the deformed surface ω are given by vector $\boldsymbol{x} \in \mathbb{R}^3$, defined by the mapping $\boldsymbol{x} = \boldsymbol{x}(s^1, s^2)$, with tangent basis vectors

$$\boldsymbol{a}_\alpha = \frac{\partial \boldsymbol{x}}{\partial \theta^\alpha} \equiv \boldsymbol{x}_{,\alpha}. \tag{A.1}$$

Note that the standard summation convention applies here with Greek indices indicating

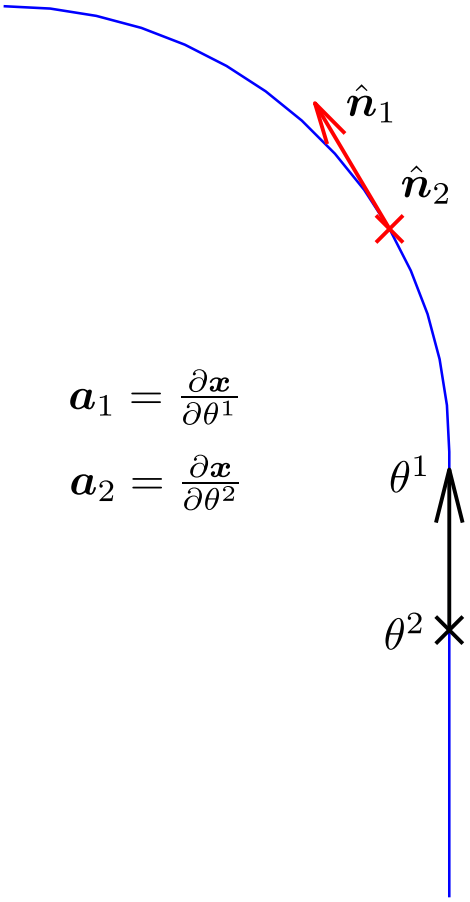

Figure A.1: Axisymmetric spherocylindrical geometry showing curvilinear coordinates θ^1 and θ^2, which are aligned with the z and θ directions within the cylindrical section. Tangent basis vectors $\boldsymbol{a}_\alpha$ are calculated by taking the partial derivative of position vector $\boldsymbol{x}$ with respect to the coordinates θ^α. Normalized basis vectors $\hat{\boldsymbol{n}}_1$ and $\hat{\boldsymbol{n}}_2$ are used to transform elastic moduli into the curvilinear frame.

values of 1 and 2. The covariant and contravariant metric tensors are

$$a_{\alpha\beta} = \boldsymbol{a}_\alpha \cdot \boldsymbol{a}_\beta \tag{A.2}$$

$$a^{\alpha\beta} = \boldsymbol{a}^\alpha \cdot \boldsymbol{a}^\beta, \tag{A.3}$$

where the definition $\boldsymbol{a}^\alpha \cdot \boldsymbol{a}_\beta = \delta^\alpha_\beta$ has been used. To account for the effects of curvature, the director and curvature tensor of the surface are required. Kirchhoff shell theory assumes that the cross-sectional rotations remain orthogonal to the mid-surface. Thus, the director $\boldsymbol{d}$ is defined as the unit normal to the surface,

$$\boldsymbol{d} \equiv \boldsymbol{a}_3 = \frac{\boldsymbol{a}_1 \times \boldsymbol{a}_2}{\|\boldsymbol{a}_1 \times \boldsymbol{a}_2\|} = \frac{\boldsymbol{a}_1 \times \boldsymbol{a}_2}{\sqrt{a}}, \tag{A.4}$$

where a is the determinant of the covariant metric, $a = \det(a_{\alpha\beta})$. The covariant components of the curvature tensor $\mathbf{B}$ are defined by

$$b_{\alpha\beta} \equiv -\boldsymbol{d}_{,\alpha} \cdot \boldsymbol{a}_\beta = \boldsymbol{d} \cdot \boldsymbol{a}_{\alpha,\beta}. \tag{A.5}$$

A.2 Membrane

Bending of the lipid bilayer is modeled using the classic energy equation attributed to Helfrich [13], which takes the form

$$\Pi^{\mathrm{m}}_{\mathrm{b}}[\boldsymbol{x}] = \int \frac{\mathcal{K}_b}{2}(2H - C_0)^2 + \mathcal{K}_G K \, dA. \tag{A.6}$$

In (A.6), $\mathcal{K}_b$ and $\mathcal{K}_G$ are the bending modulus and Gaussian modulus respectively, and C_0 represents the spontaneous curvature, induced by asymmetries in the bilayer. As a result of the Gauss-Bonnet theorem, the Gaussian curvature term is neglected. The mean curvature H is the average of the two principal curvatures, which is written as half the trace of $\mathbf{B}$

$$H = \frac{1}{2}\operatorname{tr}(\mathbf{B}) = \frac{1}{2} b^\alpha_\alpha. \tag{A.7}$$

The Gaussian curvature K is the determinant of the curvature tensor

$$K = \det(\mathbf{B}) = \det(b^\alpha_\beta). \tag{A.8}$$

The spontaneous curvature has a minimal effect on deformation, thus we set $C_0 = 0$ in the simulations. The bending has units of energy and is set to $\mathcal{K}_b = 20\, k_{\mathrm{B}}T$.

Taking the first variation of $\Pi_{\mathrm{b}}^{\mathrm{m}}$ leads to

$$\delta\Pi_{\mathrm{b}}^{\mathrm{m}} = \int \boldsymbol{n}^{\alpha} \cdot \delta\boldsymbol{a}_{\alpha} + \boldsymbol{m}^{\alpha} \cdot \delta\boldsymbol{d}_{,\alpha}\, dA, \tag{A.9}$$

with stress resultant

$$\boldsymbol{n}^{\alpha} = \mathcal{K}_b(2H - C_0)a^{\alpha\beta}\boldsymbol{d}_{,\beta} + \frac{\mathcal{K}_b}{2}(2H - C_0)^2\boldsymbol{a}^{\alpha} \tag{A.10}$$

and moment resultant

$$\boldsymbol{m}^{\alpha} = -\mathcal{K}_b(2H - C_0)\boldsymbol{a}^{\alpha}. \tag{A.11}$$

Stretching of the inner membrane gives rise to a tension that is proportional to the areal strain,

$$\tau_m = K_A\epsilon_A, \tag{A.12}$$

where K_A is the stretching modulus ($K_A = 60\, k_{\mathrm{B}}T/\mathrm{n}m^2$). Integrating the tension over the reference area gives rise to the elastic stretching energy

$$\Pi_{\mathrm{s}}^{\mathrm{m}} = \int \frac{K_A}{2}\epsilon_A^2\, dA = \frac{K_A}{2}\left(\frac{A - A_0}{A_0}\right)^2 A_0. \tag{A.13}$$

where A and A_0 are the deformed and reference areas, respectively. The stretching energy penalty is enforced at the global level.

A.3 Cell Wall

The peptidoglycan cell wall is implemented using a Saint Venant-Kirchhoff material model, which is an extension of the linear elastic Hooke's law to finite deformation. The strain energy density W is composed of both mid-surface stretching (W_{s}) and bending (W_{b}) terms,

$$W = \underbrace{\frac{1}{2}E_{\alpha\beta}A^{\alpha\beta\gamma\delta}E_{\gamma\delta}}_{W_{\mathrm{s}}} + \underbrace{\frac{1}{2}\rho_{\alpha\beta}D^{\alpha\beta\gamma\delta}\rho_{\gamma\delta}}_{W_{\mathrm{b}}}, \tag{A.14}$$

where $E_{\alpha\beta}$ is the Green-Lagrange strain

$$E_{\alpha\beta} = \frac{1}{2}(a_{\alpha\beta} - A_{\alpha\beta}), \tag{A.15}$$

$\rho_{\alpha\beta}$ is the curvature difference between deformed and undeformed configurations

$$\rho_{\alpha\beta} = b_{\alpha\beta} - B_{\alpha\beta}, \tag{A.16}$$

and $A^{\alpha\beta\gamma\delta}$ and $D^{\alpha\beta\gamma\delta}$ are fourth-order tensors containing the elastic and bending material constants, respectively.

In cylindrical polar coordinates $\{z, \theta\} \rightarrow \{1, 2\}$, the elastic and bending moduli components are

$$\bar{A}^{\alpha\beta\gamma\delta} = \frac{K_{\alpha\beta}h}{1 - \nu_{12}\nu_{21}} \left(\nu_{12} A^{\alpha\beta} A^{\gamma\delta} + \frac{1 - \nu_{12}}{2} \left(A^{\alpha\gamma} A^{\beta\gamma} + A^{\alpha\delta} A^{\beta\gamma} \right) \right), \tag{A.17}$$

$$\bar{D}^{\alpha\beta\gamma\delta} = \frac{h^2}{12} A^{\alpha\beta\gamma\delta}, \tag{A.18}$$

where the standard summation convention is ignored for the stiffness $K_{\alpha\beta}$. Due to vanishing shear terms, the only non-zero components of $K_{\alpha\beta}$ are,

$$K_{11} = \frac{E_1}{1 - \nu_{12}\nu_{21}}, \tag{A.19}$$

$$K_{22} = \frac{E_2}{1 - \nu_{12}\nu_{21}}. \tag{A.20}$$

The components $\bar{A}^{\alpha\beta\gamma\delta}$ and $\bar{D}^{\alpha\beta\gamma\delta}$ are transformed into the axi-symmetric curvilinear frame from the elastic properties in the z and θ directions $(E_z, E_\theta, \nu_{z\theta}, \nu_{\theta z})$. To carry out the basis transformation, we first define two unit vectors (see Fig. A.1) along the reference surface in the circumferential and tangential directions,

$$\boldsymbol{N}_1 = \frac{\boldsymbol{A}_1}{|\boldsymbol{A}_1|} = \frac{\boldsymbol{A}_1}{\sqrt{A_{11}}} \tag{A.21}$$

$$\boldsymbol{N}_2 = \frac{\boldsymbol{A}_2}{|\boldsymbol{A}_2|} = \frac{\boldsymbol{A}_2}{\sqrt{A_{22}}}. \tag{A.22}$$

The transformation tensor $\boldsymbol{T}$ is then defined as

$$T_\alpha^\beta = \boldsymbol{N}_\alpha \cdot \boldsymbol{A}^\beta. \tag{A.23}$$

In the $\{z, \theta\}$ frame, these components are written as $\bar{A}_{\alpha\beta\gamma\delta}$ and $\bar{D}_{\alpha\beta\gamma\delta}$, and by using T_α^β we write the material constants in the curvilinear frame using the relationship

$$A^{\alpha\beta\gamma\delta} = T_\eta^\alpha T_\kappa^\beta T_\mu^\gamma T_\nu^\delta \bar{A}_{\eta\kappa\mu\nu}, \tag{A.24}$$

$$D^{\alpha\beta\gamma\delta} = T_\eta^\alpha T_\kappa^\beta T_\mu^\gamma T_\nu^\delta \bar{D}_{\eta\kappa\mu\nu}. \tag{A.25}$$

Following the computation of $A^{\alpha\beta\gamma\delta}$ and $D^{\alpha\beta\gamma\delta}$ in the curvilinear frame, the stress and bending resultants are determined by

$$\boldsymbol{n}^{\alpha}_{\text{wall}} = \frac{\partial W}{\partial \boldsymbol{a}_{\alpha}} = n^{\alpha\beta}\boldsymbol{a}_{\beta} \tag{A.26}$$

and

$$\boldsymbol{m}^{\alpha}_{\text{wall}} = \frac{\partial W}{\partial \boldsymbol{d}_{,\alpha}} = m^{\alpha\beta}\boldsymbol{a}_{\beta}, \tag{A.27}$$

where $n^{\alpha\beta} = A^{\alpha\beta\gamma\delta}E_{\gamma\delta}$ and $m^{\alpha\beta} = D^{\alpha\beta\gamma\delta}\rho_{\gamma\delta}$.

APPENDIX B

Transport

B.1 Estimating Parameters

B.1.1 Water Permeability of the Membrane – μ_{m}

Water permeability of the inner membrane strongly influences the post-shock evolution of the cell, and is defined by the constant parameter μ_{m}. Cells initially respond to downshock by passively drawing water inward as a result of the imposed concentration gradient, and the rate at which water is accumulated is governed by μ_{m}. If μ_{m} is "large," then during these initial moments water will rapidly pass through the membrane and into the cytoplasm, increasing membrane tension and consequently gating a relatively large number of channels. Once these channels have opened, the cell can quickly expel osmolytes to reduce the pressure. On the other hand, when μ_{m} is "small" water accumulation takes place over a longer time scale, and tension slowly approaches gating thresholds. As a result, a smaller portion of channels are gated, thus decreasing solute efflux and lengthening the overall response time. Therefore, the membrane permeability μ_m directly controls the rate at which water enters the cell when channels are closed, and also dictates the time scale of the cell's response to downshock.

One parameter that is closely related to μ_m is the membrane permeation coefficient P_f, which is estimated to be in the range $P_f \approx 15-60\,\mu\mathrm{m/s}$ [32, 65]. We can obtain a relationship between P_f and μ_{m} by assuming purely diffusive transport and then using a modified version of Fick's law,

$$\frac{dV_m}{dt} = P_f A_m V_w \Delta C, \tag{B.1}$$

where V_m is the volume enclosed by the membrane surface area A_m, V_w is the molar volume of water, and ΔC is the concentration difference between the cell and its surroundings. Assuming an ideal solution, we can divide equation (B.1) by the osmotic pressure difference ($\Delta\Pi = k_{\mathrm{B}}T\Delta C$) and solve for μ_m,

$$\mu_m = \frac{P_f A_m V_w}{N_{\mathrm{A}} k_{\mathrm{B}} T}. \tag{B.2}$$

A spherocylindrical *E. coli* cell of radius $R = 500\,\mathrm{nm}$ and $L = 1\,\mu\mathrm{m}$ has surface area $A_m = 6.3\,\mu\mathrm{m}^2$. The molar volume of water is $V_w = 18\,\mathrm{ml/mol}$. Taking $P_f = 50\,\mu\mathrm{m/s}$ we can then evaluate μ_m

$$\mu_m = \frac{(50\,\mu\mathrm{m/s})(6.3\,\mu\mathrm{m}^2)(18\times10^{12}\,\mu\mathrm{m}^3/\mathrm{mol})}{(6.022\times10^{23}\,1/\mathrm{mol})(1.38\times10^{-23}\,\mathrm{J/K})(300\,\mathrm{K})} = 2.27\times10^{-24}\,\mathrm{m}^3/\mathrm{Pa/s}. \tag{B.3}$$

Due to the heterogeneity of cell sizes, the surface area available for diffusion, and uncertainty in P_f, we expect μ_m to be within the range

$$\mu_m \approx 10^{-25} - 10^{-23}\,\mathrm{m}^3/\mathrm{Pa/s}. \tag{B.4}$$

To validate our calculation we look towards hyper-osmotic shock experiments, which estimate that cells lose 30 % of their normal volume in approximately 1 s. This corresponds to a rate of roughly 10^{10} water molecules per second. To convert μ_m to similar units we divide by V_w and multiply by N_{A}

$$\mu_m \frac{N_{\mathrm{A}}}{V_w} \approx 3.3\times10^{9} - 3.3\times10^{10}\,\mathrm{molecules/atm/s}, \tag{B.5}$$

which yields the rate of water flow on a per atm basis. Noting that pressure variations during osmotic shock are believed to be around 1 atm, our calculation agrees with the literature values.

B.1.2 Channel Water Permeability – μ_c

The amount of water flow through a mechanosensitive ion channel is largely governed by its size, or pore radius. We can think of an MS channel as a cylindrical tube of radius r_c and length h_m (equal to the membrane thickness), oriented perpendicular to the membrane

surface. The Hagen-Poiseuille equation describing pipe flow for a given pressure difference can then be used to determine the permeability coefficient μ_c. This relationship states that a pressure drop ΔP drives a volumetric flow Q across the membrane, based on the equation

$$\Delta P = \frac{8 h_m \eta Q}{\pi r_c^4}, \tag{B.6}$$

where η is the viscosity of the solvent (water). Rewriting Eqn. (B.6) in terms of μ_c leads to

$$\mu_c = \frac{Q}{\Delta P} = \frac{\pi r_c^4}{8 h_m \eta}. \tag{B.7}$$

It is obvious that μ_c is strongly dependent on the pore radius r_c, from which we can conclude that smaller channel types such as MscS and MscM will have substantially lower water permeabilities. Evaluating the expression in Eqn. (B.7) for MscL using the parameters in Table 3.3, we get

$$\mu_c^{\mathrm{MscL}} = \frac{\pi (1.5\,\mathrm{nm})^4}{8(3\,\mathrm{nm})(10^{-3}\,\mathrm{N\cdot s/m^2})} = 6.6 \times 10^{-25}\,\mathrm{m^3/Pa/s}. \tag{B.8}$$

When we consider that a single cell has several hundred MscL channels, the total water permeability of MscL ($\mu_{\mathrm{c}}^{\mathrm{MscL}} \times \mathrm{N}_{\mathrm{c}}^{\mathrm{MscL}} \sim 10^{-22}\,\mathrm{m^3/Pa/s}$) will exceed the membrane permeability μ_m if all channels are in their opened state.

B.1.3 Channel Solute Permeability – $\alpha_{\mathbf{c}}$

To estimate the channel permeability to solute molecules, we make the assumption that transport is governed solely by diffusion. The channel can be idealized as a cylindrical pore of radius r and length h_m (equivalent to the membrane thickness), with its axis oriented in the z-direction. The axisymmetric geometry dictates that the concentration field C along the channel exclusively depends on z. By considering steady-state diffusion, we can then write the diffusion equation as

$$DC_{zz} = 0, \tag{B.9}$$

where D is the diffusion coefficient. Internal and external concentrations are defined as

$$C(0) = C_{in} \quad \text{and} \quad C(h) = C_{out}. \tag{B.10}$$

To solve for the concentration field $C(z)$, we integrate Eqn. (B.9) and apply the boundary conditions from Eqn. (B.10) to get

$$C(z) = \left(1 - \frac{z}{h}\right) C_{\text{in}} + \left(\frac{z}{h}\right) C_{out}. \tag{B.11}$$

Since the solution in Eqn. (B.11) is linear the concentration gradient is simply $\Delta C/h_m$, and we can write the flux through a single channel as

$$J_{ch} = A_c D \Delta C / h_m, \tag{B.12}$$

where $\Delta C = C_{out} - C_{\text{in}}$. Assuming an ideal solution ($\Delta\Pi = k_{\text{B}} T \Delta C$), the channel flux can be related to pressure through

$$J_{ch} = \alpha_c \Delta\Pi = \alpha_c k_{\text{B}} T \Delta C \quad \Rightarrow \quad \alpha_c = D \frac{A_c}{k_{\text{B}} T h_m}. \tag{B.13}$$

The parameter α_c describes the rate of solute flow through a channel per unit of pressure, and has units of 1/Pa/s. The diffusion constant D for various ions in water such as Na^+ and K^+ is $\sim 10^{-3}\,\mu\text{m}^2/\text{s}$. Taking values from Table 3.3, and $D = 10^{-3}\,\mu\text{m}^2/\text{s}$, we evaluate Eqn. (B.13) for MscL

$$\alpha_c^{\text{MscL}} = D \frac{A_c}{k_{\text{B}} T h_m} = (10^{-3}\,\mu\text{m}^2/\text{s}) \frac{\pi (1.5\,\text{nm})^2}{k_{\text{B}} T (3.0\,\text{nm})} \approx 600\,1/\text{Pa/s}. \tag{B.14}$$

As $\alpha_c \sim r^2$, the channel permeability to solute has a strong dependence on the pore radius, indicating that MscL is far more effective at transporting ions than its siblings. A smaller pore radius indicative of channels such as MscS and MscM, say $r = 1\,\text{nm}$, will give $\alpha_c \approx 300\,1/\text{Pa/s}$. This indicates that if diffusion is the only phenomenon in play here, different channel types (with unique properties) will have α_c values that differ by an order of magnitude, or more.

B.1.4 Channel Reflection Coefficient – σ

The amount of solute efflux permitted through a mechanosensitive channel is primarily limited by the pore size. The reflection coefficient describes how much solute is disallowed from traversing the channels due to the simultaneously flow of solvent. A simple mechanical model

for determining σ assumes that solute molecules are spherical, channels are cylindrical, and that there is no interaction amongst solutes with themselves [66]. The reflection coefficient can then be calculated using the equation

$$\sigma = \left[1 - (1 - \lambda)^2\right]^2, \tag{B.15}$$

where $\lambda \equiv r_{\text{solute}}/r_{\text{pore}}$ is the ratio of solute-to-pore radius.

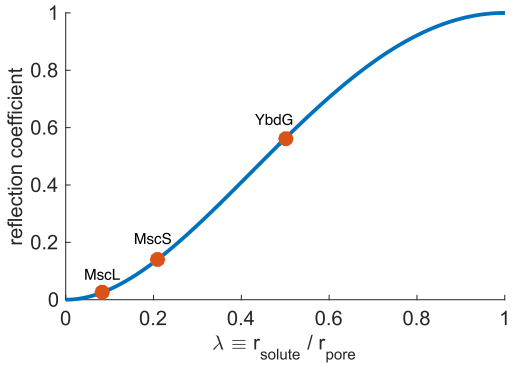

Figure B.1: Reflection coefficient σ for YbdG, MscS, and MscL calculated using Eqn. (B.15).

Potassium is by far the most abundant ion present in the *E. coli* cytosol, with intracellular concentrations ranging from 200 to 700 mM depending on external medium solute concentrations. With a hydrated radius of approximately 0.3 nm, the potassium ion is much smaller than the pores of MscL and MscS. However, K^+ is similar in size to YbdG channels, and some portion of these ions may be "reflected" by smaller channels based on their size alone. Interestingly, the potassium specific channel MscK preferentially transports K^+ over Na^+ even though the sodium anion is smaller in size. For this reason, the simple model utilized here may not be the best way to depict reflection through small or selective channels, though for non-selective large pores it appears to be adequate. In reality each solute-channel should have a unique reflection coefficient, but we have chosen to approximate all solute molecules as K^+.

Fig. B.1 shows the relationship in Eqn. (B.15) along with σ values for MscL, MscS, and YbdG indicated by red dots based on the hydrated radius of K^+. Smaller channels have greater reflection coefficients as they prevent the passage of solute molecules that exceed

the channel radius. More complicated models describing σ based on pore size show similar results. We expect $\sigma_{\mathrm{MscL}} \lesssim 0.1$, $\sigma_{\mathrm{MscS}} \lesssim 0.25$, and $0.25 \lesssim \sigma_{\mathrm{YbdG}} \leq 1.0$

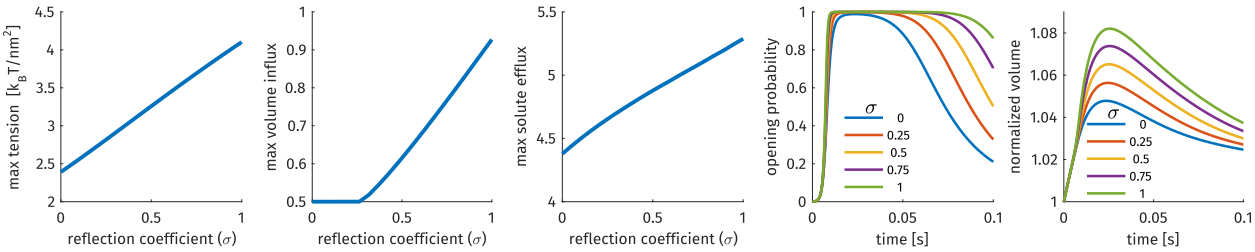

Figure B.2: Maximum values of membrane tension, volume influx, and solute efflux while varying σ. Channel opening probability and normalized volume are shown versus time for five specific values of σ. The model cell contains only a full complement of MscS channels and is subjected to a 0.5 M downshock.

B.1.5 Channel Osmosensitivity is Controlled by the Reflection Coefficient

Mechanosensitive channels are capable of transporting both water *and* solute molecules ($\sigma \neq 1$), and the amount of interaction between these fluxes is characterized by the reflection coefficient. The lower limit of $\sigma = 0$ represents maximum interaction of solute and solvent within channels. By setting $\sigma = 0$, the dimensionless kinetic equations are reduced to

$$\dot{v} = -\left(1 + \bar{\mu}\mathcal{P}_{open}\right)\Delta p + \Delta\pi, \tag{B.16}$$

$$\dot{n} = -\mathcal{P}_{open}\left(\bar{\alpha}\Delta\pi + \bar{c}\bar{\mu}\Delta p\right), \tag{B.17}$$

and

$$\dot{v}^{ch} = -\bar{\mu}\mathcal{P}_{open}\Delta p. \tag{B.18}$$

We note that in this situation of maximum interaction channel volume flux is insensitive to the osmotic chemical potential, is driven entirely by the hydrostatic pressure difference Δp, and remains outward (negative) throughout a hypo-osmotic shock.

For all nonzero values of σ, volume flow is influenced by the difference in osmotic pressure $\Delta\pi$, with increasing sensitivity as σ increases. Since $\Delta\pi$ is much larger than Δp during

the initial stages of downshock, transport of solvent and solute occurs is opposing directions. Water is drawn into the cell through channels (and the membrane) while solute is simultaneously jettisoned out of the cell. If σ is "large enough" ($\gtrsim 0.25$), $\dot{v}^{\text{ch}}$ is positive (inward) causing rapid increases in hydrostatic pressure and membrane tension. This effect is strongest with MscL due to its large pore size and greater water permeability μ^{ch}.

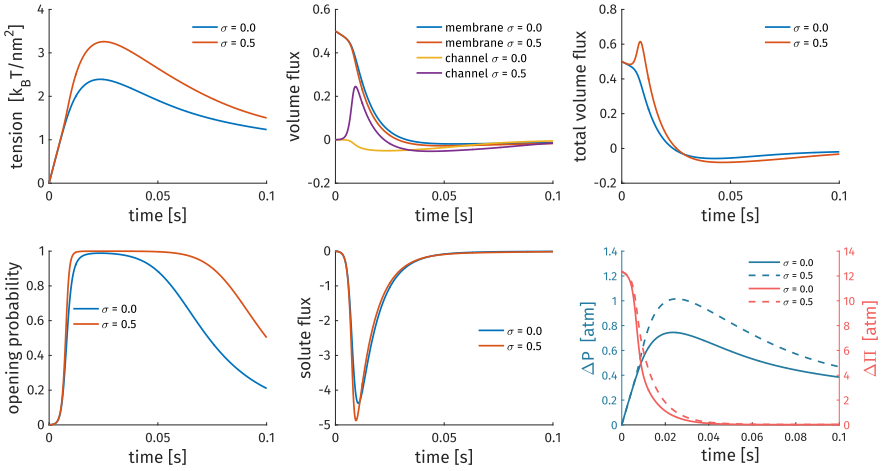

Figure B.3: Effect of the reflection coefficient on transport. When $\sigma = 0$, channel volume flux is solely dependent on the hydrostatic pressure difference ΔP. When $\sigma \neq 0$, channel volume flux depends on both ΔP and $\Delta\Pi$. In the latter case, channel volume flux is inward and solute efflux is outward shortly after shock initiation.

Interestingly, solute flux ($\dot{n}$) can actually increase with σ even though more solute molecules are "reflected" or turned away from passage through channels. The amount of solute flux at a given moment in time is determined by many factors including the pressure differences, opening probabilities, and permeability coefficients. Increasing the reflection coefficient keeps more solute inside the cell, but this in turn draws additional water into the cell increasing membrane tension. In situations where some channels have not gated ($\mathcal{P}_{\text{open}} < 1$), solute flux can increase. If all channels are already in their opened state, solute flux will decrease. However, solute flux is dominated by the first term in the equation ($\bar{\alpha}\mathcal{P}_{\text{open}}\Delta\Pi$), which is independent of σ. In other words, the amount of solute molecules "reflected" is overwhelmed by the term containing $\bar{\alpha}$. Ultimately, while the value of the reflection coefficient has a dramatic effect on volume flux, it has little bearing on solute flux $\dot{n}$.

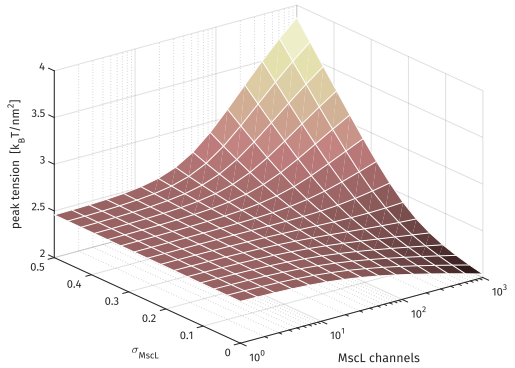

Figure B.4: Peak membrane tension plotted against varying MscL population and reflection coefficient (these quantities are held constant for MscS and YbdG) in a wild type cell. Shock magnitude is 0.5 M. Peak tension increases with the number of channels when $\sigma \gtrsim 0.25$.

B.2 Active Transport

E. coli cells maintain a near constant turgor pressure when the solute concentration of their surrounding environment does not undergo large fluctuations. Under these steady-state conditions, net flows of volume and solute are negligible. However, when this balance is disturbed and the internal pressure decreases (as in the case of hyper-osmotic shock), cells must accumulate solute molecules that, in turn, draw water into the cytoplasm and restore turgor. Therefore, cells must be equipped with some mechanism, such as a set of transmembrane ion transporters or pumps, that drives solutes against the concentration gradient into the cell. These "active" transporters require an energy source such as ATP to move solutes in the "uphill" direction, and are typically selective in terms of the ions that traverse them. While specific details of the mechanisms involved in active transport in *E. coli* remain unclear, we can nonetheless create a simple model to describe and understand their effects.

To incorporate active transport into the model we can add a constant flux term $\dot{n}_{act}$ to the equation for solute flux, which vanishes when the cell volume exceeds the reference volume, V_{ref}. The modified kinetic equation for solute is then

$$\dot{n} = -\left(\frac{n}{v} - c_{ext}\right)\sum_{i}^{\mathrm{N^c}} \bar{\alpha}_i + \frac{1}{2}\left(\frac{n}{v} + c_{ext}\right)\sum_{i}^{\mathrm{N^c}} (1-\sigma_i)\,\dot{v}^{ch} + \langle \dot{n}_{\mathrm{act}} \rangle\,, \tag{B.19}$$

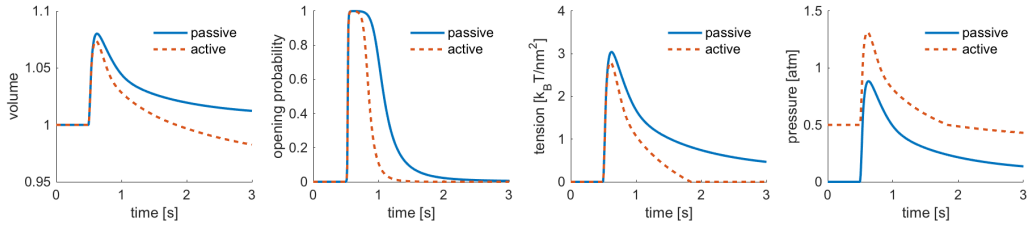

Figure B.5: Comparison of active and passive transport models.

where the angle brackets $\langle \cdot \rangle$ indicate that the enclosed term makes no contribution when $V > V_{\text{ref}}$. Here, we assume that the reference volume corresponds to a tension free state in the membrane, and that at volumes less than V_{ref} the cell wall alone absorbs the stress induced by the steady-state turgor pressure. As the opening probabilities of each channel type are very small but positive at zero tension, a small number of channels will always remain open, slowly leaking solutes and water. We set the active rate of solute accumulation to match this leak, such that $\dot{n} = \dot{v} = 0$. Therefore, under steady-state conditions the cell will actively accumulate solutes.

To understand the effects of turgor pressure and active transport on an osmotically shocked cell, we compare the response of the model with and without active transport (Fig. B.5). The model cells use the parameters in Table 3.1, and undergo a 0.8 M instantaneous downshock. Notably, in the response of the active model we observe a reduction in peak volume and membrane tension, and a faster recovery back to the reference volume. Additionally, MS channels remain open for a shorter period of time as a consequence of reduced membrane tension. This behavior can be attributed to the initial turgor, which reduces the rise in pressure required to attain osmotic equilibrium, and reverse the direction of volume change from swelling to shrinking. We also observe an overshoot in volume as the active model recovers, with the volume decreasing beneath the reference volume. This is not seen in the passive model, where the volume asymptotically approaches the initial reference volume from above. The overshoot feature is a product of the initial turgor pressure. When volume dips beneath the reference volume, the pump is switched on, and the cell slowly recovers back to its reference volume on the order of minutes.

The overshoot feature is the most interesting qualitative result here, as the minor differences seen in tension/opening probability are influenced more significantly by other aspects, such as the transport parameters. Nonetheless, the modified model provides a more complete picture of how bacterial cells adapt to osmotic shock.

APPENDIX C

Parametric Study of Growth

Thickness

Estimates for the cell wall thickness range from 3 to 6 nm. Nonlinearities in the stress-defect density relationship are stronger for thinner walls (Fig. C.1).

Defect shape

The shape of each strip of grown material is governed by the parameters c_θ and c_z in equation (5.8). We can define these constants in terms of the standard deviations s_θ and s_z (i.e., $c_\theta \equiv 1/2s_\theta^2$ and $c_z \equiv 1/2s_z^2$), which control width of the defect in the θ and z directions. The width s_z can be calculated from interstrand spacing estimates (1 to 4 nm). To appropriately model a continuum approximation of a point-like defect such as a dislocation, we assume that the value of s_θ is small such that the Gaussian blob falls off rapidly in the θ direction. Smaller values of s_θ lead to higher axial stress, while the hoop stress does not exhibit any significant change (Fig. C.2).

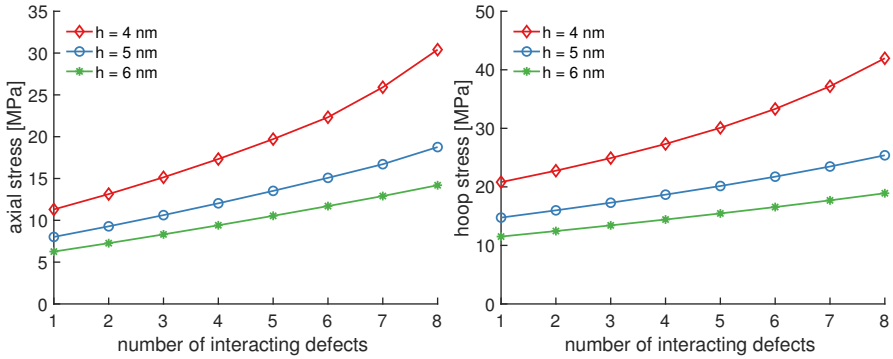

Figure C.1: Effects of defect interactions and cell wall thickness on the axial (left) and circumferential (right) Cauchy stress (σ_{zz} and $\sigma_{\theta\theta}$). As the cell wall thickness decreases, the stress-defect density relationship becomes increasingly nonlinear.

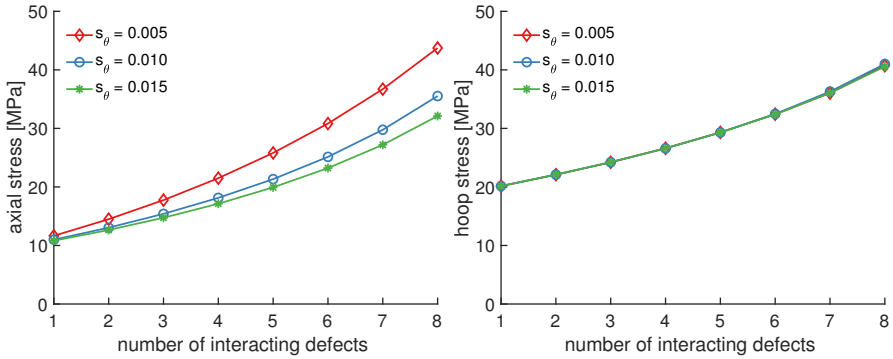

Figure C.2: Influence of defect shape on the cell wall stress. The parameter s_θ controls how abruptly the endpoint of a strip of new material falls off in the hoop direction, and the effects of varying s_θ on the axial (left) and circumferential (right) stresses are shown above. A smaller standard deviation (more rapid fall off) in the θ direction of the two-dimensional Gaussian causes larger tensile stresses in the region surrounding the strip ends. The value of s_θ has a negligible effect on the circumferential stress, which is controlled by s_z.

REFERENCES

[1] Yi Deng, Mingzhai Sun, and Joshua W. Shaevitz. Direct measurement of cell wall stress stiffening and turgor pressure in live bacterial cells. *Physical Review Letters*, 107(15):7–10, 2011.

[2] X. Yao, M. Jericho, D. Pink, and T. Beveridge. Thickness and elasticity of gram-negative murein sacculi measured by atomic force microscopy. *Journal of Bacteriology*, 181(22):6865–6875, 1999.

[3] Gene Wei Li, David Burkhardt, Carol Gross, and Jonathan S. Weissman. Quantifying absolute protein synthesis rates reveals principles underlying allocation of cellular resources. *Cell*, 157(3):624–635, 2014.

[4] Eduardo Perozo, D. Marien Cortes, Pornthep Sompornpisut, Anna Kloda, and Boris Martinac. Open channel structure of MscL and the gating mechanism of mechanosensitive channels. *Nature*, 418(6901):942–948, 2002.

[5] Ben Corry and Boris Martinac. Bacterial mechanosensitive channels: Experiment and theory. *Biochimica et Biophysica Acta - Biomembranes*, 1778(9):1859–1870, 2008.

[6] Ian R Booth, Tim Rasmussen, Michelle D Edwards, Susan Black, Akiko Rasmussen, Wendy Bartlett, and Samantha Miller. Sensing bilayer tension: bacterial mechanosensitive channels and their gating mechanisms. *Biochemical Society transactions*, 39(3):733–740, 2011.

[7] Andriy Anishkin and Sergei Sukharev. Water dynamics and dewetting transitions in the small mechanosensitive channel MscS. *Biophysical journal*, 86(5):2883–95, 2004.

[8] Enrique R. Rojas, Gabriel Billings, Pascal D. Odermatt, George K. Auer, Lillian Zhu, Amanda Miguel, Fred Chang, Douglas B. Weibel, Julie A. Theriot, and Kerwyn Casey Huang. The outer membrane is an essential load-bearing element in Gram-negative bacteria. *Nature*, 559(7715):617–621, 2018.

[9] Maja Bialecka-Fornal, Heun Jin Lee, and Rob Phillips. Rate of osmotic downshock determines bacterial survival probability. *Journal of bacteriology*, 197(October):231–237, 2014.

[10] Peter Eaton, João C. Fernandes, Eulália Pereira, Manuela E. Pintado, and F. Xavier Malcata. Atomic force microscopy study of the antibacterial effects of chitosans on Escherichia coli and Staphylococcus aureus. *Ultramicroscopy*, 108(10):1128–1134, 2008.

[11] Hannah H. Tuson, George K. Auer, Lars D. Renner, Mariko Hasebe, Carolina Tropini, Max Salick, Wendy C. Crone, Ajay Gopinathan, Kerwyn Casey Huang, and Douglas B. Weibel. Measuring the stiffness of bacterial cells from growth rates in hydrogels of tunable elasticity. *Molecular Microbiology*, 84(5):874–891, 2012.

[12] James C. Gumbart, Morgan Beeby, Grant J. Jensen, and Benoît Roux. Escherichia coli Peptidoglycan Structure and Mechanics as Predicted by Atomic-Scale Simulations. *PLoS Computational Biology*, 10(2), 2014.

[13] W Helfrich. Elastic properties of lipid bilayers: theory and possible experiments. *Zeitschrift fur Naturforschung. Teil C: Biochemie, Biophysik, Biologie, Virologie*, 28(11):693–703, 1973.

[14] P. B. Canham. The minimum energy of bending as a possible explanation of the biconcave shape of the human red blood cell. *Journal of Theoretical Biology*, 26(1):61–81, 1970.

[15] E.A. Evans. Bending Resistance and Chemically Induced Moments in Membrane Bilayers. *Biophysical Journal*, 14(12):923–931, dec 1974.

[16] Laura Picas, Felix Rico, and Simon Scheuring. Direct measurement of the mechanical properties of lipid phases in supported bilayers. *Biophysical Journal*, 102(1):L01–L03, jan 2012.

[17] Yen Sun, Tzu-Lin Sun, and Huey W. Huang. Physical Properties of Escherichia coli Spheroplast Membranes. *Biophysical Journal*, 107(9):2082–2090, nov 2014.

[18] W. Rawicz, K.C. Olbrich, T. McIntosh, D. Needham, and E. Evans. Effect of Chain Length and Unsaturation on Elasticity of Lipid Bilayers. *Biophysical Journal*, 79(1):328–339, 2000.

[19] David J. Steigmann. Koiter's shell theory from the perspective of three-dimensional nonlinear elasticity. *Journal of Elasticity*, 111(1):91–107, 2013.

[20] Teuta Pilizota and Joshua W. Shaevitz. Plasmolysis and cell shape depend on solute outer-membrane permeability during hyperosmotic shock in E. coli. *Biophysical Journal*, 104(12):2733–2742, 2013.

[21] Renata Buda, Yunxiao Liu, Jin Yang, Smitha Hegde, Keiran Stevenson, Fan Bai, and Teuta Pilizota. Dynamics of Escherichia coli 's passive response to a sudden decrease in external osmolarity. *Proceedings of the National Academy of Sciences*, 113(40):E5838–E5846, oct 2016.

[22] Michelle D. Edwards, Susan Black, Tim Rasmussen, Akiko Rasmussen, Neil R. Stokes, Terri Leigh Stephen, Samantha Miller, and Ian R. Booth. Characterization of three novel mechanosensitive channel activities in Escherichia coli. *Channels (Austin, Tex.)*, 6(4):272–281, 2012.

[23] Maja Bialecka-Fornal, Heun Jin Lee, Hannah a. DeBerg, Chris S. Gandhi, and Rob Phillips. Single-cell census of mechanosensitive channels in living bacteria. *PLoS ONE*, 7(3), 2012.

[24] I. R. Booth and Paul Blount. The MscS and MscL Families of Mechanosensitive Channels Act as Microbial Emergency Release Valves. *Journal of Bacteriology*, 194(18):4802–4809, sep 2012.

[25] Neil R Stokes, Heath D Murray, Chandrasekaran Subramaniam, Richard L Gourse, Petra Louis, Wendy Bartlett, Samantha Miller, and Ian R Booth. A role for mechanosensitive channels in survival of stationary phase: regulation of channel expression by RpoS. *Proceedings of the National Academy of Sciences of the United States of America*, 100(26):15959–15964, 2003.

[26] Enrique Rojas, Julie a Theriot, and Kerwyn Casey Huang. Response of Escherichia coli growth rate to osmotic shock. *Proceedings of the National Academy of Sciences of the United States of America*, 111(21):7807–12, 2014.

[27] Marcel Reuter, Nicholas J Hayward, Susan S Black, Samantha Miller, David T F Dryden, and Ian R Booth. Mechanosensitive channels and bacterial cell wall integrity: does life end with a bang or a whimper? *Journal of the Royal Society, Interface / the Royal Society*, 11(91):20130850, 2014.

[28] Jonas van den Berg, Heloisa Galbiati, Akiko Rasmussen, Samantha Miller, and Bert Poolman. On the mobility, membrane location and functionality of mechanosensitive channels in Escherichia coli. *Scientific Reports*, 6(April):32709, 2016.

[29] O Kedem and a Katchalsky. Thermodynamic analysis of the permeability of biological membranes to non-electrolytes. 1958. *Biochimica et biophysica acta*, 1000:413–430, 1989.

[30] Gerald S. Manning. Binary diffusion and bulk flow through a potential-energy profile: A kinetic basis for the thermodynamic equations of flow through membranes. *The Journal of Chemical Physics*, 49(6):2668–2675, 1968.

[31] Gerald S. Manning. Correlation of solute permeability and reflection coefficient for rigid membranes with high solvent content. *The Journal of Physical Chemistry*, 76(3):393–399, feb 1972.

[32] K Olbrich, W Rawicz, D Needham, and E Evans. Water permeability and mechanical strength of polyunsaturated lipid bilayers. *Biophysical journal*, 79(1):321–327, 2000.

[33] Michael Marko, Chyongere Hsieh, Richard Schalek, Joachim Frank, and Carmen Mannella. Focused-ion-beam thinning of frozen-hydrated biological specimens for cryo-electron microscopy. *Nature Methods*, 4(3):215–217, 2007.

[34] Miriam Boer, Andriy Anishkin, and Sergei Sukharev. Adaptive MscS Gating in the Osmotic Permeability Response in E. coli : The Question of Time. *Biochemistry*, 50(19):4087–4096, may 2011.

[35] Ulrike Schumann, Michelle D Edwards, Tim Rasmussen, Wendy Bartlett, Pieter van West, and Ian R Booth. YbdG in Escherichia coli is a threshold-setting mechanosensitive channel with MscM activity. *Proceedings of the National Academy of Sciences of the United States of America*, 107(28):12664–12669, 2010.

[36] N Levina, S Tötemeyer, N R Stokes, P Louis, M a Jones, and I R Booth. Protection of Escherichia coli cells against extreme turgor by activation of MscS and MscL mechanosensitive channels: identification of genes required for MscS activity. *The EMBO journal*, 18(7):1730–1737, 1999.

[37] E Evans. Dynamic Tension Spectroscopy and Strength of Biomembranes. *Biophysical Journal*, 85(4):2342–2350, 2003.

[38] Kristopher E. Daly, Kerwyn Casey Huang, Ned S. Wingreen, and Ranjan Mukhopadhyay. Mechanics of membrane bulging during cell-wall disruption in Gram-negative bacteria. *Physical Review E - Statistical, Nonlinear, and Soft Matter Physics*, 83(4):1–4, 2011.

[39] Larry A. Taber. Biomechanics of Growth, Remodeling, and Morphogenesis. *Applied Mechanics Reviews*, 48(8):487, 1995.

[40] V A Lubarda and A Hoger. On the mechanics of solids with a growing mass. *International Journal of Solids and Structures*, 39(18):4627–4664, 2002.

[41] Andreas Menzel and Ellen Kuhl. Frontiers in growth and remodeling. *Mechanics Research Communications*, 42:1–14, 2012.

[42] Ellen Kuhl. Growing matter: A review of growth in living systems. *Journal of the Mechanical Behavior of Biomedical Materials*, 29:529–543, 2014.

[43] E H Lee. Elastic-Plastic Deformation at Finite Strains. *Journal of Applied Mechanics*, 36(1):1, 1969.

[44] E K Rodriguez, a Hoger, and a D McCulloch. Stress-dependent finite-growth in soft elastic tissues. *Journal of biomechanics*, 27(4):455–467, 1994.

[45] Ellen Kuhl and Paul Steinmann. Mass- and volume-specific views on thermodynamics for open systems. *Proceedings of the Royal Society A: Mathematical, Physical and Engineering Sciences*, 459(2038):2547–2568, 2003.

[46] G Himpel, E Kuhl, A Menzel, and P Steinmann. Computational modelling of isotropic multiplicative growth. *CMES - Computer Modeling in Engineering and Sciences*, 8(2):119–134, 2005.

[47] Ping Wang, Lydia Robert, James Pelletier, Wei Lien Dang, Francois Taddei, Andrew Wright, and Suckjoon Jun. Robust growth of escherichia coli. *Current Biology*, 20(12):1099–1103, 2010.

[48] a. Amir and D. R. Nelson. Dislocation-mediated growth of bacterial cell walls. *Proceedings of the National Academy of Sciences*, 109(25):9833–9838, 2012.

[49] Ariel Amir, Jayson Paulose, and David R Nelson. Theory of interacting dislocations on cylinders. *Physical Review E*, 87(4):042314, apr 2013.

[50] David R. Nelson. Biophysical Dynamics in Disorderly Environments. *Annual Review of Biophysics*, 41(1):371–402, 2012.

[51] Ariel Amir and Sven van Teeffelen. Getting into shape: How do rod-like bacteria control their geometry? *Systems and Synthetic Biology*, 8(3):227–235, sep 2014.

[52] Tristan S Ursell, Jeffrey Nguyen, Russell D Monds, Alexandre Colavin, Gabriel Billings, Nikolay Ouzounov, Zemer Gitai, Joshua W Shaevitz, and Kerwyn Casey Huang. Rod-like bacterial shape is maintained by feedback between cell curvature and cytoskeletal localization. *Proceedings of the National Academy of Sciences of the United States of America*, 111(11):E1025–34, 2014.

[53] S. van Teeffelen, S. Wang, L. Furchtgott, K. C. Huang, N. S. Wingreen, J. W. Shaevitz, and Z. Gitai. The bacterial actin MreB rotates, and rotation depends on cell-wall assembly. *Proceedings of the National Academy of Sciences*, 108(38):15822–15827, 2011.

[54] Jaan Männik, Rosalie Driessen, Peter Galajda, Juan E Keymer, and Cees Dekker. Bacterial growth and motility in sub-micron constrictions. *Proceedings of the National Academy of Sciences of the United States of America*, 106(35):14861–14866, 2009.

[55] Ariel Amir, Farinaz Babaeipour, D. B. McIntosh, David R Nelson, and Suckjoon Jun. Bending forces plastically deform growing bacterial cell walls. *Proceedings of the National Academy of Sciences*, 111(16):5778–5783, apr 2014.

[56] Yaron Caspi. Deformation of filamentous Escherichia coli cells in a microfluidic device: A new technique to study cell mechanics. *PLoS ONE*, 9(1), 2014.

[57] Benjamin P. Bratton, Joshua W. Shaevitz, Zemer Gitai, and Randy M. Morgenstein. MreB polymers and curvature localization are enhanced by RodZ and predict E. coli's cylindrical uniformity. *Nature Communications*, 9(1), 2018.

[58] Alexandre Colavin, Handuo Shi, and Kerwyn Casey Huang. RodZ modulates geometric localization of the bacterial actin MreB to regulate cell shape. *Nature Communications*, 9(1):1–11, 2018.

[59] Lars D. Renner, Prahathees Eswaramoorthy, Kumaran S. Ramamurthi, and Douglas B. Weibel. Studying biomolecule localization by engineering bacterial cell wall curvature. *PLoS ONE*, 8(12), 2013.

[60] Felix Wong, Lars D. Renner, Gizem Özbaykal, Jayson Paulose, Douglas B. Weibel, Sven van Teeffelen, and Ariel Amir. Mechanical strain sensing implicated in cell shape recovery in Escherichia coli. *Nature Microbiology*, 2(July):17115, 2017.

[61] Robert D. Turner, Stéphane Mesnage, Jamie K. Hobbs, and Simon J. Foster. Molecular imaging of glycan chains couples cell-wall polysaccharide architecture to bacterial cell morphology. *Nature Communications*, 9(1), 2018.

[62] Oleksii Sliusarenko, Matthew T Cabeen, Charles W Wolgemuth, Christine Jacobs-Wagner, and Thierry Emonet. Processivity of peptidoglycan synthesis provides a built-in mechanism for the robustness of straight-rod cell morphology. *Proceedings of the National Academy of Sciences of the United States of America*, 107(22):10086–10091, 2010.

[63] Philipp V. Olshausen, Hervé Joël Defeu Soufo, Kai Wicker, Rainer Heintzmann, Peter L. Graumann, and Alexander Rohrbach. Superresolution imaging of dynamic MreB filaments in B. subtilis - A multiple-motor-driven transport? *Biophysical Journal*, 105(5):1171–1181, 2013.

[64] Feng Feng and William S. Klug. Finite element modeling of lipid bilayer membranes. *Journal of Computational Physics*, 220(1):394–408, 2006.

[65] J. C. Mathai, S. Tristram-Nagle, J. F. Nagle, and M. L. Zeidel. Structural Determinants of Water Permeability through the Lipid Membrane. *The Journal of General Physiology*, 131(1):69–76, 2007.

[66] John L Anderson and Dermot M. Malone. Mechanism of Osmotic Flow in Porous Membranes. *Biophysical Journal*, 14(12):957–982, dec 1974.